

**Critical Exponents in a Helimagnet,
Griffiths Phase Dynamics in a Dilute Ising System
and
A Search for Magnetic Order in Titanium.**

David James Larkman

Department of Physics and Astronomy



THE UNIVERSITY
of MANCHESTER

A thesis submitted to the University of Manchester for the degree of Doctor of

Philosophy in the Faculty of Science

1997.

ProQuest Number: 10833686

All rights reserved

INFORMATION TO ALL USERS

The quality of this reproduction is dependent upon the quality of the copy submitted.

In the unlikely event that the author did not send a complete manuscript and there are missing pages, these will be noted. Also, if material had to be removed, a note will indicate the deletion.



ProQuest 10833686

Published by ProQuest LLC (2018). Copyright of the Dissertation is held by the Author.

All rights reserved.

This work is protected against unauthorized copying under Title 17, United States Code
Microform Edition © ProQuest LLC.

ProQuest LLC.
789 East Eisenhower Parkway
P.O. Box 1346
Ann Arbor, MI 48106 – 1346

h0991284

7h 20175
(DQDG2) ✓



Contents.

<i>Abstract</i>	5
<i>Declaration</i>	6
<i>Copyright and Intellectual property rights</i>	7
<i>Acknowledgements</i>	8
1. Introduction	10
1.1 Preamble and Outline of Thesis	10
1.2 An Introduction to Phase Transitions and Spin Dynamics	12
1.3 The Theory and Practice of Neutron Magnetic Scattering	18
1.3.1 Reactor Sources (Risø and the ILL).....	23
1.3.2 The Spallation Source (ISIS).....	24
1.4 References	26
2. Critical Exponents for the Paramagnetic to Helimagnetic Transition in Holmium	27
2.1 Introduction	27
2.2 The Magnetic Structure of Holmium	28
2.3 Previous Experiments and Theoretical Predictions	30
2.4 Experiment	33
2.4.1 The Triple-Axis Spectrometer IN8	34
2.4.2 Collection of Data	36
2.5 Data Fitting and Results.....	39
2.5.1 The Triple Axis Simulation and Fitting Program	39
2.5.2 The Model	44
2.5.3 Results	46
2.6 Discussion and Conclusions	51

2.7 References	54
3. Spin Dynamics in the Dilute Ising Magnet $Mn_{1-x}Zn_xF_2$	56
3.1 Introduction	56
3.2 Theory, Background and Motivation	59
3.3 Instrumentation and Method	64
3.3.1 The Triple Axis Spectrometer IN12.	65
3.3.2 Collection of Data	66
3.4 Data Analysis and Results.	69
3.4.1 The Fast Fourier Transform and Fitting Program	69
3.4.2 Resolution and Bose Factor Corrections.	71
3.4.3 The Model for $C(t)$ and $S(q, \omega)$	73
3.4.4 Results	75
3.5 Interpretation of Results	85
3.6 Conclusions and Further Work	89
3.7 References	91
4. A Search For Magnetic Order in α-Titanium	93
4.1 Introduction	93
4.2 The Experiments	97
4.2.1 Vibrating Sample Magnetometer Measurements of the Bulk Susceptibility of α -Titanium	97
4.2.1.1 Instrumentation and Method	97
4.2.1.2 Results and Discussion.	99
4.2.2 A Neutron Diffraction Experiment on α -Titanium Performed on POLARIS at ISIS.	103
4.2.3 Diffraction Measurements on a Single Crystal of α -Titanium Performed on SXD at ISIS	105

4.2.3.1 Instrumentation and Method.....	105
4.2.3.2 Results and Discussion.	106
4.2.4 Diffraction Measurements on α -Titanium Performed on TAS3 at Risø.....	109
4.2.4.1 Instrumentation and Method.....	109
4.2.4.2 Results and Discussion.	113
4.2.5 A Muon Spin-Relaxation Experiment on α -Titanium at ISIS.	117
4.2.5.1 Theory.....	118
4.2.5.2 Instrumentation and Method.....	120
4.2.5.3 Results and Discussion.	121
4.2.6 A Diffraction Measurement on Polycrystalline α -Titanium Performed on D1B at the ILL.	124
4.2.6.1 Instrumentation and Method.....	124
4.2.6.2 Results and Discussion.	125
4.3 Discussion and Conclusions.	127
4.4 References.	129

Abstract.

The critical exponents, γ , ν and η which describe the paramagnetic to helimagnetic phase transition in holmium, a c-axis helimagnet, have been measured using neutron scattering. A novel approach to the much-discussed central peak problem is described. The exponents were found to be $\gamma=1.11(6)$, $\nu=0.56(5)$ and $\eta=0.014(8)$ in agreement with previous experimental work.

The first direct quantitative observation of the non-exponential relaxation process which is considered to be the signature of the Griffiths phase in dilute magnetic systems has been achieved, supporting previous theoretical work. Neutron inelastic scattering was used to measure the power spectrum of the dilute Ising magnet $\text{Mn}_{1-x}\text{Zn}_x\text{F}_2$, both in and out of the Griffiths phase. These data were then fitted to a correlation function defined in the time domain via a fast Fourier transform. The Griffiths dynamics dominate the form of the correlation function when the correlation function has decayed to $\sim 1\%$ of its original value.

Also presented is a chronological account of a series of experiments performed by the Manchester group over the last four years in an attempt to identify the magnetic ordering, or otherwise, in α -titanium. Included here are bulk magnetometry measurements, a muon spin relaxation experiment and bulk magnetisation measurements. Previous observations of a non-hcp neutron powder-diffraction peak are discredited while bulk magnetisation effects are consistently observed.

Declaration.

Dr P.W. Mitchell has, as my supervisor, been involved in all work contained in this thesis. The VSM measurements (section 4.2.1) were performed in collaboration with Dr J.R.Lowden (University of Manchester). The POLARIS experiment (section 4.2.2) was performed entirely by Dr J.R.Lowden. The SXD and TAS3 experiments (sections 4.2.3 and 4.2.4) were performed jointly by the author and Dr J.R. Lowden. The final D1B experiment (section 4.2.6) was undertaken in collaboration with Mr S. Subiger (University of Manchester). All other work was undertaken solely by the author and Dr P.W. Mitchell.

No portion of the work contained within this thesis has been submitted in support of an application for another degree or qualification at this or any other university or institute of learning.

Copyright and Intellectual property rights.

Copyright in the text of this thesis rests with the author. Copies (by any process) either in full, or of extracts, may be made only in accordance with instructions given by the author and lodged in the John Rylands University Library of Manchester. Details may be obtained from the librarian. This page must form part of any such copies made. Further copies (by any process) of copies made in accordance with such instructions may not be made without the permission (in writing) of the Author.

The ownership of any intellectual property rights which may be described in this thesis is vested in the University of Manchester, subject to any prior agreement to the contrary, and may not be made available for use by third parties without the written permission of the University, which will prescribe the terms and conditions of any such agreement.

Acknowledgements.

My thanks go firstly to Peter Mitchell, my supervisor, who has been a source of guidance and inspiration for all the work in this thesis. I would also like to thank all the members of the Manchester Condensed Matter and Non Linear Dynamics Group.

I would like to thank the staff who helped me at the ILL, ISIS and Risø neutron Facilities. Without them the experiments presented here would not have happened.

Particular personal thanks go to all the members of my family and the following friends: Grainne Wood, Bob Wood, Rich Haley, George Blake, Jonathan Cook, Sai-Kong Chin, Mathew Dodgson, Dennis Dyke, Jim Edwards, Paul Farnaby, Stan Gillott, Anne Kienappel, Jeff Lowden, Steve May, Jill Merrill, Sarah Philipson, Mark Sellers, Hiroko Short, Graeme Seiffert, Sebastien Subiger, Richard Stuckey, Patrick Smith and Rodney Walker; without any of who the last few years would not have been what it was and this thesis would have been more difficult to write.

I acknowledge the financial support of the EPSRC.

M.M.

Chapter 1. Introduction.

1.1 Preamble and Outline of Thesis.

Amongst all the electronic properties of solids magnetism is perhaps the most widely interesting. Even the smallest improvements in the bulk properties of magnets, such as saturation magnetisation, can be of real economic significance to the engineer. At a more academic level, phase transitions in magnetic systems have provided models for some of the most abstract modern theoretical debate. Theoretical and experimental work on magnetic phenomena has contributed enormously to a more general understanding of collective phenomena in physics. The now broadly applicable theoretical concepts of universality, scaling and symmetry have been developed and expanded with experimental observations of continuous phase transitions in magnets. The simplicity of magnetic systems makes them an appealing platform for investigating processes present in more complex collective phenomena. The elementary nature of the microscopic interactions and hence of the Hamiltonians which describe these systems, allow the effects of dimensionality, symmetry and many other properties to be studied almost in isolation from each other. This thesis contains two studies of phenomena associated with continuous phase transitions in magnetic systems and in the final chapter an attempt to find ordered magnetism in α -titanium, a system whose chemistry indicates a propensity for magnetism but which is thought to be non-magnetic.

The structure of this thesis is as follows. The next section is dedicated to establishing a basic background in the theory of phase transitions and associated spin dynamics. The

remainder of this chapter discusses the theory and practice of neutron scattering covering the results of a mathematical description of magnetic scattering and a brief description of how an experiment is performed along with the details of the facilities (the ILL, ISIS and Risø) where the experiments in this thesis were performed. More specific detail of the instruments used for each experiment can be found in the relevant chapters. These sections introduce some of the concepts and notation used later in this work.

Chapter 2, chapter 3 and chapter 4 are self-contained accounts of the three experimental projects which make up this thesis. Chapter 2 is concerned with the measurement of the critical exponents which describe the paramagnetic to helimagnetic phase transition in holmium, a c-axis helimagnet. A novel approach to the fitting of the much discussed central peak problem is described. Chapter 3 contains the first direct quantitative observation of the non-exponential relaxation process considered the signature of the Griffiths phase in dilute magnetic systems. Both of these chapters include a full discussion of the data analysis techniques used. Chapter 4 is a chronological account of a series of experiments performed by the Manchester group over the last four years in an attempt to identify the magnetic ordering, or otherwise, in α -titanium.

1.2 An Introduction to Phase Transitions and Spin Dynamics.

Phase transitions are matters of everyday experience: The boiling of water in a kettle; the formation of ice in a freezer. Phase transitions are central to life on earth and understanding them is one of the prime tasks of condensed matter physicists. It is the balance between the internal energy and the entropy of the two phases that drives a system to undergo a phase transition at a certain critical temperature, T_c . Phase transitions can be 'first order' or 'continuous'. For example, under normal circumstances the phase transitions of H_2O are 'first order'. First order phase transitions are those that involve latent heat. When a material makes a first-order phase transition from a high temperature phase to a low temperature phase, a non-zero quantity of heat, the latent heat, is given out as the material is cooled through an infinitesimally small temperature range around the transition temperature. Transitions are usually accompanied by "spontaneous symmetry breaking", the lowering of the symmetry of the high temperature phase to the low symmetry of the low temperature, more ordered, phase.

The paradigm of a continuous phase transition is the conversion at the Curie temperature ($T_c=1043K$) of iron from paramagnetic to ferromagnetic form. At $T>T_c$ iron is paramagnetic i.e. the material is not magnetised in the absence of an applied magnetic field. If a weak field is applied the magnetic moment per unit volume, m , is proportional to the applied magnetic field. In the ferromagnetic state ($T<T_c$), the material forms ordered domains which are magnetised even when no field is applied, and when an external field is applied, B , the magnetisation within the domains swings to align with B . Consequently, m is no longer linearly related to B . The magnitude of the magnetisation within a given domain, $m_0(T)$ at $B=0$ vanishes as one approaches T_c from below. As a sample of iron is heated through T_c in zero applied field, its magnetisation steadily decreases as T_c is approached, vanishing entirely at T_c and for all higher temperatures. What changes discontinuously at T_c is the *rate of change* of m_0 rather than m_0 itself. This

is the essence of a continuous phase transition. Free energy is continuous through the transition, but if the first derivatives, e.g. entropy, volume, magnetisation etc., are discontinuous, then the transition is first order. For example, when water freezes there is an abrupt change in the properties of the system, e.g. density and specific heat. If the first derivatives are continuous then the transition is continuous.

In the last two decades much work has been done in the area of continuous phase transitions. Theoreticians, using the renormalisation group¹, have made great progress in understanding the behavior of materials very close to their transition temperatures. Transitions are grouped into 'universality classes'. Each class contains transitions which are similar. Within each universality class transitions are described by a single set of 'critical exponents' which describe the temperature dependent behavior of the properties of the system near to the transition, in the so-called critical region.

The simplest theory of phase transitions is the mean (or molecular) field theory which neglects local fluctuations by replacing the value of the magnetisation at specific site with its average value. Fluctuations neglected by this approximation play an important role and can strongly modify the behavior of a system. The theory of phase transitions is described in many texts. A good introduction to phase transitions prior to the influence of the renormalisation group is given by Stanley², and for a modern version see Binney³. For an overview of the experimental side of critical phenomena see Collins⁴ and Cowley⁵. The theory is concerned with behavior very close to the critical temperature. As the temperature of the sample is increased from below the critical temperature magnetic disorder increases. Very close to the critical temperature there are localised regions which are more or less ordered and which dynamically go through large fluctuations in time and position. These fluctuations have a characteristic length scale and relaxation time both of which diverge at T_c . Neutrons can be used to detect these fluctuations provided they have a long enough relaxation time.

For a system undergoing a continuous transition many experimentally observable properties near to T_c are scaled by a power law dependence on the reduced temperature, t defined as:

$$t \equiv \frac{|T - T_c|}{T_c}$$

Equation 1-1

Scaling theory defines a set of critical exponents which describe the behavior of the system and which are measurable experimentally in a variety of ways including neutron scattering.

The order parameter is the magnitude of the parameter which is zero in the high symmetry phase ($T > T_c$) and non-zero in the low symmetry phase ($T < T_c$). The behavior of the order parameter can be described when $T < T_c$ by the critical exponent β in the case of a magnetic system:

$$\langle S(q_s) \rangle = M_0 t^\beta$$

Equation 1-2

$S(q_s)$ is the order parameter of a magnetic system, where the magnetism can be described by a wavevector q_s , t is the reduced temperature (see equation 1-1), M_0 is a constant and β is the critical exponent. (For a clarification of the notation used in describing wavevectors see section 1.3) Also:

$$\chi(t) = \chi_0 t^{-\gamma} \quad T > T_c$$

Equation 1-3

$$\chi'(t) = \chi'_0 t^{-\gamma} \quad T < T_c$$

Equation 1-4

Where $\chi(t)$ and $\chi'(t)$ are the magnetic susceptibilities above and below T_N , χ_0 and χ'_0 are constants and γ is another critical exponent. The exponents defined by the equations

above are known as critical exponents and are examples of universal quantities. Also subject to universality is the amplitude ratio χ_0 / χ'_0 . The temperature dependence of the specific heat can also be described in this way with the critical exponent α , where $C(t) = C_0 t^\alpha$ above the transition and $C(t) = C'_0 t^\alpha$ below.

The cornerstone of the theory of phase transitions is the concept of the order parameter. When the Hamiltonian which describes a system near its critical temperature, is approximated by an expansion expressed in terms of the order parameter, the main results of this theory become apparent. This approach is known as Landau-Ginzburg theory⁶. For a continuous phase transition close to the transition temperature the free energy as a function of the order parameter is very flat around zero (see **figure 1.1**) hence large fluctuations in the order parameter can occur with little or no cost in energy. As the temperature increases the minimum drops and hence the absolute gradient increases.

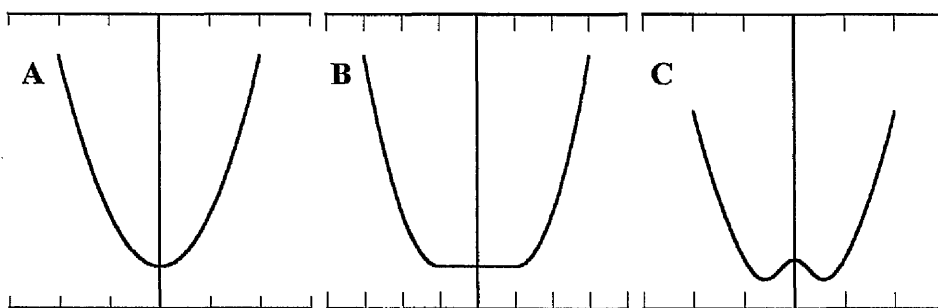


Figure 1.1. Free energy as a function of the order parameter for an example continuous transition. A, is for a temperature a few degrees above the transition. B, very close to, and at the transition temperature. C, a few degrees below the transition temperature.

Physically these large fluctuations in the order parameter correspond to dynamic domains which change rapidly in time and space. Within a given domain there is magnetic order i.e. the order parameter is correlated throughout the domain. The characteristic size of such a domain is called the correlation length, ξ . It is common in theory and experiment to consider the inverse correlation length and its associated power law;

$$\kappa(t) = \kappa_0 t^\nu \quad T > T_c$$

Equation 1-5

$$\kappa'(t) = \kappa'_0 t^\nu \quad T < T_c$$

Equation 1-6

where $\kappa(t)$ and $\kappa'(t)$ are the inverse correlation lengths above and below T_N respectively, κ_0 and κ'_0 are constants and ν is a critical exponent. Fluctuations in the order parameter decay with distance. The scaling theory of phase transitions postulates that there is only one length scale at any given temperature. The fact that the correlation length is divergent at the critical temperature gives an insight into universality. When the correlation length is longer than the range of the interactions described by the microscopic Hamiltonian the properties of the system depend only on the large scale features of the Hamiltonian, the dimensionality of the system and the symmetry group of the order parameter. The theoretical approach known as the renormalisation group has been very successful in predicting the critical exponents for many universality classes.

For systems where the ordering wavevector, q_s in equation 1-2, is zero, (such a system might be ferromagnetism) the order parameter and its fluctuations can be studied directly by bulk probes such as magnetometer measurements. Where the ordering wavevector is non zero, or in the most complex case incommensurate with the crystal lattice, the generalised susceptibility can be probed at any Q with neutron scattering and the details of the transition investigated at that wavevector. (For a clarification of the notation used in describing wavevectors see section 1.3.)

A general feature of continuous phase transitions is that the response time of the system tends to infinity as the transition is approached. The time dependent behaviour at the critical point and the response to time dependent perturbations is much less well understood than the static critical phenomena just discussed. The details of the equation of motion and the mechanisms for the time dependencies in a system are difficult to

measure or explicitly calculate. Dynamic critical phenomena have been discussed in detail in the literature and a scheme for assigning universality classes has been established⁷. It is assumed in this approach that the dynamical response function, $\chi''(\mathbf{Q}, \omega)$, as the system approaches the phase transition can be described by a single characteristic frequency ω_c which is defined by the relation

$$\frac{\int_{-\omega_c}^{\omega_c} d\omega \frac{\chi''(\mathbf{Q}, \omega)}{\omega}}{\int_{-\infty}^{\infty} d\omega \frac{\chi''(\mathbf{Q}, \omega)}{\omega}} = \frac{1}{2}$$

Equation 1-7

This characteristic frequency scales with the correlation length ξ . The prediction being that the scaling is of the form;

$$\omega_c(\xi, \mathbf{Q}) \propto |\mathbf{Q}|^z \Omega^\pm(|\mathbf{Q}|\xi)$$

Equation 1-8

where z is the dynamic critical exponent and Ω^\pm is the scaling factor. In the theoretical exposition of this hypothesis these scaling predictions work well. However, problems arise in real systems. Unlike the static critical phenomena the dynamics cannot be said to be truly independent of the details of the models equations of motion. Deviations from the theoretical Hamiltonian can become dominant in the dynamics. Typically, dipole interactions or small anisotropies in the true Hamiltonian, which are irrelevant in determining the universality class and exponents for the static phenomena, can cause substantial deviations from the theoretical treatment of the dynamic processes.

1.3 The Theory and Practice of Neutron Magnetic Scattering.

Since the vast majority of the work presented in this thesis involves neutron scattering a brief summary of the interesting properties of the neutron along with an introduction to the major features of neutron scattering theory and experiment is presented in this section.

Neutron scattering has for the last few decades provided condensed matter physicists with a tool for investigating the microscopic structure and dynamics of matter. Ordered magnetism within a sample produces peaks in the neutron elastic scattering cross-section in addition to those due to the non-magnetic Bragg reflection of the neutrons by the nuclei. Magnetic scattering of thermal neutrons has revealed complex magnetic structures of local moments in materials with weak bulk magnetic properties. Magnetic reflections can be distinguished from non-magnetic ones by their temperature dependence, they weaken and disappear as the temperature of the sample is raised through the critical temperature at which the ordering vanishes. Magnetic reflections can also be distinguished from non-magnetic ones by the use of polarised neutrons (with polarisation analysis) and their variation with applied magnetic field. Magnetic excitations can be measured by neutron inelastic scattering enabling dispersion relations to be characterised as functions of temperature and wavevector. Fluctuations in fundamental properties of a system which occur close to continuous phase transitions can be characterised enabling important information about phase transitions to be determined. It is also possible to measure information relating to correlations in time directly with the use of polarised neutrons and spin echo techniques.

The de Broglie wavelength of thermal neutrons is comparable to the inter-atomic spacing found in most materials. The wavelike properties of this relatively massive particle were demonstrated in 1936 only four years after its discovery. In addition, the energy of

readily available thermal neutrons relates directly to the energies found in common excitations, (phonons etc.). Moreover, along side these two fundamentally attractive properties the neutron also carries with it a magnetic moment which makes it possible to study magnetic structure, excitations and dynamics. Energies associated with magnetic excitations are typically of the same order as those associated with phonons. It is also worth reiterating that the neutron has no electrostatic charge. It is this property that enables us to take advantage of the previously mentioned assets as it allows the neutron to penetrate deeply into most condensed matter systems without provoking any structural or chemical change. This same property made the neutron an elusive particle and delayed its discovery until 1932. Neutrons interact with both the atomic nuclei, via the strong interaction, and with any microscopic magnetic fields within the sample, a direct consequence of the neutrons magnetic moment. It is the interaction with, and the information that is produced about, the magnetism of a sample that this thesis is primarily concerned with. The neutron interacts with both the nuclear and the atomic magnetic moment. The interaction with the nucleus is very small as a result of the relative sizes of the Bohr and nuclear magnetons and hence the dominant interaction is that due to the unpaired electrons which is of comparable size to the interaction with the chemical structure.

What follows is a simple summary of the relevant theoretical results. A full theoretical derivation can be found in one of the many standard texts on the subject. (Lovesy⁸ is a full and comprehensive treatise.) The remaining parts of this section give some brief information on how a neutron measurement is achieved and the two types of neutron source used in the experiments presented in this thesis.

Firstly, we establish an environment within which a discussion of neutron scattering from crystals can be undertaken. **Figure 1.2A** and **B** shows a schematic of real space and the

reciprocal space equivalent in a simple crystal showing the set of reflecting planes in real space which give rise to diffraction points in reciprocal space.

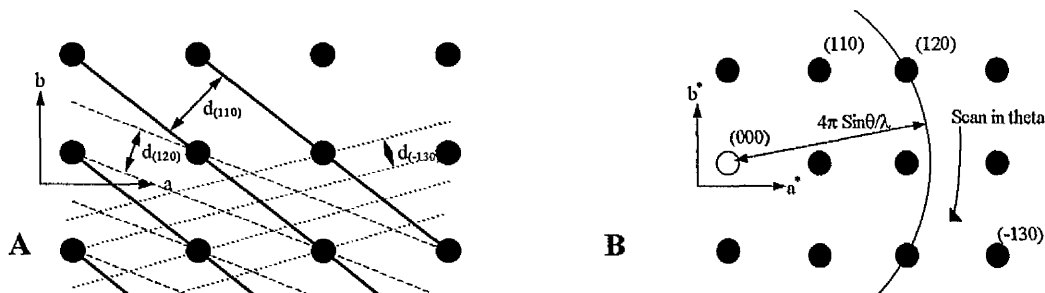


Figure 1.2 **A** shows a real space representation of a crystal where the points indicate atomic positions. The sets of Bragg reflecting planes are labelled with miller indices (hkl) . — (110) set of planes, ---- (120) set of planes, (-130) set of planes. **B** shows the reciprocal space equivalent. Here the points correspond to the position in reciprocal space where the diffraction condition for a set of planes in real space is satisfied. The axes a^* and b^* are in units of $2\pi/a$ and $2\pi/b$. A scattering experiment performed using an incident beam of wavelength λ and rotating θ (the Bragg angle) would describe the arc shown centred at (000) .

This picture of diffraction can be more conveniently described by wavevectors, denoted k which then modifies the reciprocal space image to that shown in **figure 1.3** where a typical scattering process (in this case elastic) is shown.

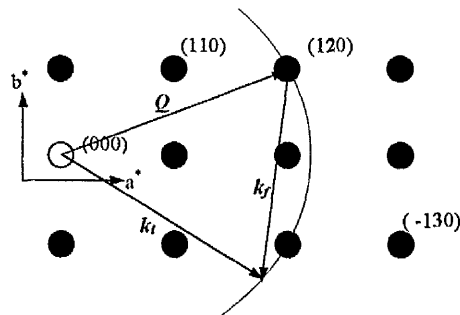


Figure 1.3 A vector diagram showing a typical scattering process in reciprocal space. Where $|k_i| = |k_f|$ in this case (elastic scattering). Q is a vector 'pointing' to a general position in reciprocal space. In this case the elastic scattering observed is that due to the Bragg scattering from the set of planes in real space which make the point (120) in reciprocal space. The reduced wavevector, q , is zero (see explanation in the main text).

The theory of neutron scattering is complex and involved. It is appropriate here to just touch on its major features. The quantity that is measured in a neutron scattering experiment is the partial differential cross-section which gives the probability of a neutron being scattered into a solid angle, $\delta\Omega$ with a final energy between E' and $E' + \delta E'$. This cross-section for a condensed matter system can in general be written as;

$$\frac{\delta^2 \sigma}{\delta\Omega \delta E'} = \frac{|k_f|}{|k_i|} S(\mathbf{Q}, \omega)$$

Equation 1-9

Where k_i and k_f are the incident and scattered neutron wavevectors respectively. $S(\mathbf{Q}, \omega)$ is the scattering function or scattering law. It contains all the information about the properties of the system which contribute to the scattering cross-section. This part of the cross-section is a function only of the change in wavevector \mathbf{Q} , which is defined as $k_i - k_f$, and the change in energy $\hbar\omega = (\hbar^2 / 2m_n)(k_i^2 - k_f^2)$, where m_n is the mass of the neutron. These two terms are more usually called the wavevector transfer and the energy transfer. In this thesis \mathbf{Q} will be used for the neutron wavevector transfer and \mathbf{q} for the reduced wavevector so $\mathbf{q} = \mathbf{Q} - \mathbf{G}$ where \mathbf{G} are the vectors of the reciprocal lattice, it is \mathbf{q} that more often than not is the subject of any theory. The interaction of the neutron with matter is sufficiently weak as enable the Born approximation to be employed. This greatly simplifies the theory as all interactions can be averaged over as each is presented with an identical initial state. The magnetic part of the scattering function for an unpolarised incident neutron beam can then be expressed in the dipole approximation as ;

$$S(\mathbf{Q}, \omega) \propto [f(\mathbf{Q})]^2 \exp\{-2W(\mathbf{Q})\} \sum_{\alpha\beta} \left(\delta_{\alpha\beta} - \frac{Q_\alpha Q_\beta}{|\mathbf{Q}|^2} \right) S^{\alpha\beta}(\mathbf{Q}, \omega)$$

Equation 1-10

where uninteresting constants have been factored out. The sum over α and β is over the Cartesian component of the spins, $S^{\alpha\beta}(\mathbf{Q}, \omega)$ is the Fourier transform in time and space of the correlation function between spin densities at sites i and j , $\langle \sigma_i^\alpha(t) \sigma_j^\beta(0) \rangle$. The

exponential term is the Debye-Waller factor arising from thermal motion of the scattering centres in the crystal. At the wavevectors used in the experiments described in this thesis it is considered constant. $f(\mathbf{Q})$ is the magnetic form factor and where applicable has been approximated by the exponential term, $\exp\{-\alpha|\mathbf{Q}|^2\}$, where α is a system dependent term. The magnetic form factor varies slowly with \mathbf{Q} falling off at high $|\mathbf{Q}|$. The orientation factor in the sum arises due to the complex vector nature of the magnetic form factor, only components of the spins perpendicular to the scattering vector contribute to the cross-section. It is worth noting that this is not the case for Bragg scattering from the chemical structure where the form factor is a complex scalar. The value of equation 1-10 lies in the interpretation of the correlation function. If the Born approximation can be assumed and the response of the system to the neutron is linear then the correlation function can be related to the complex part of the macroscopic response function, the generalised susceptibility. The generalised susceptibility measures the response of the system to spatially and temporally varying magnetic fields and hence holds all the information we require of the magnetic statics and dynamics. If it is desired the time dependent part can be separated out and the inelastic part of the scattering function can be written in terms of the spectral weight function. $F(\mathbf{Q}, \omega)$:

$$S^{\alpha\beta}(\mathbf{Q}, \omega) \propto \chi_Q^{\alpha\beta} \beta \omega [1 + n(\omega)] F^{\alpha\beta}(\mathbf{Q}, \omega)$$

Equation 1-11

$\beta = 1/k_B T$, All the information regarding the spin dynamics is contained within the normalised spectral weight function. It is this function which is modelled in the treatment of spin dynamics in chapter 3.

Measurement of the scattering function is the aim of any neutron scattering experiment. If we confine the discussion here to only the most general features of any neutron experiment we can see how such measurements are achieved. Scattering experiments fall into two categories, elastic and inelastic scattering measurements. The former being diffraction measurements and the latter being spectroscopic in nature. The experiment in

chapter 2 uses elastic scattering conditions to measure energy integrated inelastic scattering. This is a common technique used when investigating inelastic processes where all the information sought is contained within an energy integrated elastic scattering function. Measurement of $S(Q)$ requires the diffractometer to be set up to detect all neutrons at a specific scattering angle but to be indiscriminate about the energy of the scattered neutrons. This means that all inelastic processes of energy transfer less than the energies of the incident neutrons are integrated over. Unfortunately a change in the neutron energy causes a change in the wavevector transfer Q . We can consider the effects of this on measurement of critical scattering (which is the subject of chapter 2). A characteristic frequency can be assigned to the critical fluctuations, ω_{crit} . The change in Q is then given by $\delta Q = k' \hbar \omega_{crit} / (2E')$, this must be kept small if a reliable energy integration is to be made. By happy coincidence the theory of critical phenomena predicts that $\omega_{crit} \rightarrow 0$ as $T \rightarrow T_c$, and since the errors produced in neutron energy gain and loss tend to cancel the results are more accurate than might be expected⁹. This is known as the *quasi-static* or *quasi-elastic* approximation. It is still prudent to keep the energy of the incident neutrons as high as possible to minimise the change in Q .

In the inelastic case where measurement of $S(Q, \omega)$ is desired the final wavevector is selected from all possible energies by the use of an analyser which selects out a specific wavelength and is positioned before the detector. The experiment described in chapter 3 used inelastic scattering to measure $S(Q, \omega)$ from which the correlation function is extracted through a Fourier transform. The neutron experiments described in chapter 4 are all simple diffraction experiments.

1.3.1 Reactor Sources (Risø and the ILL).

The experiments described in chapter 2 and chapter 3 and the last experiment described in chapter 4 were performed at the Institut Laue Langevin (ILL) high flux reactor. This reactor had recently been shutdown for three years to enable a reactor refurbishment

programme to be undertaken. A natural consequence of this was a shift in the international neutron scattering community to other sources, most notably the ISIS Spallation source in the UK and a clutch of smaller research reactors dotted around the world. The ILL reactor came back on line in 1995 and has once again become the world leading neutron source enabling many experiments that were unable to be performed without the high flux of the ILL to be carried out. The reactor operates at a thermal power of 57MW. A single fuel element sits in a heavy water (D_2O) moderator which reflects some of the neutrons back into the fuel element to sustain fission. Biological shielding is provided by a light water swimming pool assembly. The thermal flux moderated by the D_2O (at 300K) has a Maxwellian velocity distribution with a peak at 1.2\AA . This profile can be modified for certain instruments by hot or cold sources made of graphite (at 2400K), or deuterium (at 25K) respectively. Neutrons are available from all sources in the reactor hall and via guides up to 120m in length in two guide halls. Up to 35 instruments are supplied with neutrons at any one time.

The Danish National Laboratory has a research reactor (DR3), based in Denmark at Risø, which was used in the experiment described in chapter 4, section 4.2.4. The Risø reactor has a lower power rating (10MW) and fewer instruments than the ILL but the neutron production and moderation process is essentially the same as at the ILL.

1.3.2 The Spallation Source (ISIS).

ISIS is, at the time of writing, the worlds most powerful pulsed spallation neutron source. Neutrons supplied by ISIS were used for several of the experiments discussed in chapter 4. The proton beam also produced the muons used in the experiment described in section 4.2.5. The source is based around a high intensity proton synchrotron. The intensity is $\sim 2.5 \times 10^{13}$ protons per pulse at a pulse rate of 50Hz (200 μ A mean current). The protons are impacted upon a heavy metal target (uranium or more commonly tantalum) to produce, by the process of spallation, $\sim 4 \times 10^{16}$ high energy neutrons per

second. The fast neutrons are moderated by either ambient water or liquid methane (at 100K) placed close to the target. The moderators slow the fast neutrons to thermal velocities broadening the pulse to lengths to $\sim 1\text{-}100\mu\text{s}$. The thermal neutrons pass through one of eighteen holes in the massive concrete and steel shielding to surrounding instruments either directly or via neutron guides. The muon beam is produced by inserting a graphite target in the proton beam before the main neutron producing target. This generates pulses of muons (with only a small reduction in the beam intensity). The muons are then guided to the instruments by magnetic fields. The data collected during a neutron experiment using ISIS is characterised generally by its Q , the position in the reciprocal space of the sample, and, in an inelastic experiment, its time of arrival at the detector relative to the proton beam pulse, which when combined with the flight path length enables the final energy, and hence the energy transfer of the neutron to be determined. The two neutron experiments performed at ISIS in chapter 4 were both simple elastic ‘white’ beam experiments where no energy analysis was performed. Because of the vast amount of data it is possible to produce during an experiment at a pulsed source the ISIS staff have produced a series of programs designed to enable the experimenter to access quickly the specific details they require. These programs of basic data manipulation go under the collective name of GENIE¹⁰ and will be referred to in chapter 4.

1.4 References.

- ¹ Binney J.J., Dowrick N.J., Fisher A.J. and Newman M.E.J. "The theory of critical phenomena." pp228. Oxford University Press, Oxford. (1992)
- ² Stanley. H.E. "Introduction to Phase Transitions and Critical Phenomena" Clarendon press, Oxford. (1971)
- ³ Binney J.J., Dowrick N.J., Fisher A.J. and Newman M.E.J. "The theory of critical phenomena" Oxford University Press, Oxford. (1992)
- ⁴ Collins M.F. "Magnetic critical Scattering" Oxford University Press, Oxford. (1989)
- ⁵ Cowley R.A. "Neutron and Synchrotron Radiation for Condensed Matter Studies" Volume 2. pp137 Springer-Verlag. (1994)
- ⁶ Binney J.J., Dowrick N.J., Fisher A.J. and Newman M.E.J. The theory of critical phenomena pp178. Oxford University Press, Oxford. (1992)
- ⁷ Hohenberg P.C., and Halperin.B.I., Rev Mod Phys **49** pp435 (1977)
- ⁸ Lovesey S.W. "Theory of Neutron Scattering from Condensed Matter" Vol 1 and 2. " Oxford University Press, Oxford. (1987)
- ⁹ Cowley R.A. "Neutron and Synchrotron Radiation for Condensed Matter Studies" Volume 2. pp154 Springer-Verlag. (1994)
- ¹⁰ David W.I.F., Johnson M.W., Knowles K.J., Moreton-Smith C.M., Crosbie G.D., Campbell E.P., Graham S.P. and Lyall J.S. PUNCH GENIE Manual "A Language for Spectrum Manipulation and Display", R.A.L. publication. RAL-86-102 (1986).

Chapter 2. Critical Exponents for the Paramagnetic to Helimagnetic Transition in Holmium.

2.1 Introduction.

The motivation for this experiment was to clarify the nature of one of the principal magnetic phase transitions in holmium. Holmium undergoes a magnetic phase transition from a paramagnetic state to a 'helimagnetic' state at $\approx 132\text{K}^1$. This phase transition is not well understood, theoretically or experimentally. Holmium is one of three elemental c-axis helimagnets, the other two being dysprosium and terbium. It is expected that these three systems would be described by the same universality class, (the groupings used to describe all continuous transitions) and critical exponents. However, the experimental evidence provides conflicting values of the critical exponents. This is due to the complicated nature of critical scattering experiments in the c-axis helimagnets. Theoreticians have failed to agree on the universality class of the transition, and where agreement is found in the universality class the calculated exponents have been different. It was our aim to provide definitive values of the critical exponents γ and ν , overcoming the inherent difficulties in experiment and analysis by applying methods of data analysis and experimentation learned from previous efforts and as a result differentiate between the proposed theories.

2.2 The Magnetic Structure of Holmium.

Holmium is a heavy rare-earth metal which, in common with all other heavy rare-earth elements (except ytterbium) exhibits states of magnetic order when in the form of pure metal. A comprehensive discussion of rare-earth magnetism can be found in Jensen and Mackintosh². The metals terbium, dysprosium and holmium crystallise in the hexagonal-close-packed structure. The 4f moments are constrained by the local anisotropy to lie in the a-b plane, and are assumed to have the symmetry of the x-y model. There may be some in plane six-fold (or higher) anisotropy but this can be shown to be irrelevant as far as the phase transitions are concerned³. These materials order helimagnetically (at $\approx 132\text{K}$ in the case of Ho) with the moments in the basal plane ordering ferromagnetically but with a turn angle between neighbouring layers which gives an incommensurate modulation along the c-axis. This arises due to the coupling of the moments via the conduction electrons (the RKKY interaction). The modulation wavevector corresponds to a peak in the conduction band susceptibility. A representation of the helimagnetic state is shown schematically in **figure 2.1**

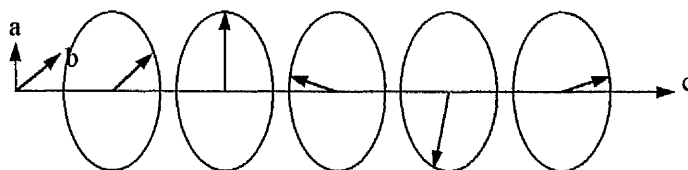


Figure 2.1. A schematic representation of the spin arrangement in a c-axis helimagnet, with each spin on the c-axis representing the ferromagnetic a-b plane layer.

At lower temperatures further magnetic arrangements are possible. These magnetic structures are complex and have been determined by neutron diffraction on single crystals^{4,5}. The principal transitions are from a paramagnet to helimagnet at 132K (the subject of this work) and from helimagnetic to a conical structure (at 20K) where the spins are no longer constrained to lie in the a-b plane. The helical structure in **figure 2.1**

becomes conical. The magnetic structure of the helimagnetic phase of holmium is such that the ordered magnetism produces peaks in the elastic neutron cross-section at sites $(h\ k\ l \pm \tau)$, satellites to the magnetic zone centre where h , k and l are the indices of the Bragg reflections due to the hexagonal-close-packed chemical structure of holmium.

2.3 Previous Experiments and Theoretical Predictions.

There have been many attempts to determine theoretically the model which best describes the high temperature transition in the helimagnets. In the early days, Bak and Mukamel⁶ confidently asserted that the paramagnetic-helimagnetic transition is characterized by a four component order parameter. They calculated the exponents to be $\beta=0.39$, $\gamma=1.39$ and $\nu=0.70$. Barak and Walker⁷ later concluded that the transition was first order, against the bulk of experimental evidence, although there is some support from dilatometry of some weak first order behavior⁸. More recently Kawamura⁹ asserted that the chirality inherent in helimagnetic order spoils the earlier arguments, and predicted exponents of $\beta=0.25$, $\gamma=1.1$ and $\nu=0.53$. Recent studies, using a $2+\epsilon$ expansion of a nonlinear σ model¹⁰, conclude that the transition could be first order, or second order with Ising or tri-critical mean-field exponents, depending on the residual anisotropies, which are usually ignored. All of these theoretical predictions claim some experimental validation, indicating the difficulty of such an experiment. A summary of theoretical predictions is presented in **table 2.1**.

Theory	α	β	γ	ν
Universality class: $d=3, n=4$ (i) ⁶	-0.17	0.39	1.39	0.7
(ii) ¹¹	-0.22	0.39	1.47	0.74
Chiral ⁹	0.4	0.25	1.1	0.53
Tri-critical mean field ¹²	0.5	0.25	1	0.5
First order ⁷	-	-	-	-

Table 2.1. A summary of the theoretical predictions for the critical exponents in the helimagnets.

Experimental measurements of the critical exponents show a range of values for the helimagnetic elements, terbium, dysprosium and holmium, e.g. $\beta=0.25(13)$ to

$\beta=0.39(14)$. Many authors note the difficulty of obtaining reliable values of β from neutron data but more recently, due to high resolution neutron and x-ray work, a further complication has been discovered with the appearance of a second, apparently Lorentzian squared profile central peak close to T_N ¹⁵. This feature may be associated with random defects or impurities enabling order to persist beyond the transition temperature. A summary of the main experimental results is given in **table 2.2**. We can see that the spread of results is vast with values of the exponent α being given as ± 0.2 . There is a distinct lack of consistency across the three elements where all the theoretical indications are that the three belong to the same universality class.

The scattering experiments can be put into three categories depending upon the treatment of the Lorentzian squared shaped central peak. This may account for the differences in the values of the exponents across these experiments. Firstly there are those early experiments where the resolution was broad and the central peak has been indistinguishable from the bulk scattering hence no account of it has been taken in the analysis. Secondly the central peak has been fitted to a Lorentzian squared profile (discussed in much of the literature as a second length scale) superimposed upon the critical scattering. The critical scattering part has then been used to calculate the exponents¹⁹. Finally in the case of Thurston et al¹⁹ the central peak itself has been used to calculate the exponents to demonstrate the exponents measured if the central peak is considered in the same way as critical scattering. The use of the Lorentzian squared profile peak has little real physical basis. The discussion of a second length scale brings into doubt the whole theory of universality and scaling, a theory which up to now has been extremely successful. In the analysis of the experiment we have performed we have assumed that the central peak is the result of $1/|q|^2$ divergent spin wave scattering (an acknowledged feature below T_N) resulting from persistent order pinned at defect sites.

	α	β	γ	ν
<u>Terbium</u>				
Specific Heat ¹⁶	0.20(3)			
Neutron Scattering.		0.25(1)		
Neutron Scattering				0.53
Neutron scattering (c.p. only)			1.6	1.3
<u>Holmium</u>				
Specific Heat ¹⁷	0.27(2)			
Specific Heat	0.16(6)			
Neutron Scattering ¹⁴		0.39(3)		
Neutron Scattering ¹⁸			1.14(10)	0.57(4)
Neutron Scattering ¹⁹		0.37(10)	1.24(15)	0.54(4)
Neutrons and X-ray (c.p) ¹⁹		0.37(10)	2-5	1.0(3)
<u>Dysprosium</u>				
Specific Heat ²⁰	-0.2			
Specific Heat ²¹	0.18			
Specific Heat ²²	0.24			
Mößbauer Spectroscopy		0.335(10)		
Neutron Scattering		0.39(2)		
Neutron Scattering ¹⁸			1.05(7)	0.57(5)

Table 2.2. A summary of experimentally measured values of the critical exponents in the helical antiferromagnets.

2.4 Experiment.

When a neutron scattering experiment is performed the data collected gives a measure of the scattering function for a given point in reciprocal space and energy transfer (a measure of the inelasticity of the interaction). This is usually denoted by $S(\mathbf{q}, \omega)$ i.e. the scattering function at the reciprocal space co-ordinates q_x, q_y, q_z with energy transfer ω .

As in any scattering process interactions can be elastic or inelastic. In the critical region there is scattering from the dynamic fluctuations within the sample which can be observed given the correct experimental conditions. These fluctuations give rise to a finite scattering function at energy transfers other than zero i.e. an inelastic spectrum. The function which describes such scattering is usually characterised by a Lorentzian energy profile described by:

$$S(\mathbf{q}, \omega) = \left(\frac{\chi^2 \kappa^2}{\kappa^2 + q^2} \right) \cdot \left(\frac{\Gamma}{\Gamma^2 + \omega^2} \right)$$

Equation 2-1

Where Γ is the energy width and the reduced temperature dependent terms κ and χ have been defined in chapter 1, section 1.2. If this quantity is measured by a series of constant Q scans in energy at a range of temperatures in the critical region the exponents γ and ν can be deduced.

Constant Q scans can only be achieved using a 'triple axis' spectrometer which can select a discrete value of Q and ω . However this is time consuming and in the final analysis the information about γ and ν is fully held in data that has been integrated over all energies. It is efficient to use a 'two axis' instrument where the final energy is not selected discretely but all energies are collected simultaneously, therefore performing the integration experimentally. This has the additional advantage in data analysis of reducing

the resolution function from a four dimensional hyperellipsoid to a three dimensional ellipsoid. The form of the scattering then becomes

$$S(\mathbf{q}) = \frac{\chi^2 \kappa^2}{\kappa^2 + |\mathbf{q}|^2}$$

Equation 2-2

The assumption being that the experimental integration over energy is sufficient to be considered infinite. It is prudent to measure the energy width in triple axis mode at some sample scans to ensure this full energy integration is being performed.

Holmium metal crystallizes in the hexagonal-close-packed system with unit cell dimensions $a=3.58\text{\AA}$, $b=3.58\text{\AA}$, $c=5.63\text{\AA}$. Experiments of this nature must be performed on a single crystal. We used a large, $\approx 1.5\text{cm}^3$, slab shaped crystal provided by D.McMorrow of the Danish National Laboratory in Risø.

2.4.1 The Triple-Axis Spectrometer IN8.

The experiment was performed in Grenoble at the Institut Laue Langevin (ILL) high flux reactor neutron source on a three axis spectrometer, IN8. A diagram of the instrument is shown in **figure 2.2**. It is called a triple-axis spectrometer as the neutron beam is scattered at three elements all of which pivot around a vertical axis. The monochromator can be considered to be a large single crystal chosen such that an intense Bragg reflection can be used to select a specific energy, calculated from the Bragg equation, to be incident on the sample. The now monochromatic beam is then scattered from the sample which is set at a specific angle to fulfill the scattering condition for the point in reciprocal space which is to be investigated. The beam leaving the sample can then be scattered by the analyser, which again can be considered to be another large single crystal. This enables a specific energy to be selected from the scattered beam. In reality both the monochromator and analyser are made up of many single crystals. This enables artificial broadening of the mosaic structure to optimise the use of the available neutron beam. In

the 3-axis configuration the incident and final wavevectors are known and can be selected by the operator. This gives the experimenter the ability to pick a specific point and energy transfer in reciprocal space to investigate inelastic scattering. The analyser can be removed and the instrument used in 2-axis mode. The detector is then rotated around the point labelled 3rd AXIS, in the diagram until the beam scattered from the sample is directly incident on the detector. This is the usual arrangement for investigating elastic scattering i.e. the initial and final wavevectors of the beam are assumed to be the same. The spectrometer was used in 2-axis mode (no analyser) for the majority of this experiment.

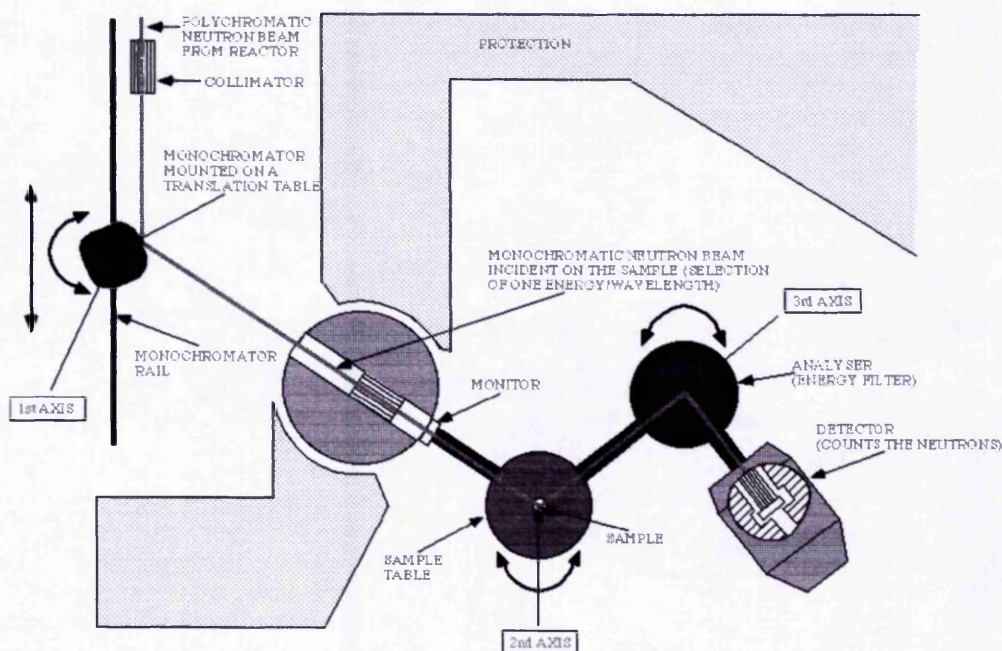


Figure 2.2. Diagram of IN8²³. The triple axis spectrometer at the ILL shown here in 3 axis mode. The analyser can be removed and the detector rotated about axis 3 until it coincides with the reflected sample beam.

2.4.2 Collection of Data.

A reciprocal space map of the area studied in this experiment is shown in **figure 2.3**, where the satellites studied are shown. It is at and around these satellite positions that critical phenomena can be observed. The sample was aligned with the $[002][100]$ plane as the scattering plane. The (100) and the (002) are purely structural Bragg points.

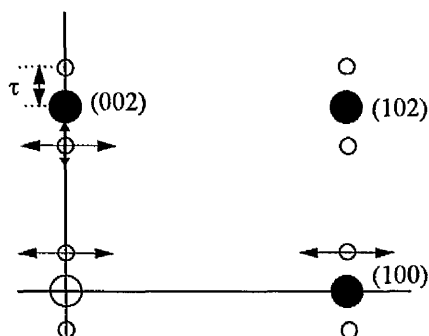


Figure 2.3. A map of reciprocal space. The structural Bragg points are shown as ●, and the magnetic satellites as ○. The satellites studied in this experiment have a double headed arrow through them showing the scan directions.

Data from this experiment can be seen in **figure 2.4** which shows data collected from the $(002 \pm \tau)$ satellites. In **figure 2.4A**, the two peaks are critical scattering. The sample was above its transition temperature and so the peaks are of a Lorentzian shape. The data at the centre of the scan is the Gaussian profiled structural Bragg peak, the (002). This has its maximum value greater than 170,000 counts showing the relative magnitude of the critical scattering (1000 counts). The satellites are a result of critical fluctuations and are therefore strictly speaking an inelastic phenomenon. **Figure 2.4B**, and **C** show scans through the magnetic satellite position $(002 - \tau)$ orthogonal to the scan in **2.4A**. **Figure 2.4B** shows purely critical scattering above T_N while **2.4C** shows the critical scattering with the elastic magnetic satellite contribution imposed upon it. Again this demonstrates the relative magnitudes of the fluctuating and ordered components of the scattering.

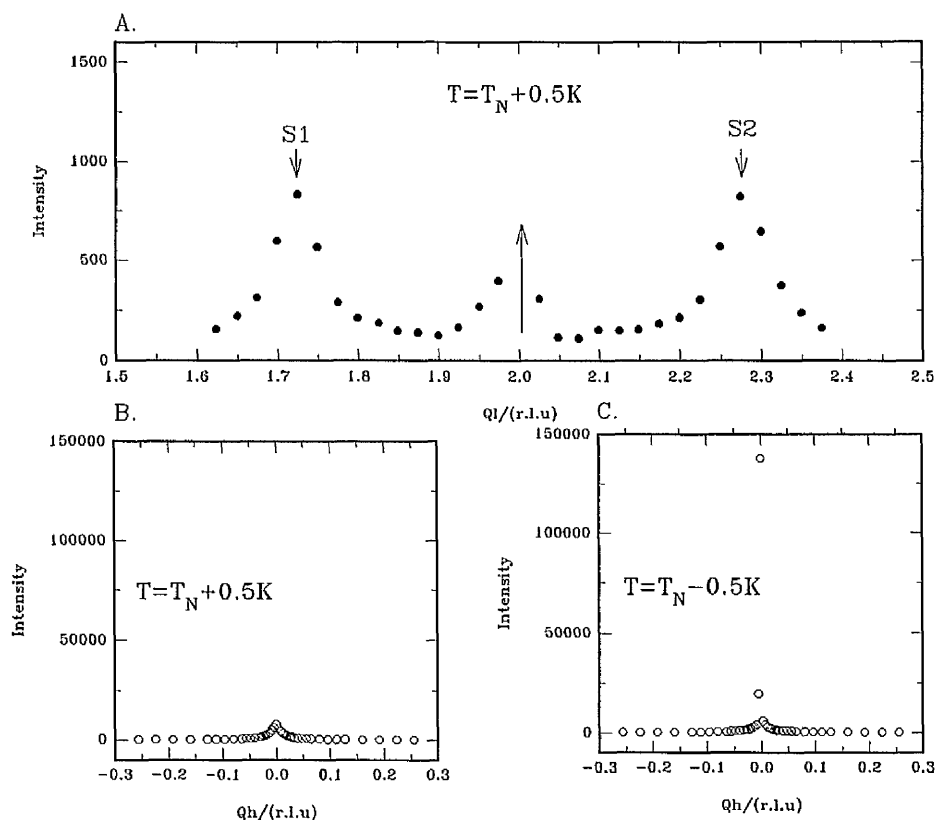


Figure 2.4. Sample data from the (002) satellite used experimentally for alignment purposes only. **A** shows a radial scan through the (002) and its two satellites. **B** and **C** show transverse scans through the (002- τ) satellite above and below the critical temperature.

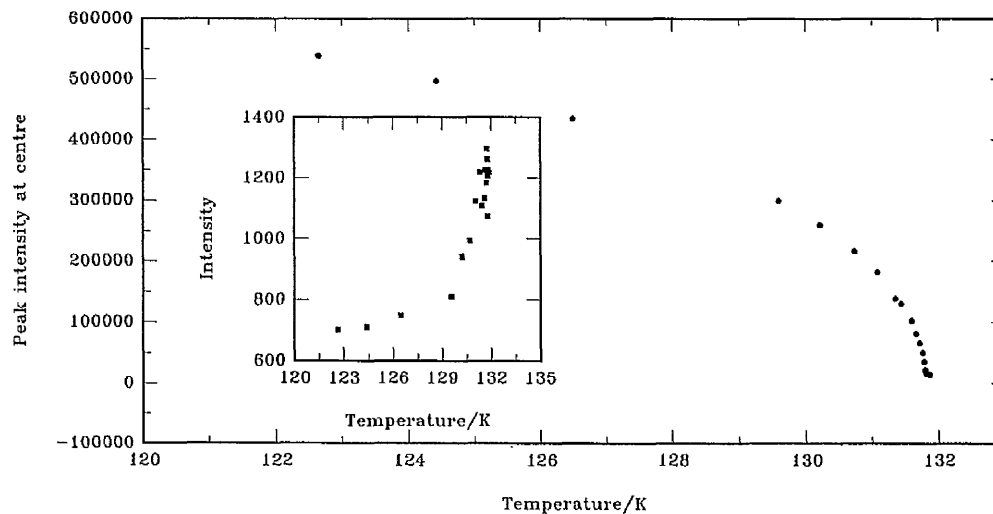


Figure 2.5. Shows the temperature dependence of the ordered magnetism, the satellite peak intensity with, inset, the temperature dependence of the fluctuating component, the critical scattering.

A series of scans in temperature enabled the magnitude of the critical and Bragg scattering to be monitored as a function of temperature and so the transition temperature be located at 131.88K. (See **figure 2.5.**)

The bulk of the data collected during this experiment consisted of scans directly through the satellite positions at a nominal energy transfer of zero. Scans through three satellites were performed at 40 different temperatures encompassing a range of $T_N \pm 10\text{K}$, spanning four orders of magnitude in reduced temperature, spaced in a logarithmic manner. Each satellite at each temperature was scanned several times to enable higher densities of points at the centre of the scan than at the wings. Scan sets taken at smaller reduced temperatures contain more data points than those at large reduced temperature reflecting the broad nature of the critical scattering at large reduced temperatures. For each nominal reduced temperature a single radial scan was performed through the (002- τ) satellite this was to enable accurate determination of the temperature dependence of τ . Temperature stability is a major problem during this type of experiment. If reduced temperatures of 0.005 were to be achieved good thermal contact of the sample with the cryostat and well behaved electronic control systems are vital. Unfortunately there existed temperature drift in all scans. The stabilisation time was very long so it was decided to take data with this drift and in the modelling procedure fit each point with an individual temperature.

2.5 Data Fitting and Results.

2.5.1 The Triple Axis Simulation and Fitting Program.

Analysis of neutron data requires careful consideration of the elements which contribute to the observed data. The spectrum in the raw data consists of the resolution function of the instrument convoluted with $S(\mathbf{q}, \omega)$ which contains the physics of the sample. A program we have developed at Manchester enables a full numerical convolution of a calculated resolution function, which is a four dimensional hyperellipsoid in \mathbf{q}, ω space and a three dimensional ellipsoid in \mathbf{q} space, with a parameterised model scattering function, to achieve a full simulation of the data. The main elements of this process are laid out here. A more detailed exposition of the original program can be found in Lloyd's thesis²⁴.

The resolution function is modeled as a Gaussian-profiled probability density function which describes the deviations a neutron can take from a nominal trajectory (which is determined by the setting of the spectrometer). The function is artificially limited in \mathbf{q} to points only where the function is greater than e^{-3} of the maximum value. This gives the function an ellipsoid form (hyperellipsoid in 4 dimensions). The total intensity of neutrons detected at a given setting is then the sum of the scattering function over all possible paths a neutron can take weighted with the probability density function which is expected to be a maximum at the nominal path. Any given path can be described by its wavevector and energy transfer hence the sum over all these paths can be expressed as an integral over energy and wavevector transfer giving:

$$I(\mathbf{q}, \omega) = \iint_{\Delta\mathbf{q}, \Delta\omega} S(\mathbf{q} + \Delta\mathbf{q}, \omega + \Delta\omega) R_0(\mathbf{q}, \omega) \exp\left\{-\frac{1}{2} \mathbf{x} \cdot \underline{\mathbf{M}} \cdot \mathbf{x}\right\} d(\Delta\mathbf{q}) d(\Delta\omega)$$

Equation 2-3

Where $\mathbf{x}=(\Delta\mathbf{q}, \Delta\omega)$, $R_0(\mathbf{q}, \omega)$ is a resolution correction, $\underline{\mathbf{M}}$ is, in the four dimensional case a 4×4 and in the 3-D case a 3×3 symmetric matrix with its elements being calculable from known instrument parameters. It is worth noting that this is an approximation to the real resolution function which is known to be centrally weighted and symmetric but is not by necessity Gaussian (the transmission profiles of Söller collimators are known to be triangular). The ‘clipped’ Gaussian approximation is the result of a speculative application of the central limit theorem, encouraged by fits to well characterized scatterers.

As always neutron scattering data are subject to Poisson statistics. The fitting part of the program employs a maximum likelihood process to compare a given measured $S(\mathbf{q}, \omega)_{obs}$ to $S(\mathbf{q}, \omega)_{calc}$ calculated using the values of parameters P_0, P_1, \dots, P_x . The probability of obtaining a set of data points I_i^{obs} given a predicted model set of points Y_i^I for N points is given by:

$$P_{prob} = \prod_{i=1, N} \frac{Y_i^I}{I_i^{obs}} \exp\{-Y_i^I\}$$

Equation 2-4

The parameters P are varied using a Newton-Raphson method of iteration to maximize this probability. This then provides the basis of our analysis.

The integral described in equation 2-3 must be performed for every unique set of \mathbf{q} and ω values. In general this integral is performed numerically. The integration is achieved using a grid of points arranged in an hyperelliptical coordinate system with the density of the points higher near the centre of the hyperellipsoid, reflecting the probability density function. The number of points in this grid can be set to reflect the smoothness of the data. The data from this experiment were collected using no energy analysis. The critical scattering information we required was fully contained within the integrated scattering cross-section (although inelastic in origin). The simulation of these data required the

modification of Lloyd's code to make the appropriate transition from a four-dimensional resolution function to a three-dimensional one. To simplify this conversion and to maintain a consistency of approach within the original code written by Lloyd several approximations were used. Firstly it was assumed that the extent of the real resolution function in energy could be considered infinite. This assumption was made when the experiment was performed and is central to having a full description of the critical scattering contained within the energy integrated scattering spectrum. The validity of this approximation is contained wholly within the relative magnitude of the energy of the incident neutrons and the energy width, Γ , of the scattering. (See equation 2-1 and the discussion of energy integrated scattering at the end of section 1.3). Secondly, the resolution function extends into energy space in the form of a 'pipe' inclined at the same angle as the major axis of the four dimensional hyperellipsoid. The function is shown schematically in **figure 2.6** where the solid lines forming tangents to the ellipsoid form the sides of the 'pipe'. The angle of inclination of the ellipse is a complex function of q (and energy in the inelastic case.)

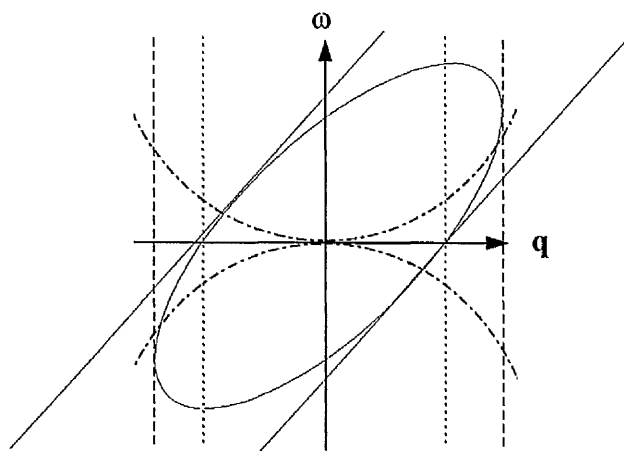


Figure 2.6. A schematic representation of the four dimensional resolution function where the three dimensions of q are collapsed onto the x axis. The elliptical 4-D function is shown with the effect of removing the analyser shown by the 'pipe' parallel to the major axis of the ellipse. The first order approximation to this (the caliper width) is shown as a dashed line. The approximation used is shown as a dotted line, the zero energy width. The dot-dash line shows the spread of the scattering into the energy domain.

The resolution simulation program effectively projects a vertical 'pipe', shown in **figure 2.6** as dashed lines, onto the q axis. It can be seen that while the scattering remains symmetrical (as the diagram shows) then any losses due to this approximation at positive q are offset by a gain at negative q . We assume that where symmetry is lost the scattering is weak enough to be negligible. Finally, the width of the area in q over which we are suggesting the resolution function should extend is wider than the width simulated in the resolution calculation this is justified with reference to **figure 2.6**. The four dimensional resolution function ellipsoid is shown as it would extend into the energy domain if this was a three axis inelastic experimental configuration. The absence of the analyser reduces this representation from an ellipse in q, ω space (as it is shown) to a 'pipe' (of infinite extent). This is then approximated not to the caliper width in q (dashed lines) but the width shown by the dotted lines. This is the width of the resolution function at $\omega=0$, the zero energy width. (The magnitude of the approximation is somewhat exaggerated for clarity in the schematic **figure 2.6**.) This approximation means that the four dimensional problem can be reduced to three dimensions mathematically, saving valuable computer resources. The approximation is not as brutal as it first appears. The nature of the energy dependent scattering is outlined in **figure 2.6** by the dot-dash line. This is somewhat misleading as at relatively large $|q|$, where the approximation is most gross, the scattering is much reduced by the denominator terms in equation 2-1. The form of the energy dependent scattering and its q dependence can be seen in **figure 2.7**, a graphical representation of equation 2-1. This approximation was rigorously tested by programs written by the author which numerically integrate the energy dependent function shown in **figure 2.7** convoluted with the calculated resolution function for a range of q widths corresponding to the zero energy width and larger. The intention was that, if necessary, the calculated resolution function could be broadened by the convolution of another resolution element to simulate any extra width due to any shortcomings of approximating the caliper width to the zero energy width. These simulations

showed that the approximation was valid with a full description of the scattering gained at widths equivalent to the zero energy width. For the purposes of the simulations the energy width, Γ was estimated by fitting an inelastic data set taken during the experiment. (see **figure 2.11** page 50.) At this stage physically realistic values of the other variables were used rather than the final fitted values as these were not known. These simulations gave insight into the validity of the approximations used but also the programs could be used to cross-check the final fitted data for the continuing integrity of these approximations.

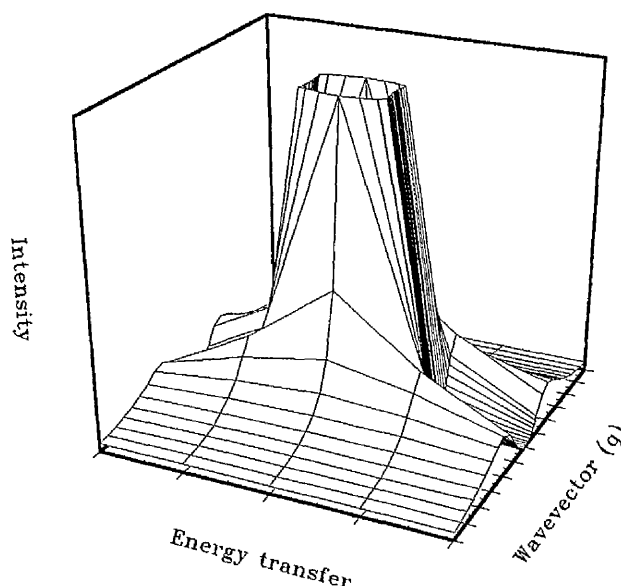


Figure 2.7. The structure of the q,ω scattering as defined by equation 2-1. The variables have been assigned arbitrary physical values. The 'fanning out' of the scattering in energy that is shown in **figure 2.6** by the dot-dash line can be seen starting here. The relative magnitude of the central scattering can be plainly seen justifying the approximations applied where the large q scattering is neglected.

For these data, where the resolutions are high and gradients of the scattering function are also high, the integration grid density in the 3-D simulation program was set at 25^3 . Where a large data set is being fitted the integral is performed a vast number of times. This is very demanding on computer resources, hence the **CRAY EL98** vector processor at Manchester Computing Centre was used along with carefully written vectorised code.

2.5.2 The Model.

One of the major problems in extracting valid critical exponents from such a neutron experiment is separating out the true critical scattering from the spin wave, and other, scattering. In the c-axis helimagnets there is a unique orientation where the critical scattering can be separated from the transverse scattering. This is of vital importance below the transition temperature. If the whole sample is above its transition temperature the longitudinal, (spin wave and anisotropy) and the radial (critical fluctuations) contributions to the scattering are indistinguishable and not divergent. Below the transition temperature the spin wave scattering diverges at the magnetic Bragg point whereas the critical scattering is non-divergent and broad. This is shown schematically in figure 2.8.

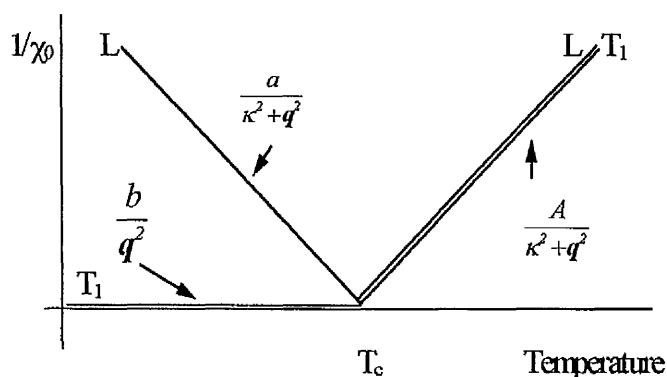


Figure 2.8 Showing the divergent and non-divergent parts of the scattering. These can be separated by applying the knowledge that $A=a+b$ for a given satellite. T_1 is transverse scattering and L is longitudinal.

The terms A, a and b in **figure 2.8** can be considered as simplified amplitudes of the respective scattering components. In reality the critical amplitudes, A and a , are given by multiples of $\chi\kappa^2$. (see the previous discussion of critical exponents). The other transverse term (referred to as T_{A2} and T_{B2} in **figure 2.9**) is cut off by the anisotropy, and is therefore almost q independent, so it is treated as a contribution to the incoherent background.

The amplitude b arises from the susceptibility term and is proportional to the magnetization divided by the spinwave stiffness. This composite factor is assumed to scale in the same way as A . We know that the exponent which scales these amplitudes, η , is very small, (η is defined by $\gamma = (2 - \eta)\nu$), typically 0.02 so near the critical temperature these two amplitudes are practically temperature independent.

A simple consideration of the physical spin arrangement in the basal plane (the spins are restricted to this plane by the crystal field, hence an x-y model can be used) gives the appropriate factors to be used in separating these components.

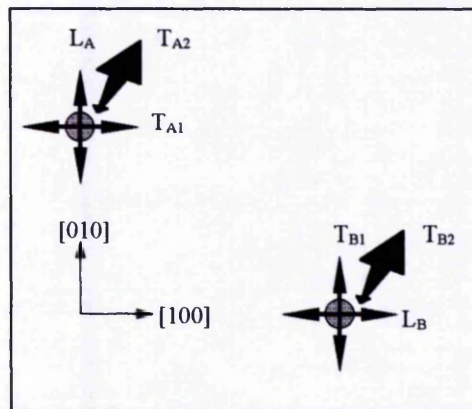


Figure 2.9 A sketch showing the three degrees of freedom allowed for a given spin subject to fluctuations in the basal plane, T and L refer to transverse and longitudinal fluctuations.

If a spin vector can be considered in the basal plane then its fluctuating component can, at any point, be broken down into three components orthogonal to each other, two transverse and one longitudinal component as shown in **figure 2.9**. by T_1 , T_2 and L_1 . Neutrons will only be affected by the components perpendicular to any given Q (see section 1.3). The scattering plane in which this experiment was performed was not the basal plane but chosen to be that described by the $[100]$ and the $[001]$ directions. Contributions to the magnetic scattering cross-section can therefore be algebraically separated into those which come from which fluctuating component. As an example let

us consider the primary contributions to a scan around the (100) position shown in **figure 2.3**. These would arise from a Q vector from the origin in reciprocal space to the point (100), it is therefore in the basal plane and the main perpendicular contributions would be (from **figure 2.9**): $T_{B1}+T_{B2}+L_A+T_{A2} = 2T_2+(T_1+L)$; and for a scan around the (002) position (the transverse scan shown in **figure 2.3**) the primary contributions would be, $T_{B1}+L_B+T_{A1}+L_A = 2(T_1+L)$. From this we can see that the critical scattering detected around the (002) position should be approximately twice the scattering around the (100) position and that the 'background' contribution from the out of plane anisotropy scattering is only present at the (100) position. The exact contributions are Q dependent. The scans performed are described in the next section but it can be seen that an expression which holds for general Q is only a matter of applying the correct geometric weighting factors. The exact form of the model used in our simulation was

$$S(q, \omega)_{\omega=0} = \exp\{-\alpha|q|^2\} \cdot \left[G_1 \left(\frac{A_{crit}}{\kappa^2 + |q|^2} \right) + G_2 \left(\frac{A_{div}}{|q|^2} \right) + A_{Bragg} \exp\left\{-\frac{1}{2} \frac{|q|^2}{\sigma^2}\right\} \right]$$

Equation 2-5

where the first exponential term models the magnetic form factor, the constants G_1 and G_2 are the geometric weighting factors discussed earlier, A_{crit} and A_{div} are the relative amplitudes of the divergent and critical scattering ($A_{crit} = \chi\kappa^2$, A_{div} assumed constant over the small temperature range we are concerned with). A finite value of A_{div} above the transition temperature is how we expect to be able to account for the issue of the resolution dependent central peak. This corresponds to defects (surface or otherwise) producing areas where the local ordering temperature is higher than the bulk. The final term models the magnetic Bragg scattering and so is only non-zero below the transition temperature.

2.5.3 Results.

A full fit of all the data from the three satellites resulted in a poor quality fit where no real significance could be assigned to the values of the fitted exponents. There are several

reasons for this. Firstly the crystal mosaic was shown to be structured, that is the crystal was made up of at least two crystallites. The extent of the structure could be seen in the elastic alignment scans. The misorientation between the two major crystals is small, $\approx 0.2^\circ$, and we originally hoped to consider this as mosaic spread in one large crystal. This has proved to be impossible with a one crystal model. Secondly, the temperature drift in the scans means that collecting data with a consistent symmetry in temperature about the transition temperature was impossible to achieve. 'Dead time' scans were incorporated to allow the temperature to stabilise between data sets. The temperature relaxation hysteresis at the transition temperature was carefully checked to enable accurate determination of the transition temperature, thus the appropriate time for temperature stabilisation was known. Even with these precautions, and fitting data with individual temperatures, it still could not be guaranteed that the sample itself was not subject to temperature lag. Thirdly, the sample was a large one and the high quality statistics needed to investigate the critical scattering meant that the intensity of the Bragg component of the scattering below the transition temperature was very large. A direct consequence of this was that the Bragg scattering suffered losses from its true intensity due to extinction. This was treated by a first order correction to the Bragg intensity of a fraction proportional to the predicted intensity being subtracted. The problem of temperature control resulted in a non symmetric distribution of points around T_N which is the area of crucial importance. The effect was not prohibitive but did result in a higher density of data at temperatures greater than T_N than less than T_N . The problem of structured mosaic has been attempted to be overcome with the inclusion of a twin crystal model where the model previously discussed is duplicated exactly but with a different zone centre which was calculated and fixed (relative to the magnetic zone centres of the main crystal) from the information held in the alignment scans. An overall scaling factor corresponding to the relative volume of the crystallite gave the appropriate weight. These two models are then summed to produce a full model $S(\mathbf{q}, \omega)$. This model increased the quality of fit for the $(000+\tau)$ satellite. χ^2 per degree of freedom for the

single crystal model was 26 whereas with the inclusion of the second crystal model this was reduced to 10, (see **table 2.3**). The radial scans performed during the experiment were fitted separately. The temperature dependence of τ was found to be small and consistent with the values measured by Thurston et al¹⁹. The effects of the crystallite and the temperature dependent effects associated with it far outweighed any advantage of incorporating a temperature dependent satellite position in the model. Unfortunately the duplication of the model to account for the second crystallite increased the computer time from a tolerable few half hours per iteration to a prohibitive several hours for a full data set. This means that the original intention to fit all the data together had to be revised and the individual satellites fitted on their own. The wider resolution scans were fitted with the one crystal model, the width of the resolution reducing the impact of the mosaic structure, whereas the high resolution small q peak was fitted with the two crystal model. The correction for extinction was crude and as such only applied to the two lower resolution data sets. In the high resolution satellite data the Bragg component was not fitted ($T < T_N$ data was ignored) removing the need to apply an inaccurate correction and, incidentally removing any possibility of measuring β , although this would already be too difficult to do accurately due to the problem of extinction. The accidental higher density of data at temperatures greater than T_N meant that even limiting the fitting procedure to this set a sufficiently large data set was being used. The results from these three individual fits are shown in **table 2.3**. Some sample scans along with the fitted data are shown in **figure 2.10**. All this data is from the $(000+\tau)$ satellite where the divergent term has been included.

Satellite	ν	η	$\gamma-(2-\eta)\nu$	χ^2
(100)	0.36(7)	0.032(5)	0.71	13.05
(002)	0.498(5)	0.039(3)	0.98	8.34
(000) without divergent term	0.85(8)	0.002(3)	1.70	13.8
(000) with divergent term	0.56(3)	0.014(8)	1.11	10.4

Table 2.3. Results of fits. The (100) and (002) data were full temperature data fitted with a single crystal model. The (000) data were $T > T_N$ data fitted to the twin crystal model. The quality of fit was improved with the addition of a divergent term

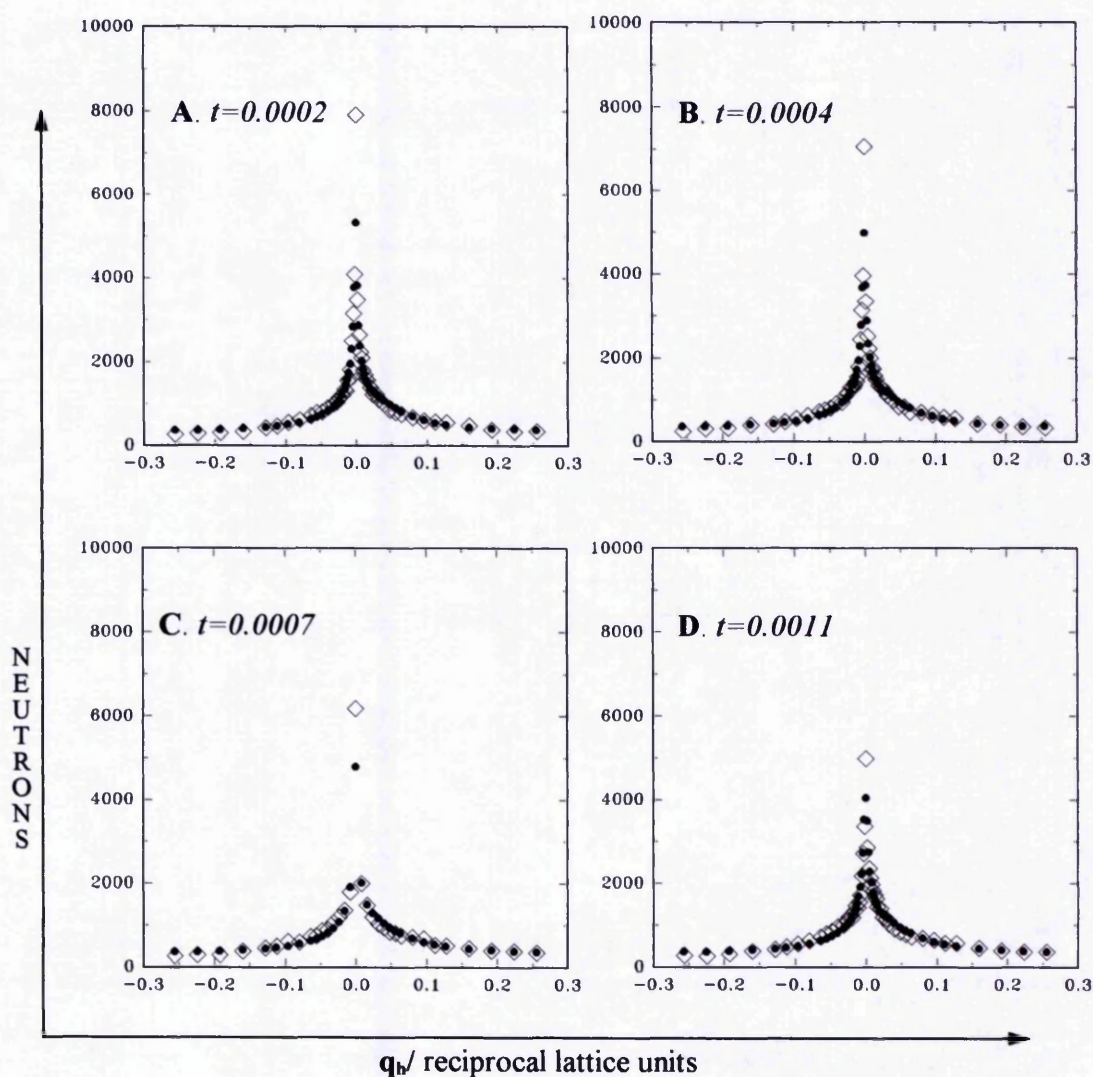


Figure 2.10. Samples of data from the (000+ τ) satellite shown as \diamond with the final fit shown as \bullet . It is clear that in the data taken at small reduced temperature that the model is lacking in intensity in the centre of the scans. All elastic data were taken with $|k_{\parallel}|=4.001\text{\AA}^{-1}$ and 30' Söller collimators throughout.

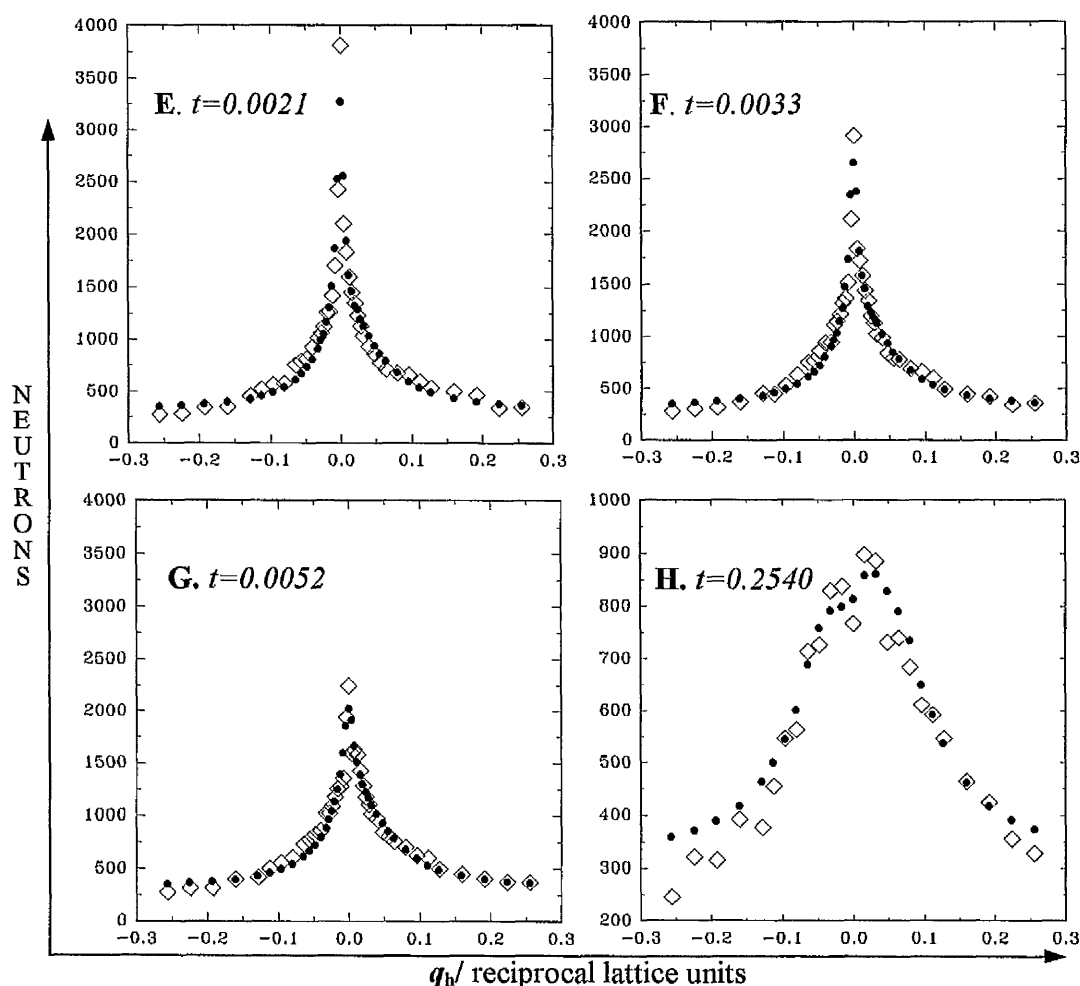


Figure 2.10 continued. Samples of data from the $(000+\tau)$ satellite shown as \diamond with the final fit shown as \bullet . It can be seen in E,F,G and H that the lack of intensity in the model is less pronounced at these larger reduced temperatures. Note: The y-axis is re-scaled from A,B,C and D. The scan shown in H clearly shows the mosaic structure and how the twin crystal model compensates for it. This is apparent here as the critical scattering is very broad at this large t hence more scattering from the second crystal is included within the resolution function appropriate for the scan performed.

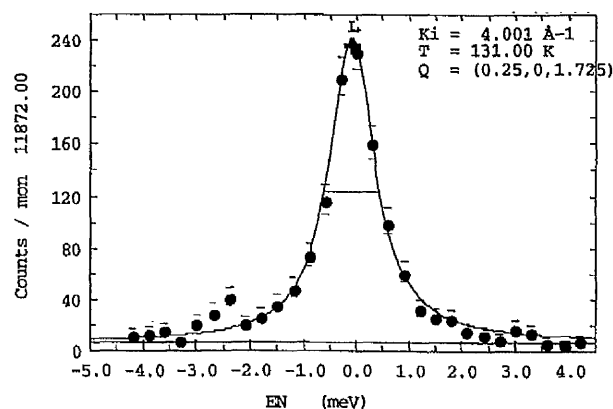


Figure 2.11. An inelastic scan taken in three-axis mode used to calculate the intrinsic energy width. The width was found to be 4.28 THz (1.03 meV). Collimation before the analyser was $60'$ all other was $30'$.

2.6 Discussion and Conclusions.

The lack of a single crystal sample means that this data set is ultimately limited in its use. The difficulties raised in this experiment display clearly why the helimagnets are still a subject of experimental study. It is plain that the analysis of this data could be refined considerably with the extension of the twin crystal model to the whole data set. Although the mosaic indicates two principal crystals which make up the whole sample it is probable that more smaller crystallites are also contained within the bulk, frustrating our attempts to fully map the mosaic structure. The lack of a single crystal is not the only limiting complication with these data. The addition of variables is not desirable. The problems encountered with temperature drift were a major issue. The temperature control used was not optimal for this experiment. To enable many orders of magnitude in reduced temperature to be covered with confidence platinum resistance thermometry combined with the appropriate control systems are desirable. These systems enable stability's of 0.01K to be achieved routinely. This was not available for this experiment. A further question which is raised is that of energy integration and whether it was complete. Due to a restricted beam time allocation it was not possible to perform the range of inelastic scans required to answer this question. The approximations made in terms of the data analysis was that the fourth dimension of the hyperellipsoid resolution function could be considered as a limitless column in q, ω space. If, after the expansion of the twin crystal model there is reason to bring the energy integration into question then this approximation could be refined and the data fitted to a discretely integrated energy dependent function. The basis for such a modified fit has been laid out in the series of simulation programs written to test the validity of the resolution approximations used. These are discussed in section 2.5.1. The description of the central peak by resolution limited divergent scattering appears to be reasonable although the quality of fit is not as good as was hoped. The model shows a clear lack of central weight at small reduced temperatures although this still could be due to the imperfect mosaic description.

It is appropriate here to make some general comments about the overall approach taken to this experiment. In our analysis of these data a global approach was taken where the intention was that *all* the raw data was to be fitted in one process with a single model. While such an approach is undoubtedly elegant the sheer magnitude of the task uncovered a new set of problems associated with the interpretation of such large data sets. Using the methods attempted here requires extreme caution and rigor. The raw data set is large and complex even by neutron scattering standards. The problem arose during analysis of being unable to see easily and quickly how the fits were evolving. This was highlighted with the introduction of the twin crystal model where the subtle effects at small reduced temperatures become large at larger reduced temperatures (see **figure 2.8**), an initially non-intuitive conclusion. It is vital to maintain an objective view of the model during the fitting procedure. These problems have meant that for these data the global approach was not used. The development of much more sophisticated data visualisation and interpretation software is necessary to make this 'whole model' type approach to the analysis of such large data sets on reasonable time scales viable.

The results obtained for the high resolution satellite (see **table 2.3**) show some consistency with the results obtained by Thurston et al¹⁹. Where Thurston's group deliberately fitted the central peak as critical scattering the values of γ and ν are high (see **table 2.1**). This is reflected in our results where the data was fitted without the central peak contribution. $\gamma=1.7(2)$, $\nu=0.85(8)$ compared to Thurston's $\gamma=2.5$, $\nu=1.0(3)$ this indicates that the fit was absorbing the central peak scattering into the critical scattering model artificially elevating the exponents in value. The fitted values being an approximate weighted mean of the two sets of values published by Thurston. The exponents obtained when the central peak was included separately are consistent to within error of previously published values, $\gamma=1.11(6)$, $\nu=0.56(3)$ compared to Thurston's $\gamma=1.24(15)$, $\nu=0.54(4)$ and those published by Gaulin et al¹⁸, $\gamma=1.14(10)$, $\nu=0.57(4)$.

In conclusion I consider the values of the critical exponents extracted from the $(000+\tau)$ data set to be a reliable indication that the transition is in the chiral, tri-critical mean field range of predicted critical exponents rather than that predicted by Barak⁷ or Guillou¹¹ (see **table 2.1**). This is consistent with previously published results where the central peak was modelled as a Lorentzian squared profile feature. The modelling of the central peak by assuming a defect driven persistence of order beyond the transition temperature has some merit although it is impossible from the analysis so far to be anything other than cautious about this. The analysis of this data is ongoing.

2.7 References.

- ¹ Taylor. K.N.R. "Physics of Rare Earth Solids" Chapman and Hall (1972)
- ² Jensen J. and Mackintosh A.R. "Rare Earth Magnetism" Oxford Science Publications. Clarendon Press. (1991)
- ³ Brézin E. Phys. Rev. B. **12** pp4945 (1975)
- ⁴ McMorow D.F., Patterson C., Godfrin H. and Jehan D.A., Europhys. Lett. **15** pp541 (1991)
- ⁵ Cowley R.A., Jehan D.A., McMorow D.F. and McIntyre G.J., Phys. Rev. Lett. **66** pp1521 (1991)
- ⁶ Bak P. and Mukamel D., Phys. Rev. B **13** pp5086 (1976).
- ⁷ Barak Z. and Walker M.B., Phys. Rev. B **25** pp1969 (1982)
- ⁸ Tindall D. A., Steinitz M.O. and Plumer M.L., J. Phys. F. **7** L263 (1977).
- ⁹ Kawamura H., L. Appl. Phys. **63** pp3086 (1988).
- ¹⁰ Azaria P., Delamotte B. and Jolicoeur J., Phys. Rev. Lett **64** pp3175 (1990)
- ¹¹ J.C.Le Guillou. Private Communication to Azaria.P., Delamotte.B. and Jolicoeur.T. Phys.Rev.Lett **64** pp3175 (1990)
- ¹² Azaria.P., Delamotte.B. and Jolicoeur.T. Phys.Rev.Lett **64** pp3175 (1990)
- ¹³ Dietrich O.W. and Als-Nielsen J., Phys. Rev. **162** pp315 (1967)
- ¹⁴ Eckert J. and Shirane G., Solid State Comm. **19** pp911 (1976)
- ¹⁵ Thurston T.R., Helgesen G., Hill J.P., Doon Gibbs., Gaulin B.D. and Shirane G. B.D, Physica B. **192** pp177 (1993) and Thurston T.R. et al., Phys. Rev. Lett **70** 3151 (1993)
- ¹⁶ Jayasuriya K.D., Campbell S.J. and Stewart A.M., J.Phys.F **14** pp1725 (1984)
- ¹⁷ Jayasuriya K.D., Campbell S.J. and Stewart A.M., J.Phys.F **15** pp225 (1985)
- ¹⁸ Gaulin.B.D., Hagen.M. and Child.H.R., Journal de Physique. C8 **49** pp327 (1988)

¹⁹ Thurston T.R., Hill J.P., Doon Gibbs., Gaulin B.D. and Simpson P.J., Phys.Rev.B **49** pp15730 (1994)

²⁰ Malmstrom G., and Geldart D.J.W., Phys.Rev.B. **21** pp1133 (1980)

²¹ Lederman F.L. and Salomon M.B., Solid State Commun. **15**, pp1373 (1974)

²² Jayasuriya K.D., Campbell S.J. and Stewart A.M., Phys.Rev. B **31** pp6032 (1985)

²³ Instrument details. <http://www.ill.fr> (1997)

²⁴ Lloyd R.G., Ph.D. Thesis, University of Manchester. (1989).

Chapter 3. Spin Dynamics in the Dilute Ising Magnet $\text{Mn}_{1-x}\text{Zn}_x\text{F}_2$.

3.1 Introduction.

In the previous chapter the discussion of phase transitions was restricted to static critical phenomena which can be described in terms of single time spin correlation functions. In this chapter we are to consider the effects of dynamic phenomena. In a continuous phase transition the response time of the system tends asymptotically to infinity as the transition is approached. It is the dynamic processes which determine the behavior of such quantities as relaxation rates, transport coefficients and response times. The relaxation processes are governed by the specific dynamics of a system although dynamic universality classes have been assigned. Important factors in the relaxation to equilibrium process may include geometric disorder, frustration and the interplay between the two. Clarification of the roles of these factors is an important aim in the study of the dynamics of random magnetic systems.

$\text{Mn}_{1-x}\text{Zn}_x\text{F}_2$ is a disordered system. When $x=0$, i.e. 'pure' MnF_2 , the system orders antiferromagnetically with the manganese ions forming a body centred tetragonal unit cell. In total there are six atoms in the full chemical unit cell arranged as shown in **figure 3.1**. In the alloy, zinc is added in such a way as to produce a dilute system. In such a system a fraction of the magnetic ions are replaced by chemically similar ions with radically different magnetic properties. This can be achieved in such a way that the distribution of the replacement ions throughout the system is random. Under such conditions the system becomes magnetically frustrated. Zinc ions being of a similar size to manganese can occupy the body centered crystal sites of manganese shown in **figure 3.1** and the magnetic symmetry is spoilt. One

effect of this is to suppress the transition temperature of the system. This can be understood in a simple mean field context as $J(q_0)$, the sum over the magnetic ion-ion interactions, is reduced. The phase diagram of a dilute system is shown schematically in **figure 3.2**. The dotted line shows the transition temperature of the pure system, (67K in MnF_2). As the dilution concentration is increased from zero, the transition temperature is suppressed. The area in this phase diagram between the transition temperature of the pure system (67K, the dotted line in **figure 3.2**, known as the Griffiths temperature, T_G , in the dilute system) and the transition temperature of the dilute system, T_C , is known as the Griffiths phase, a term first coined by Randeria et al³.

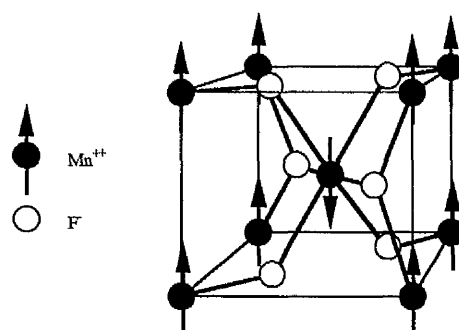


Figure 3.1. Structure of 'pure' MnF_2 . The antiferromagnetic spin orientation is shown by the arrows on the Manganese ions.

Above a certain level of dilution known as the percolation threshold, x_p , there ceases to be an ordered magnetic phase, long range order is destroyed and the system breaks up into a series of isolated uncorrelated clusters. In the area labelled the Griffiths phase the bulk of the system is not ordered but there are clusters of order within the sample where the dilution from the randomly introduced Zn ions is lower than average due to statistical fluctuations. These areas are statistically unlikely but are of great importance in determining the dynamics of the system. The effects of these areas was originally thought to be too subtle to be measurable as a direct consequence of their statistical improbability. In the wake of earlier work by the Manchester group¹ we now know that measurement of these effects can be achieved. Lloyd and Mitchell's work¹ was the first direct observation of the non-exponential relaxation at long times, the signature of the Griffiths phase. These measurements were made in a dilute

Heisenberg antiferromagnet. It is worth noting that the theoretical existence of such a relaxation has never been in doubt and that the theories all agree that non-exponential relaxation should be present. The predicted effects are subtle, and require well-defined experiments to observe and characterize them in detail. The Manchester group's¹ previous experiment successfully identified the existence of a Griffiths phase signature but was unable to show its form. It is the aim of the work laid out in this chapter to carry forward Lloyd and Mitchell's¹ early work to provide some direct quantitative information about the form of the non-exponential relaxation in the asymptotic regime ($t \rightarrow \infty$).

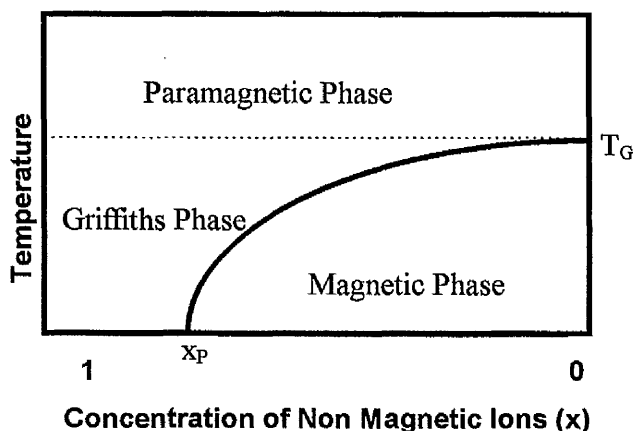


Figure 3.2. A schematic phase diagram showing the Griffiths phase. T_G is the Griffiths temperature, x_p is the percolation threshold below which there is no ordered magnetic phase.

3.2 Theory, Background and Motivation.

Theoretical descriptions of the dynamics of disordered magnetic systems in the paramagnetic phase often display non-exponential relaxation. These relaxation's are analogous to the stretched exponential Kohlraush law, $C(t) \propto \exp\{-At^\beta\}$, for glassy systems¹². Theoretical work on the dynamics of dilute Ising ferromagnets², based on the concept of isolated rigid clusters of order, was extended to Ising spin glasses³ and later developed further for disordered magnets in general^{4,5,6,7,8,9}. All predict non-exponential forms for the long time limit of the dynamics above the ordering temperature of the pure system. There is predicted to be a qualitative difference, depending on whether the system is above or below the Griffiths temperature. Non-exponential decay of the spin correlation function in the asymptotic limit $t \rightarrow \infty$ reflects the presence of free-energy singularities. In the disordered system above the bulk ordering temperature statistical fluctuations produce small regions with higher than average concentration which are below their local ordering temperature. The slow relaxation of these rare regions of order gives rise to the non-exponential term, characterised by a long time tail in the correlation function.

The predictions for the existence of the long time tail are not in dispute theoretically although there is dispute about the appropriate time regime for these effects. The precise nature of the theoretically predicted form of decay at long times depends on the number of degrees of freedom of the magnetic moments in the system. In the next few pages I will give a basic account of the theoretical results, the approach that lead to them and introduce some more formal definitions relating to dilute systems.

The theoretical approach adopted by Bray⁴, whose early work still governs any discussion of dynamics in the Griffiths phase, concentrates on the dominance of the long-time dynamics of the previously mentioned clusters of spins which are ordered. In

general the Griffiths temperature can be defined to be “the highest possible transition temperature allowed in principle by a rare statistical fluctuation in the spins over the whole system”¹⁰. Non-exponential decay in the correlation function, $C(t)$, at long times is indicative of the Griffiths phase. At the Griffiths temperature there is a cross-over between exponential and non-exponential relaxation. The non-exponential decay arises due to a finite contribution to the correlation function from statistically rare, quasi-ordered regions of the system whose relaxation is only limited by finite-size effects.

The predictions of Bray⁵ can be outlined as follows; at and above T_G the asymptotic form, ($t \rightarrow \infty$), of the spin correlation function, $C(t) = [\langle S_i(t)S_i(0) \rangle]$, for small $|T - T_G|/T_G$ is

$$C(t) \sim \exp\left\{-t^{d/(d+z_p)} f(t/\xi^{d+z_p})\right\}$$

Equation 3-1

where d is the dimensionality of the spins, and z_p is the dynamic critical exponent of the pure system. $f(x)$ is a scaling function where ξ is the correlation length of the pure system. This is different to the previously standard result which involves the exponent z not $d+z_p$.

- For large t/ξ^{d+z_p} i.e. $\gg 1$, above T_G and out of the critical region for the pure system we have,

$$C(t) \sim \exp\left\{-c\xi_p^d\right\} \exp\left\{-t/\xi_p^{z_p}\right\}$$

Equation 3-2

- For Small t/ξ^{d+z_p} , i.e. $\ll 1$, this is the case in the vicinity of T_G we have,

$$C(t) \sim \exp\left\{-t^{d/(d+z_p)}\right\}$$

Equation 3-3

- For a Heisenberg system below T_G , (the parameter B vanishes as $T \rightarrow T_C$, $B \sim (T - T_C)^{\alpha+z\nu}$, α , z and ν are the usual critical exponents of the random system).

$$C(t) \sim \exp\left\{-(Bt)^{1/2}\right\}$$

Equation 3-4

- For Ising systems below T_G an even slower relaxation is predicted (where amplitude A diverges as T_G is approached from below).

$$C(t) \sim \exp\left\{-A(\ln t)^{d/(d-1)}\right\}$$

Equation 3-5

There have been other approaches to the problem of spin dynamics in dilute magnets. Most of these have been based on considering the percolation threshold (where $T_C=0$). This allows a low temperature approach to be used. Using this regime it has been shown that a stretched exponential relaxation can be derived by applying a power law distribution of barriers to relaxation and cluster sizes¹¹. This produces a Kohlrausch¹² like form with a temperature dependent parameter β . These methods calculated at the percolation threshold explicitly neglect the influence of the rare quasi-ordered clusters central to Bray's approach and as such can be considered to be reflecting some pre-asymptotic regime. More recently, Nusser¹³ has analysed the problem and shown the relationship with the Lifshitz band tails. The problem is still a live subject theoretically, Monte Carlo techniques have provided the means to model the phenomena. The Ising system has been the subject of many such investigations, below the percolation threshold^{14,15,16,17,18} where results were consistent with the above pre-asymptotic regime and above the percolation threshold where results have been conflicting. Komori et al.¹⁹ observed effects consistent with the relaxation of rare clusters of spins while Grassberger²⁰ has not. All these simulations have used the early work of Bray as the

benchmark and hence it is Bray's early model for the asymptotic relaxation that will be the focus of this work.

Considering the model proposed by Bray several questions are raised. First, at what point are we in the long time limit? The theory is not correct for short times thus the cross-over point is to be determined for any given system. This has particular implications for an experiment which will be discussed later. Second, how applicable is this theory to real systems? Whether the details of a system's dynamics affect the validity of the theory is at this stage unknown. Bray assumed model A relaxation dynamics²¹ with no conservation laws (below T_G). In this model spins are assumed to be in thermal equilibrium with a bath which introduces a random spin flip excitations where the flipping probability is constant per unit time. These results were used to model, with reasonable success, a Heisenberg system which would normally be considered as having a conserved order parameter. Finally, how large is the effect? We expect that it is small but we do not know the amplitude dependence on temperature. It can be assumed that the effect is zero above T_G and increases as T_G is approached from above. We also know that amplitude A in equation 3-5 is divergent as T approaches T_G from below. Beyond this a direct measurement is required.

The unanimous agreement on the existence of a non-exponential long-time tail has, as we have seen, maintained a high level of theoretical interest in the area. It is however difficult to find experimental characterisation of these effects in the literature. A previous experiment by this group studied the mixed Heisenberg antiferromagnet $\text{KMn}_x\text{Ni}_{1-x}\text{F}_3$ using neutron inelastic scattering¹. This experiment successfully identified the Griffiths phase signature of a long time tail along with a well described pre-asymptotic regime. Since then effects seen in muon-spin-relaxation and Mößbauer experiments²² have been attributed to spin-cluster effects in the Griffiths phase. The Duisberg group have performed a series of susceptibility measurements on uniaxial antiferromagnets^{23,24,25},

using SQUID magnetometry, which have also given experimental evidence of the Griffiths dynamics and followed these up with a quasielastic neutron scattering study of the magnetic field induced Griffiths phase in FeCl_2 ²⁶. They observed the Griffiths signature as a discontinuous change in slope of the integrated scattering intensity as a function of temperature. This is more direct than the SQUID magnetometry measurements although it is still not as direct an observation of the relaxation processes that can be achieved using neutron inelastic scattering.

The direct observations of the Manchester group on a mixed Heisenberg system has shown the validity of the experimental process we are to use. The Heisenberg system is not necessarily described well by model A dynamics (the model assumed by Bray). The exact form of the non-exponential term is almost certainly dependent on the dynamics specific to the system. It is advantageous therefore to choose a system which matches as closely as possible the model used by Bray. In this way we can expect to reveal quantitative rather than only qualitative information about the form of the relaxation. Ising systems are known to be well described by model A dynamics giving more reason to expect the form of the non-exponential term to reflect Bray's predictions, which incidentally, predict an even longer time tail for the Ising case than for the Heisenberg case. The dilute Ising antiferromagnet $\text{Mn}_{1-x}\text{Zn}_x\text{F}_2$ was chosen as it closely obeys model A type dynamics and, in the context of the random field problem, has been well characterised as a system²⁷

3.3 Instrumentation and Method.

Measuring directly the correlation function experimentally is not trivial. The most direct method would be the neutron spin echo technique which measures the “intermediate scattering law” $S(\mathbf{q}, t)$. Although this technique has been applied successfully to study magnetic dynamics the expected weak nature of the signal at long times meant that in practice the Griffiths signature would be very difficult to observe. Experiments outlined in the previous section have used measurement of the magnetic susceptibility and quasielastic neutron scattering to successfully access the Griffiths signature. Susceptibility measurements do not provide as direct a measurement of the correlation function as neutron scattering and as such are not as convincing. The quasielastic neutron scattering experiment was concerned with measuring the effect of the Griffiths singularities on the integrated scattering intensity, which is, in essence, a magnetisation measurement. More strictly, it measures a quantity related to the antiferromagnetic order parameter fluctuations. Inelastic neutron scattering was therefore chosen as the means of investigating a dilute Ising system. Inelastic neutron scattering measures directly the scattering function, $S(\mathbf{q}, \omega)$. If the quantity we wish to measure is \mathbf{q} independent then the scattering function becomes only a function of energy, a power spectrum. Using fast Fourier transform techniques (the details of which will be discussed later) a model defined in the time domain (the correlation function) can be fitted to the scattering function (power spectrum). The long time information is contained at high enough resolution within the line shape at small energies of the power spectrum. This provides a direct observation of the relaxation.

For the purposes of this experiment three crystals were grown by the crystal growth unit at the Clarendon Laboratory, Oxford. The specifications were for $\text{Mn}_{1-x}\text{Zn}_x\text{F}_2$ where $x=0.05, 0.35$ and 0.60 . The $x=0.05$ and $x=0.35$ crystals were of high quality with no visible cracking. Both boules were approximately 5cm long and 1cm in diameter and

oriented such that the c^* axis was parallel to the length of the boules. The $x=0.60$ crystal was of very low physical quality with fragmentation and cracking in all areas. This sample was not used in this experiment.

3.3.1 The Triple Axis Spectrometer IN12.

IN12 is situated at the end of a long beam guide in the main experimental hall at the Institut Laue Langevin (ILL) high flux reactor neutron source. The main features of the spectrometer are similar to IN8 (discussed in section 2.4.1). A diagram of the instrument is shown in **figure 3.3**.

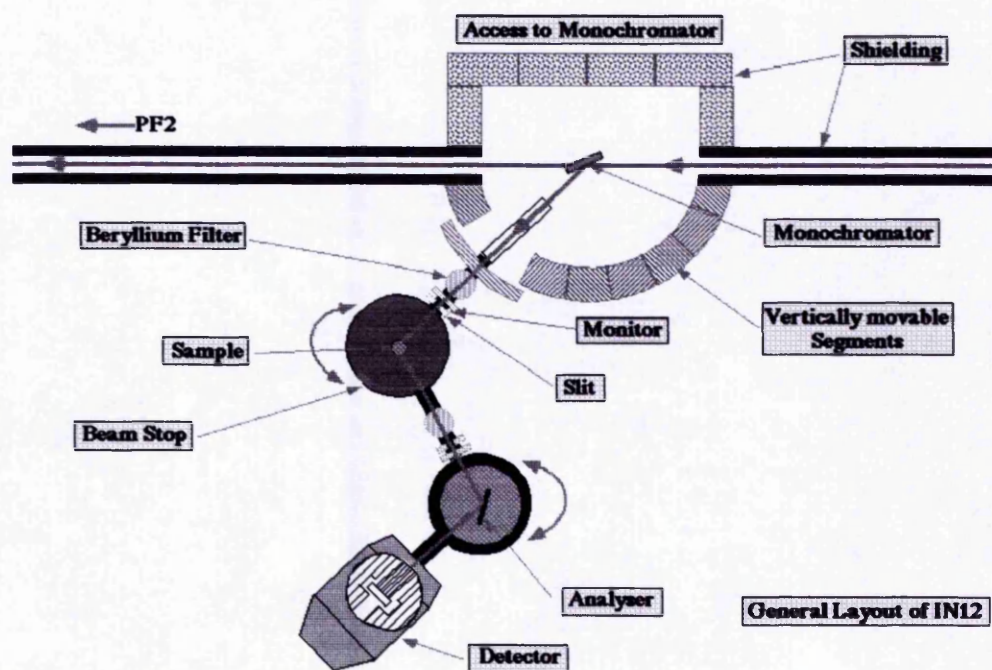


Figure 3.3. A diagram showing the layout of the triple axis spectrometer IN12²⁸. The direction and path of the neutrons is shown arriving from the shielded beam line. The monochromator selects out neutrons contained in the guide directed from the ILL reactor.

The instrument has the three scattering elements common to all triple axis machines, namely the monochromator, sample and analyser. On IN12 (unlike IN8) the position of the monochromator rotation axis is fixed, which requires a semi-circular array of shielding blocks one of which is raised to allow the neutron beam passage and the others

are lowered to provide shielding. The monochromator itself is a set of vertically focusing pyrolytic graphite crystals using the (002) reflection. The instrument is 108m from the reactor source. The beam size is $12 \times 3 \text{ cm}^2$. The neutron guide has double curvature which provides a filter for $\lambda/2$ contamination at all wavelengths shorter than 4\AA . For longer wavelengths a nitrogen cooled 10cm long beryllium filter can be mounted on the instrument after the primary spectrometer and before the monitor (shown in **figure 3.3**). This enables secondary scattering from the monochromator at $\lambda > 4\text{\AA}$ to be filtered out of the beam incident on the sample. Gadolinium-coated Söller collimators with divergences of $10'$, $20'$, $30'$, $40'$, $50'$ and $60'$ are available and any combination can be placed before the sample, the analyser and the detector. The detector is a vertically mounted 12cm high, 5cm diameter ^3He gas detector. Other than for initial alignment of the crystals the instrument was used in constant- Q triple-axis mode throughout the experiment.

3.3.2 Collection of Data.

The samples were aligned with the $[010][100]$ plane as the scattering plane. The (100) and the (010) are purely magnetic Bragg points being systematic structural absences. In the alignment process the beryllium filter was removed so that $\lambda/2$ scattering from the structural (002) and (200) was present at the (010) and (100) sites. These peaks were used for alignment above T_C . The a lattice parameter was measured to be 4.81\AA in the $x=0.35$ sample and 4.86\AA in the $x=0.05$ sample, to be compared with 4.87\AA in pure MnF_2 .

The temperature of the magnetic phase transition was located initially by an estimate calculated by linear interpolation from previous measurements of the transition temperature in $\text{Mn}_{1-x}\text{Zn}_x\text{F}_2$, $x=0.25$ (46K) and $x=0.50$ (21K)²⁷. Using the nominal dilution level given by the Clarendon laboratory crystal growth unit an approximate transition temperature was calculated. A series of scans in temperature enabled the actual transition

temperature to be located (see **figure 3.4**) at 40.00(4)K for $x=0.35$ and 64.3(1)K for $x=0.05$.

The bulk of the data collected during this experiment was taken at a constant Q of (1.04 0 0), which was chosen for two reasons. Although the (100) is a purely magnetic Bragg reflection there may be some small residual order contamination, giving rise to a small nuclear Bragg component, the addition of an elastic contribution superimposed on top of the dynamic information is not desirable. The second point is that although we can assume that the non-exponential component of relaxation is not strongly Q -dependent the intensity is scaled by the critical scattering (the principal exponential relaxation process) which is q dependent and is a maximum at the magnetic zone centre.

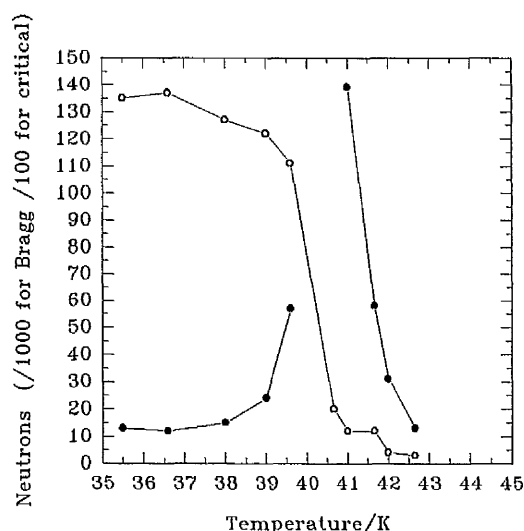


Figure 3.4. Shows a graph illustrating the level of scattering at the point $Q_h=1.00$ (mainly Bragg scattering, filled circles) and $Q_h=1.02$ (mainly critical scattering, hollow circles) for the $x=0.35$ sample. This clearly shows the transition in the $x=0.35$ crystal.

These two contradictory desires for optimising the measurement lead to the compromise of (1.04,0,0). The elastic resolution width was smallest in the radial direction and hence a point well away from Bragg scattering still with considerable critical scattering amplitude was chosen.

For the first crystal, $x=0.35$, inelastic scans were performed under three energy resolutions. Firstly a resolution of 0.113THz full width at half the maximum amplitude (FWHM) later referred to as low resolution data. This was achieved with an incident wavevector, $|k_i|$, of 2.10\AA^{-1} and three Söller collimators each with $60'$ divergence. With this resolution set up an energy width of $\pm 0.5\text{THz}$ was required to reach background in a 44K inelastic scan. A series of five inelastic scans at $T=295\text{K}$, 70K, 64K, 54K and 44K were made each with 51 evenly spaced points spanning -0.5THz to $+0.5\text{THz}$. Secondly, a resolution of 0.011THz FWHM using $|k_i|=1.110\text{\AA}^{-1}$ and collimation of $60'$ in each of the three collimation positions was used (these data will later be called medium resolution data). These data have an energy range of $\pm 0.1\text{THz}$ (51 points per scan), this limit was imposed by physical restraints of the spectrometer (when this incident wavevector is used) but was sufficient as the high energy transfer information is contained within the low resolution data. Data were taken at the same temperatures as the low resolution data sets. Finally a resolution of 0.0045 THz FWHM (high resolution). This resolution required a $|k_i|$ of 1.05\AA^{-1} and collimator divergence's of $10'$ throughout the spectrometer. Again the physical restraints of the spectrometer limited the energy width of the scans but again it was sufficient to select the central information, 15 point scans with an energy width of $\pm 0.007\text{THz}$ were undertaken at 295K, 70K and 44K. The reduced range of temperatures was due to the restricted beam-time allocation. The narrower the resolution width and the lower the incident wavevector the fewer neutrons are incident on the sample. Less still are detected hence the high resolution data took considerably longer to collect even though statistically it is of lower quality.

There was time to have only a preliminary look at the second crystal. A single resolution set up was used (that corresponding to medium resolution for the previous sample). Scans of energy width 0.1THz and temperatures 293K, 70K, 66.3K, 65.6K and 64.9K ($T_c=64.3\text{K}$) were performed at $(1.04\ 0\ 0)$, each scan having 51 points.

3.4 Data Analysis and Results.

3.4.1 The Fast Fourier Transform and Fitting Program.

The type of neutron scattering experiment that we have performed gives a direct measure of the scattering function $S(\mathbf{q}, \omega)$ which is a Fourier transform of the two point correlation function $C(\mathbf{r} - \mathbf{r}', t - t') = \langle \sigma(\mathbf{r}, t) \sigma(\mathbf{r}', t') \rangle$ where the spin component $\{\sigma(\mathbf{r}, t)\}$ may be the value of a Cartesian component of the spin at \mathbf{r} , or the scattering length density (for elastic scattering). Many theoretical approaches to condensed matter problems lead naturally to a correlation function defined in the wavevector energy (\mathbf{q}, ω) system making the comparison of theory and experiment straightforward. In this case however, theory has led to a correlation function defined in time. This is due to the nature of disordered systems where the averaging procedures used to calculate these correlation functions in Fourier space, in pure systems, may reduce the impact of effects of crucial importance due to statistically unlikely regions in real space in the disordered system. Ultimately once the correlation function has been calculated the model must maintain its integrity through the Fourier transform and the two representations must be equivalent.

As the natural space for the theory governing this work is real space and time, (\mathbf{r}, t) , the data from this experiment were fitted to a model defined in the time regime using a fitting program originally developed by Lloyd²⁹ and subsequently adapted by the author called FTFIT. The approach of this program is to calculate a numerical model of $C(t)$ and then compare its Fourier transform to the measured data. $C(t)$ is known to be real and even, so, expressing the usual Fourier integral as a sum:

$$F(\omega_n) = \Delta t \sum_{k=0}^{N-1} C(t_k) \exp\{i\omega_n t_k\}$$

Equation 3-6

Where $t_k = k\Delta t$, $k=0, 1, \dots, N-1$ and $\omega_n = 2\pi n/N\Delta t$, $n=-N/2, \dots, N/2$. The values of N and Δt determine the CPU time required by the program and the precision of the results. Applying Nyquist's theorem which states that if a function is band-width limited to frequencies within $\pm\omega$ then it may be completely specified by a sample taken at time intervals Δt where $\Delta t = \pi/\omega$, the reverse is also true. As the function we are describing tends to zero at long times we can choose a maximum time t_{\max} such that $R(t_{\max}) \approx 0$, (<the smallest real number on the computer). t_{\max} is determined by the precision with which the energy was measured, in this case $t_{\max} = 2\pi/\delta\omega$, $R(t_{\max})$ is then checked to be zero. N was chosen to be 8192 (2^{13}), powers of two are required by the transform routines, which was sufficient to avoid aliasing in all the data sets. Aliasing occurs when any weight in the Fourier transform which lies outside the frequency range $\pm\omega_{\max}$ is folded back in by the transform routine, this can be avoided by checking that $F(\omega_{\max}) \approx 0$. The discrete transform, equation 3-6, is performed by library subroutines REALFT and FOUR1 documented in Numerical Recipes³⁰.

The fitting routine applies the Levenberg-Marquardt method to maximise the Poisson probability function given in equation 2-4. This procedure varies smoothly between the inverse Hessian method and the steepest descent method. The latter being used far from the maximum in Poisson probability space and switching smoothly to the former close to the maximum. The code was adapted for data subject to Poisson statistics by Lloyd²⁹ and updated by the author. The code is based on subroutine MRQMIN from numerical recipes³⁰.

The information about the correlation function held in a single data set decreases as time increases since the resolution function in the frequency domain is a Gaussian envelope,

(this is discussed in detail in section 3.4.2). The implication being that any error on a fitted model increases with time. This provides us with a dilemma, we do not have a truly model independent fitting process. This can be overcome for the most part by taking data under a variety of resolution conditions. As has been mentioned previously three different sets of resolution conditions were used during this experiment. This was to enable the full frequency range to be covered with weight given to a different time range in each resolution enabling different model parameters to dominate in each resolution and be fixed where their influence is least. In this way a more model independent picture can be built up with realistic errors on each fitted parameter. The effects on the fitting process and final parameters will be discussed later.

3.4.2 Resolution and Bose Factor Corrections.

The resolution correction is performed in two parts, the resolution volume corrections and the $|k_f|/|k_i|$ factor in equation 1.9 are calculated and applied in phase space, (q, ω) space, and the resolution function convolution is performed in the time domain.

There are two resolution volume components. From Dorner³¹ we have:

$$\int_{-\infty}^{\infty} d^3q d\omega R(q - q_0, \omega - \omega_0) = V_I V_F$$

Equation 3-7

where $R(q, \omega)$ is the resolution function and V_I and V_F are the resolution volumes of the primary and secondary spectrometer respectively. The correction for V_I can be removed from the data by normalising by the monitor counts (providing the monitor is placed after the monochromator and filter but before the sample). V_F can be calculated from:

$$V_F = k_F^3 \cot \theta_A (2\pi)^{3/2} \cdot \frac{\beta_2 \beta_3}{\sqrt{4 \sin \theta_A \eta_A^2 + \beta_2^2 + \beta_3^2}} \cdot \frac{\eta_A \alpha_2 \alpha_3}{\sqrt{\alpha_2^2 + \alpha_3^2 + 4\eta_A^2}}$$

Equation 3-8

Where θ_A is the scattering angle at the analyser. The α s and β s are the horizontal and vertical collimation divergences before and after the analyser and η_A is the mosaic of the analyser, all of which are either machine parameters or can be calculated directly from machine parameters. From the extensive work of Cooper and Nathans³² we define the resolution function as:

$$R(\mathbf{x}) = \left(I_0 \frac{V_F}{4\pi^2} \sqrt{\det \mathbf{M}} \right) \cdot \exp \left\{ -\frac{I}{2} \mathbf{x} \cdot \mathbf{M} \cdot \mathbf{x} \right\}$$

Equation 3-9

Where \mathbf{M} is a symmetric matrix whose elements are given by Cooper and Nathans in terms of the instrumental parameters, $\mathbf{x} = (q_x, q_y, q_z, \omega)$ and I_0 is a constant containing factors arising from attenuation due to the cryostat, detector efficiencies etc.

We can now describe the scattering function as two factors, the wavevector dependent susceptibility and the normalised spectral weight function (as described in chapter 1). If the approximation that the wavevector dependent susceptibility is slowly varying over the range of \mathbf{q} spanned by the resolution function we can perform the integrals over \mathbf{q} analytically. The scattering function can then be expressed as an integral over time with a correlation function defined in the time domain, this gives:

$$S(\mathbf{q}, \omega) = \frac{2I_0 V_F \chi_{\mathbf{q}}}{\sqrt{2\pi} \sqrt{M_{44}^{-1}}} \beta \omega (n(\omega) + 1) \int_0^{\infty} dt C(t) R(t) \exp\{-i\omega t\}$$

Equation 3-10

Where

$$\begin{aligned} R(t) &= \int_{-\infty}^{+\infty} d\omega \exp \left\{ -\frac{I}{2} \frac{\omega}{M_{44}^{-1}} \right\} \exp\{-i\omega t\} \\ &= \sqrt{2\pi} \sqrt{M_{44}^{-1}} \exp\{-t^2 M_{44}^{-1}\} \end{aligned}$$

Equation 3-11

and $(n(\omega)+1)$ is the Bose factor arising from the condition of detailed balance. This is the resolution function in the time domain which is convoluted with a model for the correlation function before undergoing the Fourier transform to the energy domain where the calculated correction for the resolution volume and the Bose factor are made (this is convenient as both these factors lie outside the time integral in equation 3-10). The three sets of resolution conditions that were used in this experiment (the details of which will be given later) give rise to the functions shown in **figure 3.5** each of which acts as an envelope on the correlation function. It can be seen that the low resolution function cuts off ($R(t) < 0.5 \times 10^{-7}$) at $\approx 100\text{fs}$, the medium resolution at $\approx 1000\text{fs}$ and the high resolution reaches $\approx 2500\text{fs}$

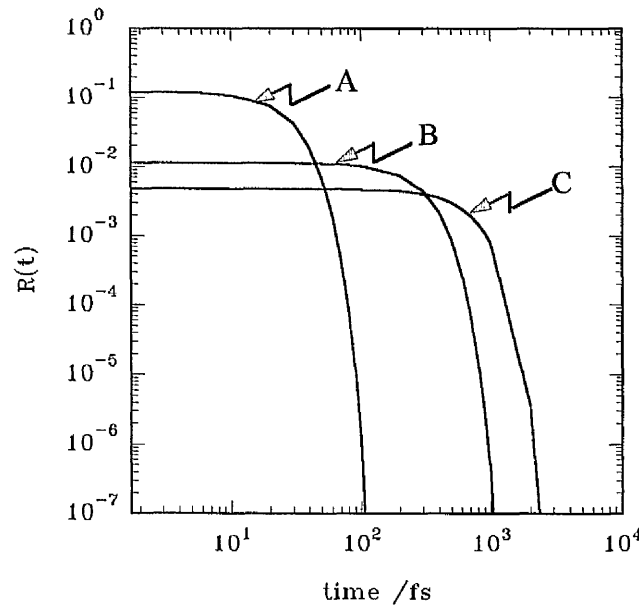


Figure 3.5. $R(t)$ shown for the three resolutions used in this experiment. A is the low resolution, B is medium resolution and C shows the high resolution. The y axis shows $R(t)$ down to 10^{-7} , which is the limit in accuracy of the software.

3.4.3 The Model for $C(t)$ and $S(q, \omega)$.

The theoretical prediction of the long time relaxation in an Ising system, (equation 3-5) is used to construct a correlation function valid for all times. At very short times we assume that there is a period before which the correlation function does not decay (or at

least decays very slowly), this is analogous to the finite time between collisions in Brownian motion. At long times we expect the form of the relaxation to be as predicted by Bray. In the intermediate regime we are unsure of the exact form, so we assume the form $C(t) \sim \exp(-t/\tau)$ where τ is a phenomenologically introduced relaxation time used to describe the critical scattering processes and any over-damped spin wave excitations (In a perfect Ising system these are indistinguishable. Here there may be some small difference but as none could be detected in the data a single time constant was assumed for both). The ambiguity arises in pin-pointing the cross-over from the intermediate time form to the long time form and also in how the cross-over is achieved numerically. The model used was a normalised sum of the two relaxation processes :

$$C(t) = \left(\frac{\exp\{-t/\tau\} + B \exp\left\{-A(\ln(t/t_0))^{3/2}\right\}}{\exp\{-t_0/\tau\} + B} \right), \quad t > t_0.$$

Equation 3-12

$$C(t) = (1.0), \quad t < t_0$$

Equation 3-13

The normalisation ensures that $C(q, t_0) = 1.0$. This is the full model for the relaxation process. It is convoluted with the resolution expression, $R(t)$ equation 3-11, and then transformed into q, ω space. The final detail is the addition of a background. The background is composed of two parts. Firstly there is a sample independent contribution from γ -rays and neutrons arriving at the detector from sources other than the spectrometer and from any electronic noise in the data acquisition systems. Secondly there is a background due to chemical disorder and nuclear spin incoherence, (these two sources are indistinguishable at room temperature). This scattering is strictly elastic and can be assumed to be isotropic, with only the Debye-Waller factor having any possible influence on its q -dependence. These elastic contributions give rise to a resolution limited central peak at room temperature the height of which is independent of both q and

temperature, at the small values of $|q|$ we are using. Static magnetic disorder would also make a truly elastic contribution to the scattering but this would be proportional to the magnetisation and hence zero above the transition temperature. The elastic part of the background can be measured and fixed in the room temperature scans. A flat (in q, ω space) background is added to account for the first mentioned source of background, and as we shall see later under certain circumstances is allowed to become negative to negate the unwanted short time contributions of the long time relaxation function.

3.4.4 Results.

For the $x=0.35$ crystal we have a full data set spanning three resolution conditions. Thus a complete analysis was achieved and a full discussion of the results is given here. The $x=0.05$ data set is incomplete due to a lack of experimental time. The preliminary results are discussed here with a view to completing the investigation at a later date.

The initial state of no relaxation was defined by t_0 in equation 3-12 this was fitted in the widest room temperature scan (low resolution) to be $(1.7 \pm 1.4) \times 10^{-15} \text{s}$. This value was then kept constant throughout the fitting process. In the low resolution data at room temperature the amplitude of the resolution limited elastic line was fitted along with the resolution width which was fitted with a Gaussian width of $0.0480(1) \text{THz}$. These two parameters along with the small time cut-off limit were fixed for all other temperatures in the low resolution data. All the other variable parameters are shown at their final fitted values in **table 3.1**. The long time tail is considered only as an addition to the elastic line (a constant in time, labelled “CP addition” in **table 3.1**, CP meaning central peak.) as under these resolution conditions this term is resolution limited. The values of τ are most accurate at this resolution in all but the 44K data, where it becomes resolution limited. The time constant increases with decreasing temperature corresponding to the narrowing of the critical scattering in the energy domain (see **figure 3.6**) and hence τ is

fixed at the low resolution values in the medium resolution data. The fitted data are shown in **figure 3.6**.

$k_z=2.1000\text{\AA}^{-1}$. Collimation is $60' 60' 60'$. Maximum energy= 0.5THz . Smallest energy step= 0.02THz .								
Temp /K	Back	Neg back	Amplitude	τ	B	A	CP addition	χ^2
295K	100±39	-	$0.62(5)\times 10^5$	1.05(7)	-	-	-	1.27
70K	188±30	-	$6.9(2)\times 10^5$	2.98(6)	-	-	-	1.57
64K	120±22	-	$9.51(9)\times 10^5$	3.62(4)	-	-	-	1.78
	113±24	-	$9.53(9)\times 10^5$	3.59(5)	-	-	10±10	1.80
54K	82±16	-	$19.1(7)\times 10^5$	6.04(4)	-	-	-	2.43
	61±18	-	$19.1(8)\times 10^5$	5.92(7)	-	-	57±20	2.31
44K	6.9±10	-	$77.34(9)\times 10^5$	18.77(5)	-	-	-	15.99
	0.007±9	-	$75.4(4)\times 10^5$	18.1(2)	-	-	645±128	8.95
	0.0006±2	-	$77.7(8)\times 10^5$	21.7	0.28	0.70	-	226.20
	-	-1.69(1)	$84.18(1)\times 10^5$	21.7	0.28	0.70	-	22.99
	-	-1.80(2)	$84.43(1)\times 10^5$	20.95(7)	0.28	0.70	-	9.73

Table 3.1. Data from the $x=0.35$ sample. The final fitted parameters for the low resolution data. The amplitude of the resolution limited central peak is 466(9), fitted in 295K data. The resolution width also fitted in the 295K data is 0.0480(1)THz. Each data set in the Griffiths phase is shown with and without a contribution to the resolution limited central peak (this represents the long time tail). The 44K data also shows the results of fits with the long time tail included explicitly with parameters fixed (in bold) at their values from higher resolution data. It is clear from this data that a resolution limited contribution to the scattering on top of the truly elastic scattering improves the quality of the fit.

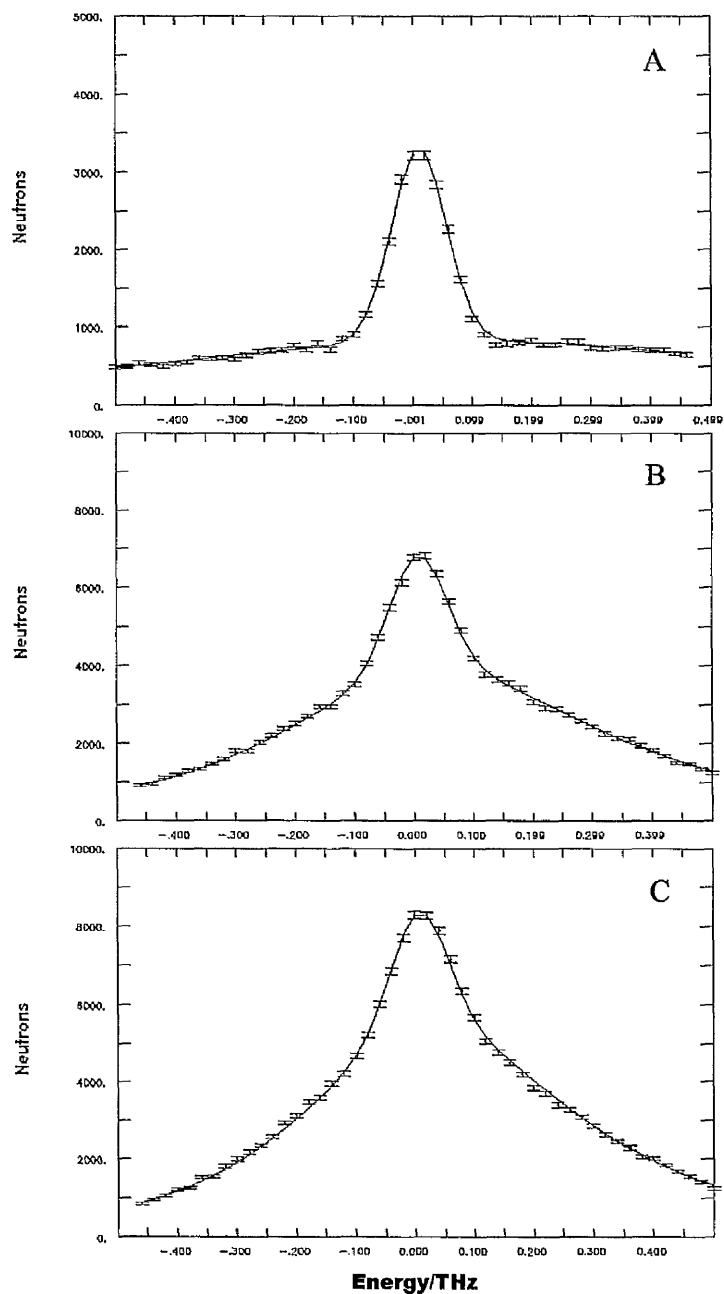


Figure 3.6. A,B and C. Final fits to the low resolution, $x=0.35$, data sets. **A** is room temperature data, **B** is data taken at 70K and **C** at 64K. The data is shown as points with error bars and the fit is given as a solid line. **C** has additional amplitude on the resolution limited central peak to describe the long time tail scattering.

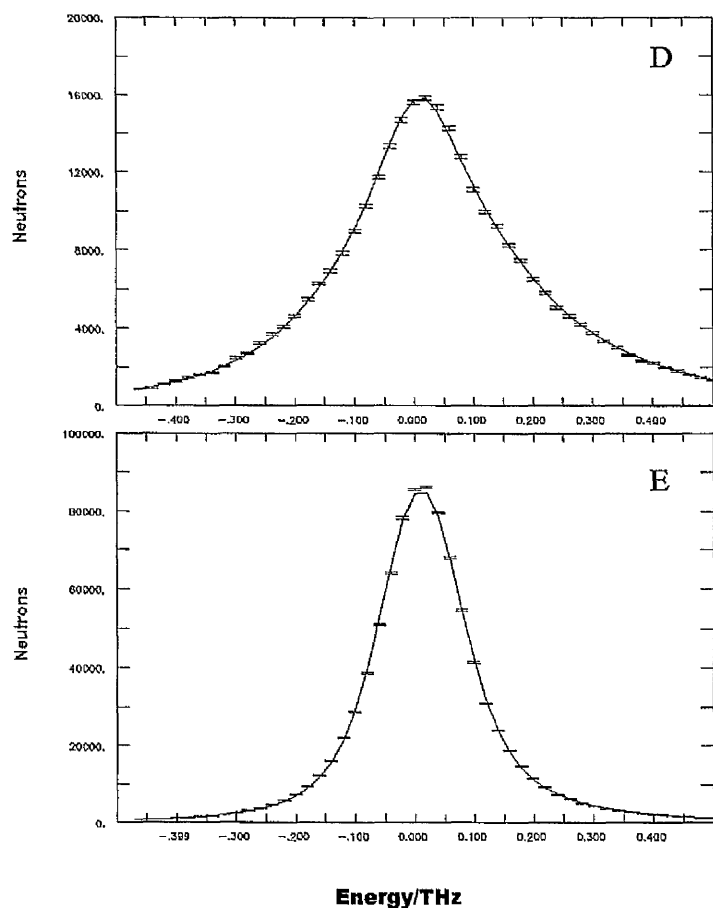


Figure 3.6D and E. Final fits to the low resolution, $x=0.35$, data sets. **D** was taken at 54K and **E** was data taken at 44K. **D** and **E** have additional amplitude on the resolution limited central peak to describe the long time tail scattering. In **E** the exponential relaxation processes are almost resolution limited.

The medium resolution room temperature data was similarly treated. The amplitude of the resolution limited elastic line was fitted and the resolution width was fitted to a Gaussian width of $0.004542(7)\text{THz}$. Again these were fixed in the other temperature data. The values of τ were fixed at the low resolution fitted values in all but the 44K data (A fit where it was free in the 54K data is shown in **table 3.2** for a check of self consistency). The long time tail is now treated explicitly with the inclusion of the parameters A and B . A is the amplitude in the exponent as defined in equation 3-5, B is the size of the additional contribution as defined in equation 3-12. The final parameters are shown in **table 3.2**. Each data set in the Griffiths phase was fitted with and without

the terms explicitly describing the long time tail. τ is fixed at the values fitted in the low resolution data except in the 54K data, where freeing it can be seen to have no effect, and the 44K data where there is a large difference between the low and medium resolution values. This is due to the exponential term being resolution limited at 44K in the low resolution scan and hence the exact line shape was difficult to determine. (see figure 3.6E).

$k_F=1.110\text{\AA}^{-1}$. Collimation is 60' 60' 60'. Max energy= 0.1THz. Smallest energy step= 0.004THz.							
Temp /K	Back	Neg back	Amplitude	τ	B	A	χ^2
295K	0.17±21	-	$3.6(1)\times 10^5$	1.05	-	-	1.65
70K	0.2±33	-	$57(8)\times 10^5$	2.98	-	-	2.25
	-	-0.009±11	$57(60)\times 10^5$	2.98	$(0.4\pm 7)\times 10^{-4}$	0.07±41	2.63
64K	0.3±37	-	$85(10)\times 10^5$	3.59	-	-	2.69
	-	-10(7)	$138(17)\times 10^5$	3.59	0.9(9)	1.29±1	1.25
54K	0.0005±2	-	$210(2)\times 10^5$	5.92	-	-	6.77
	-	-47(6)	$446(30)\times 10^5$	5.92	0.015(19)	0.44(30)	0.97
	-	-48±120	$(449\pm 615)\times 10^5$	5.92±3	0.011(15)	0.39(43)	1.02
44K	0.08±23	-	$107(22)\times 10^6$	18.1	-	-	31.93
	-	-555±299	$4(2)\times 10^9$	18.1	5(3)	1.2(1)	5.32
	-	-5.128±22	$120(9)\times 10^6$	21.7(9)	0.28(4)	0.70(6)	1.65

Table 3.2. The final fitted parameters for the medium resolution data taken with the $x=0.35$ sample. The amplitude of the resolution limited central peak is 183(4), fitted in the 295K data. The resolution width also fitted in the 295K data is 0.004542(7)THz (Gaussian width). Each data set in the Griffiths phase was fitted with and without the terms explicitly describing the long time tail. τ is fixed at the values fitted in the low resolution data except in the 54K data where freeing it can be seen to have no effect and the 44K data where there is a large difference between the low and medium resolution values. This is due to the exponential term being resolution limited at 44K (see figure 3.6).

The final fits are shown with the data in **figure 3.7**. The sixth frame of this figure (**3.7F**) shows the fit of **3.7E** but without the contribution from the non-exponential term in the correlation function. It is apparent that under these conditions the contribution is a substantial one.

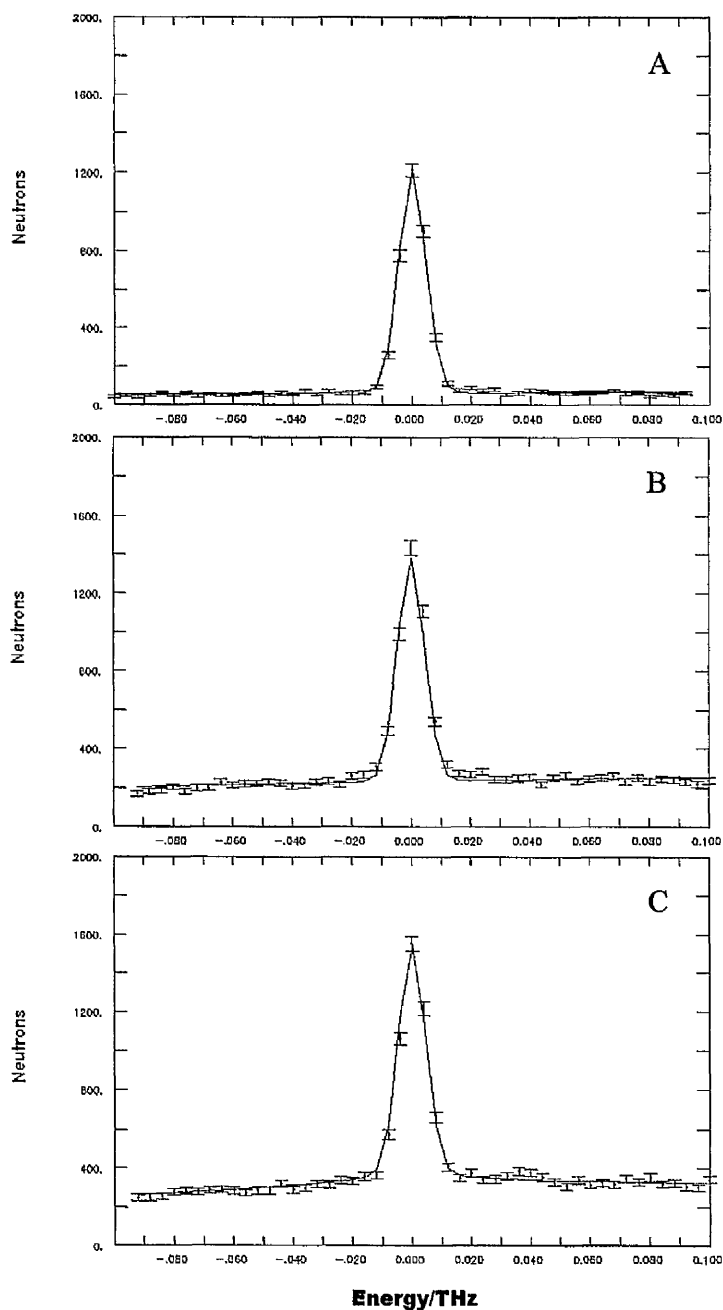


Figure 3.7A,B and C. Final fits to the medium resolution, $x=0.35$, data sets. **A** is room temperature data, **B** is data taken at 70K and **C** was taken at 64K.

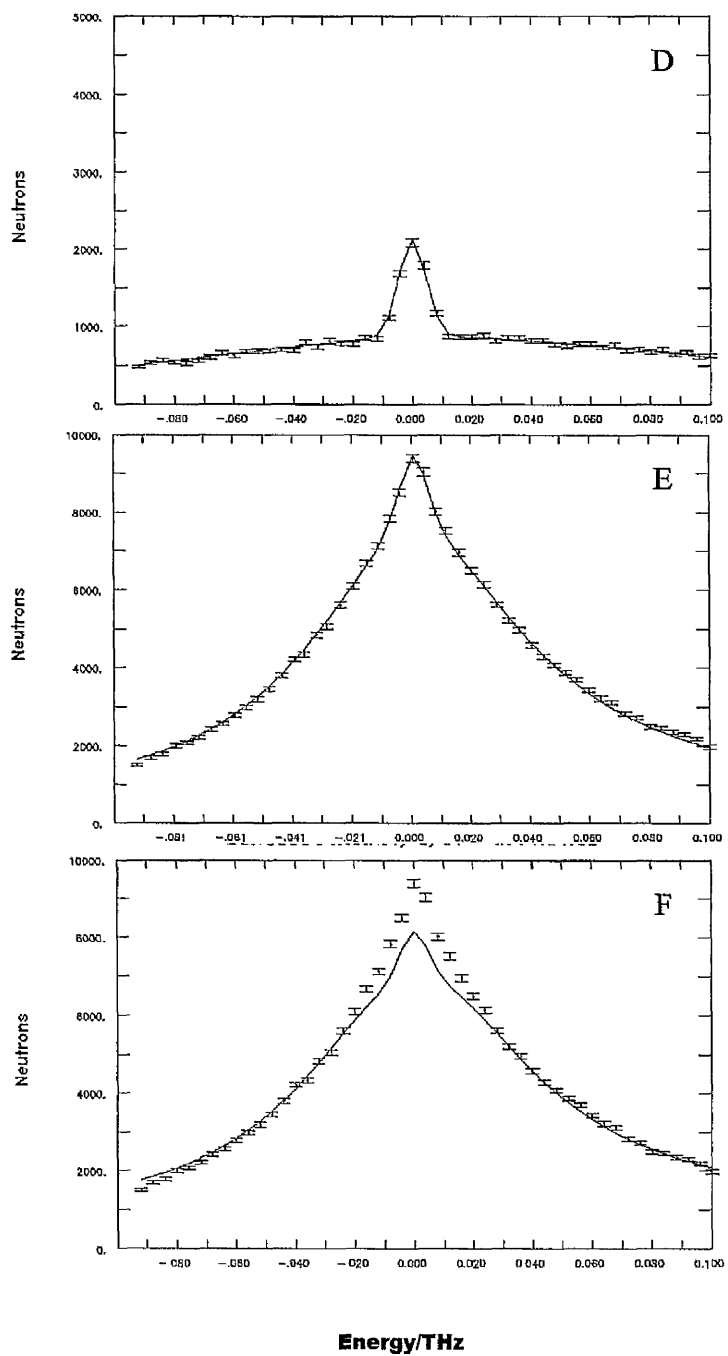


Figure 3.7D,E and F. Final fits to the medium resolution, $x=0.35$, data sets. **D** is 54K data and **E** is data taken at 44K. **F** is also the 44K data shown in **E** but without the non exponential term this is to demonstrate the size of the contribution at this temperature and is not fitted data.

The parameters fitted to the high resolution data are shown in **table 3.3**. Here the only free parameters initially are the background and overall scaling parameter (called Amplitude in these tables). After these were established the long time tail parameters were freed in the 44K data and allowed to fit. As **table 3.3** displays several permutations of free and fixed parameters were tried to reduce any errors due to highly correlated parameters. These data were particularly difficult to fit due primarily to much reduced number of data points, and much poorer statistics. Hence significant errors on the results. The final fits to the data are shown in **figure 3.8**.

$k_F=1.05 \text{ \AA}^{-1}$ collimation is $10' 10' 10'$, max energy= 0.007THz, smallest energy step= 0.001THz.						
Temp/ K	Background	Amplitude	τ	B	A	χ^2
295K	0.28±194	$(0.4\pm0.7)\times10^6$	1.05	-	-	0.47
70K	74±159	$(9.6\pm24)\times10^6$	2.98	-	-	1.25
44K	0.22±289	$(43\pm73)\times10^6$	21.7	0.28	0.70	1.44
	0.22±536	$(43\pm136)\times10^6$	21.7	4.5±350	0.7±2.3	1.56
	0.22±523	$(43\pm13)\times10^6$	21.7	4.5±85	0.70	1.56
	0.22	43×10^6	21.7	0.26±10	0.47±0.5	1.31

Table 3.3. The final fitted parameters for the high resolution, $x=0.35$, data. The amplitude of the resolution limited central peak is 10.5(9), fitted in the 295K data. The resolution width also fitted in the 295K data is 0.0019(2)THz (Gaussian width). At this resolution the scattering seen at 44K is exclusively the resolution limited peak and long time tail.

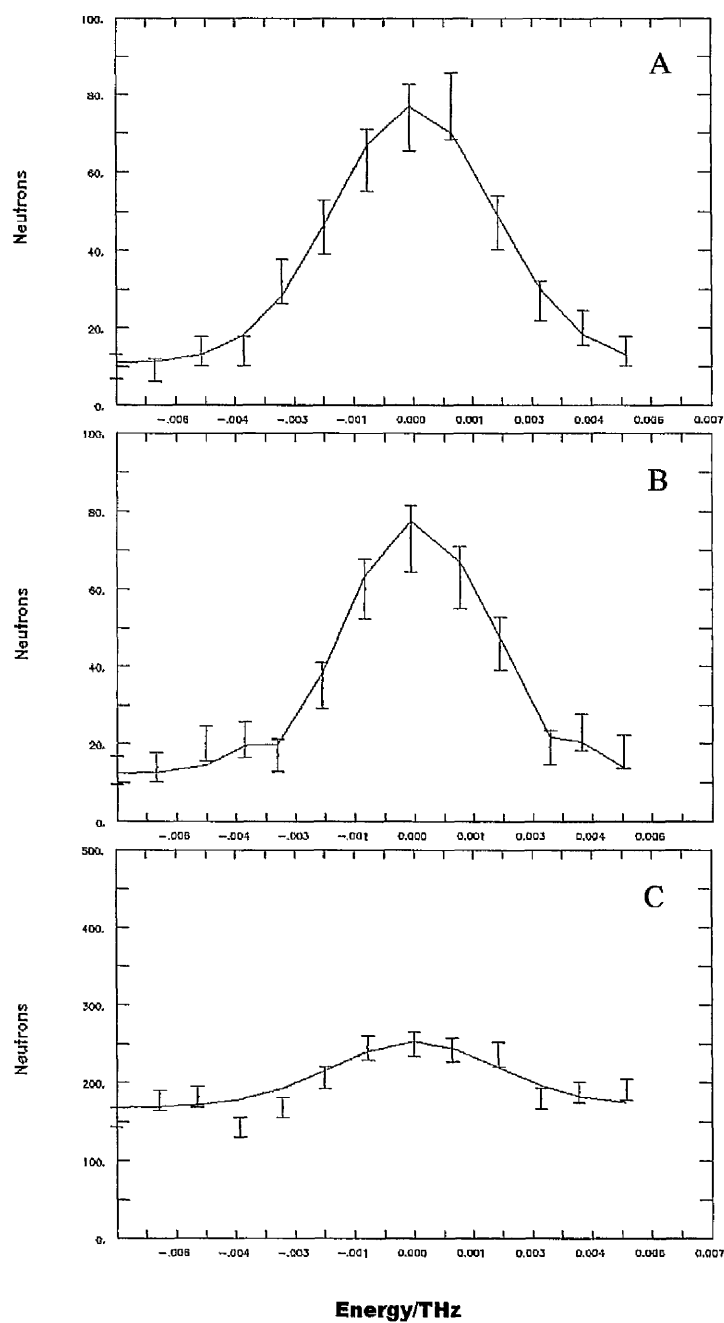


Figure 3.8A,B and C. Final fits to the high resolution, $x=0.35$, data sets. **A** is room temperature data, **B** is data taken at 70K and **C** is data taken at 44K.

The $x=0.05$ sample data were only taken at one resolution due to experimental time restrictions. It is therefore difficult to determine the correctness of parameters whose weight lie outside the time window of this resolution. Nevertheless there is convincing evidence of the non-exponential time tail although these data should be treated as only a qualitative indication of the relaxation processes. The results of fitting the same model $C(t)$ as previously can be seen in **table 3.4**.

$k_f=1.110\text{\AA}^{-1}$ Collimation is $60' 60' 60'$ Max energy= 0.1THz Smallest energy step= 0.004THz.							
Temp/K	Back (4)	neg back	Amp	τ	B	A	χ^2
293.2	0.45 ± 18	-	$0.23(9)\times 10^5$	5(1)	-	-	1.32
70.0	0.01 ± 63	-	$37(1)\times 10^6$	11.5(1)	-	-	2.87
	0.001 ± 5	-	$38(2)\times 10$	11.6(1)	C.P.= 0.002 ± 7		3.14
	-	-1.67 ± 4	$38(3)\times 10^6$	11.7(3)	0.03 ± 0.4	4.1(5)	2.10
66.3	372 ± 44	-	$76.7(8)\times 10^6$	22.1(2)	-	-	10.77
	85 ± 54	-	$80.9(9)\times 10^6$	20.2(2)	C.P.= 23 ± 15		10.00
	-	-42 ± 91	$106\pm 22\times 10^6$	21(3)	0.6(5)	0.8(6)	5.25
65.6	1057 ± 35	-	$96.4(6)\times 10^6$	29.4(2)	-	-	34.34
	448 ± 26	-	$104.7(8)\times 10$	24.8(2)	C.P.= 567 ± 20		20.36
	-	-73(3)	$153.7\pm 98\times 10^6$	25(2)	0.7(4)	0.75(5)	4.96
64.9	1608 ± 29	-	$113.7(5)\times 10^6$	37.6(2)	-	-	87.34
	759 ± 39	-	$122.8(6)\times 10^6$	29.9(2)	C.P.= 1168 ± 26		32.67
	-	-69(5)	$179(2)\times 10^6$	27(2)	0.8(3)	0.6(1)	16.13

Table 3.4. The final fitted parameters for the $x=0.05$ sample. The amplitude of the resolution limited central peak is 20(2), fitted in the 293.2K data. The resolution width also fitted in the 295K data is 0.0051(7)THz (Gaussian width). Each data set in the Griffiths phase (all sets in this table below 67K) were fitted without any long time tail, with the central peak addition that approximates the long time tail (C.P.) and also with the terms explicitly describing the long time tail.

3.5 Interpretation of Results.

The results shown in **tables 3.1, 3.2 and 3.3** require some interpretation to explain the apparent inconsistencies between the values of fitted parameters across the different resolutions and why the background has become negative in some cases. These subtleties are best illustrated by example. The complete correlation function as fitted to the 44K medium resolution data is plotted as a function of time in **figure 3.9A**. (Note: this is a log log plot.) Along with the combined correlation function the long time tail component and the exponential component are also shown to indicate how the combined function deviates from the individual functions in different time windows. Also shown in **figure 3.9A** (and **B** and **C** where appropriate) are what are labelled the “cut off” of each of the three resolutions. In each case this is the point at which the resolution function, $R(t)$, falls below the decimal precision used on the computer, in this case 0.5×10^{-6} . (See the full time dependent resolution envelope in **figure 3.5**.) It is where the correlation function is suppressed to zero by the resolution, this is an absolute cut off but it is worth emphasising that the closer to this cut off in time the less reliable the fit becomes. (see discussion in section 3.4.1). It is clear that the tighter the resolution the longer the times that become available to us. Referring back to the results and looking only at the 44K parameters which are summarised in **table 3.5**. It is not unreasonable to expect the values of τ and the non-exponential terms to be consistent across all resolutions as the physics does not change.

Resolution (44K)	Background	τ	B	A	χ^2
Low	0.007 ± 9	18.1(2)	645 ± 128 (C.P.addition)		8.95
Medium	-5.1 ± 22	21.7(9)	0.28(4)	0.70(6)	1.65
High	0.22 ± 500	21.7(9)	0.26 ± 10	0.47 ± 0.5	1.31

Table 3.5. A summary of the 44K data from previous tables.

The reasons for these inconsistencies are demonstrated in **figure 3.9B** and **C**. These two areas are the main sources of difficulty. We can see that at very short times (**3.9B**) the addition of the long time tail expression raises the exponential function. This has no basis in physics. The long time tail is not correct at these short times and only the exponential term is required. This unwanted effect can be partially suppressed by allowing the energy background to become negative.

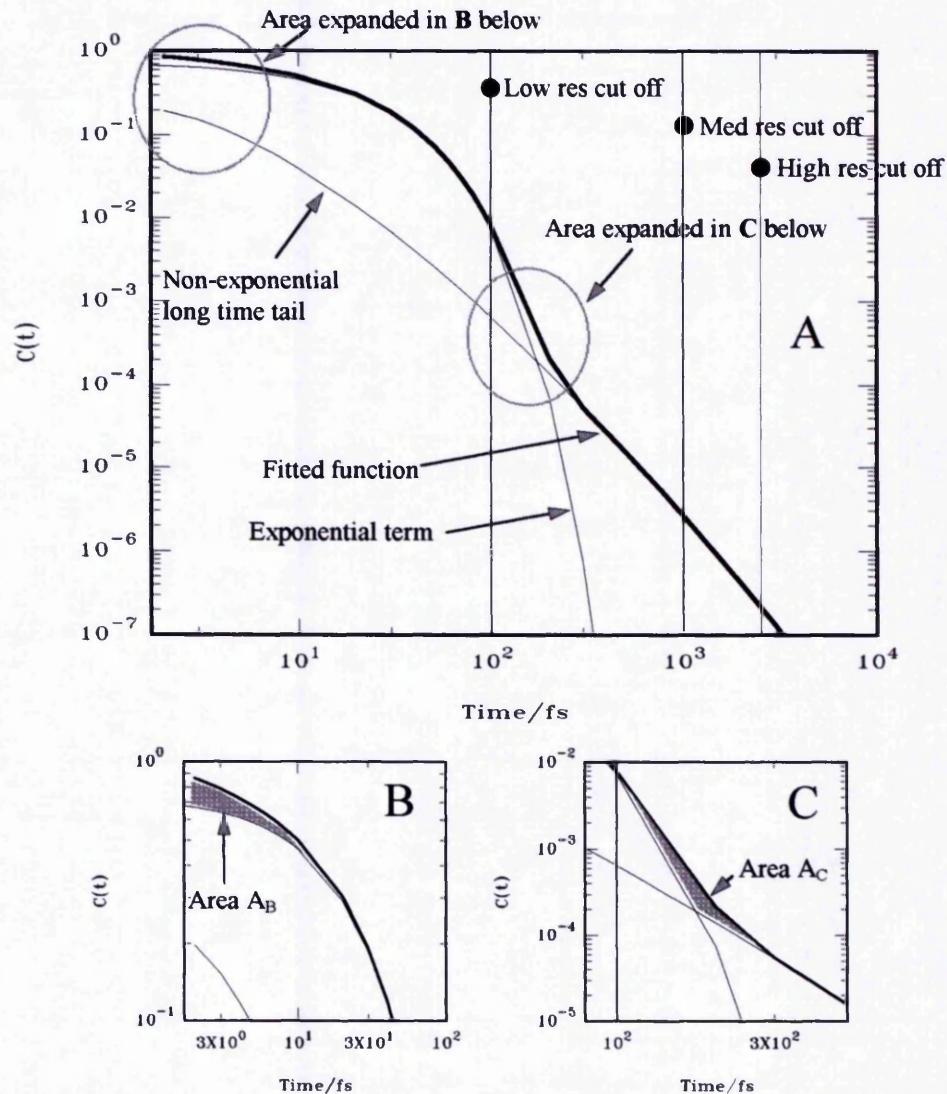


Figure 3.9A,B and C. A shows the variation of the correlation function with time, the two components are shown along with the full relaxation function. B and C

We can see in **table 3.5** that the background fits preferentially negative in the medium resolution data. The low resolution fit does not include the full form of the non-exponential term hence this does not have a negative background. However, when the values of the non-exponential parameters are fixed in the low resolution data the background is forced negative (see **table 3.1**). This effect is not seen in the high resolution data as the much smaller energy width, $\pm 0.007\text{THz}$, reduces the influence of the small time details. In addition to introducing the need for a negative background (which is an imperfect correction) this unwanted weight at short times, combined with modelling the long time tail with a simple addition to resolution limited scattering, distorts the measurement of τ in the low resolution fits, explaining the discrepancy in these values.

We can also see a second area where the influence of the long time tail is large. **Figure 3.9B** shows an area just above the cut off of the low resolution data where the 'cross-over' from primarily exponential relaxation to primarily non exponential relaxation occurs. This area inevitably gives rise to different values of the non-exponential parameters in the high and medium resolutions. The anomaly carries more weight in the medium resolution data than in the high resolution data as it is closer to the cut off in the medium resolution data. The results are consistent with this, where as the amplitude of the non-exponential term is similar in both resolutions, the parameter A is larger in the medium resolution data, corresponding to the long time term cutting through the top of the shaded area A_c in **figure 3.9C** and extending to longer times.

Although all these points of discussion have been illustrated using the 44K data a similar process of interpretation can be applied to the other temperature data for the $x=0.35$ sample although the increase in uncertainty on the parameters in the other cases make such detailed interpretation difficult. The lack of other resolution data for the $x=0.05$ sample means that such interpretation is impossible, hence the $x=0.05$ data should be

treated only in a qualitative manner. The $x=0.05$ data shows the existence of a long time relaxation process which exists in the Griffiths phase.

3.6 Conclusions and Further Work.

In conclusion we have performed a series of measurements of the power spectrum of spin fluctuations in the dilute Ising antiferromagnet $\text{Mn}_{1-x}\text{Zn}_x\text{F}_2$, fully for $x=0.35$ and partially for $x=0.05$. Evidence for the non-exponential time tail predicted by Bray and others is clear in all data taken in the Griffiths phase and is clearly absent in data taken above the Griffiths temperature. We have been able to fit the functional form of the relaxation predicted by Bray and have extracted values for the size of this relaxation and the parameter B in Brays work. The non-exponential decay starts to dominate when the correlation function has decayed exponentially to $\sim 1\%$ of its zero time value, which is consistent with previous measurements²⁹. This form of long time function describes our data very well with $\chi^2 \sim 1.5$ for all data where the function was explicitly fitted. At 44K for $x=0.35$ ($T_c=40.0$) the amplitude was found to be $0.28(4)$ and parameter $A=0.70(6)$. Higher resolution measurements gave 0.26 ± 10 and $A=0.47 \pm 0.50$ but the correlation between the parameters made the errors prohibitively large. At 54K $B=0.011(15)$ and $A=0.39(43)$ these large errors make a quantitative discussion at this temperature difficult, the implication appears to be that the magnitude of the effect, which is directly related to the size and number of quasi-ordered clusters, drops off dramatically with temperature. This and the higher temperature data are not inconsistent with the expected trends for A and B . The $x=0.05$ ($T_c=64.3$) data are also consistent with this picture although the incomplete nature of this data should discourage any great emphasis being put upon these results.

This experiment provides the basis for an ongoing full quantitative characterisation of Griffiths dynamics. The $x=0.35$ investigation requires high resolution data for the temperatures other than 44K to enable the ambiguity of large errors due to correlated parameters to be cleared up. The $x=0.05$ data should be completed with higher and lower resolution data collected. It is tempting at this stage to propose a neutron spin echo

experiment to observe directly the relaxation process. In the Ising case the Griffiths signature is more pronounced (the magnitude of non-exponential term at $(T-T_C)/T_C=0.10$ was 0.26) than the Heisenberg case (magnitude of non-exponential term at $(T-T_C)/T_C=0.05$ was 0.044). The problem still remains that the effect is only dominant after the exponential relaxation decayed to 1% which is at the limit of the sensitivity of such an experiment.

This chapter presents a direct and quantitative measurement of the non-exponential relaxation, which is the signature of the Griffiths phase. The predictions of Bray appear to hold, implying that the behaviour of the long time dynamics is dominated by rare quasi-ordered regions.

3.7 References.

- ¹ Lloyd R.G. and Mitchell P.W., J.Phys: Condensed Matter **1** pp5013 (1989)
- ² Dhar D. "Stochastic Processes: Formalism and applications" S.Agarwal and S. Dattagupta eds. Springer, Berlin. (1983).
- ³ Randeria M., Sethna J.P, Palmer R.G., Phys. Rev. Lett. **54** pp1321 (1985)
- ⁴ Bray A.J., Phys. Rev. Lett. **59** pp586 (1987)
- ⁵ Bray A.J., Phys. Rev. Lett. **60** pp720 (1988)
- ⁶ Bray A.J., J.Phys.A:Math.Gen. **22** L81 (1989)
- ⁷ Dhar D., Randeria M. and Sethna J.P. Europhys. Lett. **5** pp485 (1988)
- ⁸ Bray A.J. and Rodgers G.J. J.Phys. C:Solid State Phys. **21** L243 (1988)
- ⁹ Bray A.J. and Rodgers G.J. Phys.Rev.**B38** pp9252 (1988)
- ¹⁰ Bray A.J. and Moore M.A. J.Phys. C:Solid State Phys. **15** L765 (1982)
- ¹¹ Rammal R.,J.Physique **46** pp1837 (1985)
- ¹² Kohlrausch Ann.Phys.Lpz **12** pp393 (1847)
- ¹³ Nusser A.,J.Phys **A24** pp2355 (1991)
- ¹⁴ Colborne S.G.W. and Bray A.J. J.Phys. A: Math. Gen. **22** pp2505 (1989)
- ¹⁵ Takano H. and Miyashita S., Journal of the Physical society of Japan. **64** 2 pp423 (1995)
- ¹⁶ Takayama H. and Yoshino H., Journal of the Physical society of Japan. **64** 8 pp2766 (1995)
- ¹⁷ Jain S.,Physica A **218** No3-4 pp279 (1995).
- ¹⁸ Komori T.,Hukushima K. and Takayama H. Journal of the Physical society of Japan. **64** 11 pp4418 (1995)
- ¹⁹ Komori T and Takayama H., International Journal of Modern Physics C-Physics and Computers. **7** 3 pp371 (1996)

-
- ²⁰ Grassberger P., International Journal of Modern Physics C-Physics and Computers. **7** 1 pp89 (1996)
- ²¹ Hohenburg P.C. and Halperin B. I., Rev. Mod. Phys. **49** pp435 (1977)
- ²² Boekema C., Suarez I.M., Lam J.C., Hoffman T.J., Lajoie E.N., Weathersby S.F., Flint J.A., Lichti R.L., Wang C.P. and Cooke D.W., Hyperfine Interactions **64** 1 pp467 (1990)
- ²³ Binek C. and Kleeman W., Phys. Rev. Lett. **72** pp1287 (1994)
- ²⁴ Binek C. and Kleeman W., Acta Physica Slovaca **44** pp435 (1994)
- ²⁵ Binek C., De Azevedo M.M.P., Kleeman W. and Bertrand D. J. Mag. Mag. Mat. **140-144** 3 pp1555 (1995)
- ²⁶ Binek C., Bertrand D. J., Regnault L.P. and Kleeman W., Phys Rev B. **54** 13 pp9015 (1996)
- ²⁷ Mitchell P.W., Cowley R.A., Yoshizawa H., Böni P., Uemura Y.J. and Birgeneau R.J. Physical Review B. **34** 7 pp4719 (1986)
- ²⁸ Instrument details. <http://www.ill.fr/> (1997)
- ²⁹ Lloyd R.G., Ph.D. Thesis, University of Manchester. (1989)
- ³⁰ Press W.H., Flannery B.P., Teukolsky S.A. and Vetterlink W.T. "Numerical Recipes: The Art of Scientific Computing" Cambridge University Press. (1986)
- ³¹ Dorner B., Acta Crystallogra. **A28** pp319 (1972)
- ³² Cooper M.J. and Nathans R., Acta Cryst. **23** pp357 (1967)

Chapter 4. A Search For Magnetic Order in α -Titanium.

4.1 Introduction.

Titanium is the most naturally abundant transition metal after iron. Titanium, atomic number 22, is a silver grey metal with a density of 4.5g cm^{-3} . It has two principal allotropic modifications, α and β Titanium: α -Ti has a hexagonal-close-packed (hcp) crystal structure and exists below 1115K; β -Ti has a body centred cubic crystal structure which exists above that temperature until its boiling point at 1670K. It is the lower temperature phase, α -titanium, that we are concerned with here.

Interesting magnetic features are common to the transition metals. Iron, nickel and cobalt are all itinerant electron ferromagnets and chromium and manganese are known to be itinerant electron antiferromagnets. The magnetic complexities common to the transition metals arise due to the partially filled 3d, 4d or 5d electron shells and the associated electronic energy band structure around the Fermi level. The electron wavefunctions of the d-electrons on adjacent atoms overlap and thus complex band structures arise. There has been widespread interest in both vanadium and titanium despite the fact that both these metals are superconducting at low temperatures (vanadium at 5.38K and titanium at 0.39K). The exposure of magnetic ordering within these elements would be of great interest beyond its purely intrinsic value.

α -titanium is generally considered to be a Pauli paramagnet but work carried out by Pop et al¹ has suggested a magnetic phase transition. The evidence put forward by Pop is in

three forms. An anomaly in the bulk magnetic susceptibility was observed at 276K. This is shown in **figure 4.1** and takes the form of a change in gradient of the susceptibility as a function of temperature. This deviation indicates a departure from simple Pauli-paramagnetism;

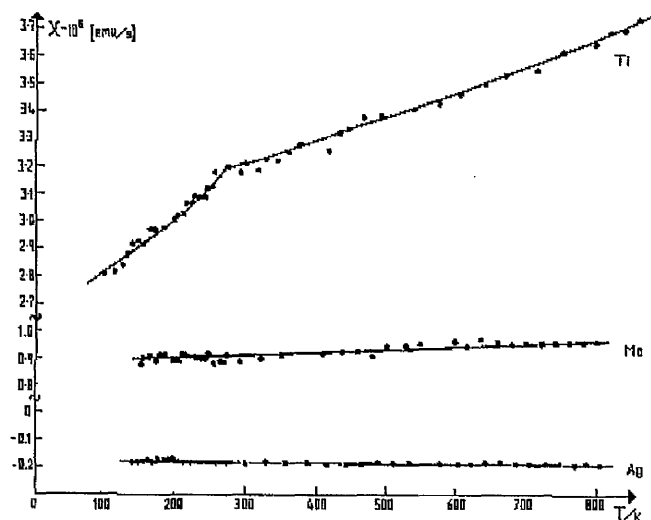


Figure 4.1. Magnetic susceptibility of α -titanium as a function of temperature taken from Pop et al¹. Also shown are comparative results for pure Mo and Ag. The anomaly in titanium is at 276K.

Electrical resistivity measurements, shown in **figure 4.2** also present an anomaly at the same temperature;

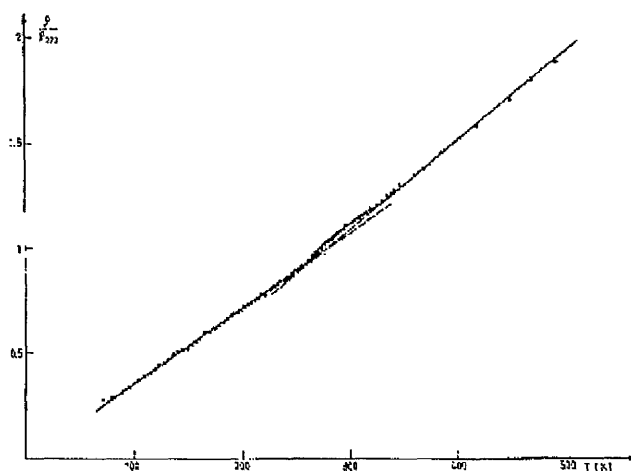


Figure 4.2. Electrical resistivity as a function of temperature from Pop et al¹.

A cusp in the specific heat measurements (**figure 4.3**) is also observed indicating a continuous phase transition.

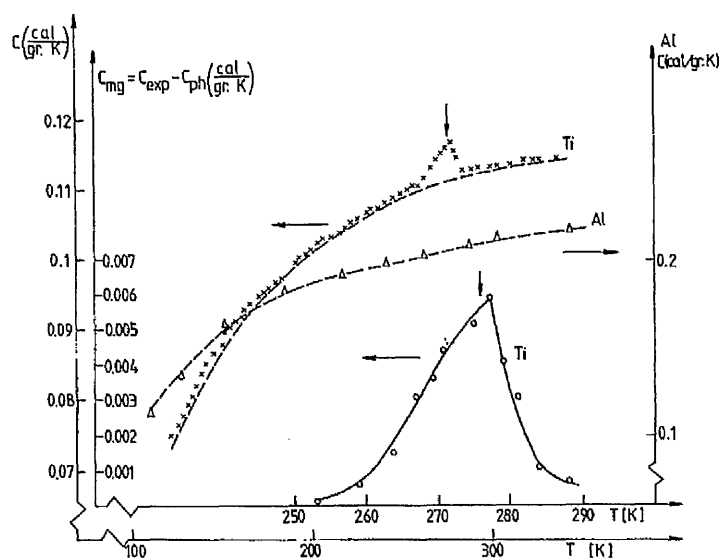


Figure 4.3 Specific heat measurements as a function of temperature from Pop et al¹. Specific heat measurements for aluminium are shown for comparison.

Pop et al¹ concludes from this evidence that due to the strong similarity between the magnetic susceptibility of α -titanium and that of chromium (see **figure 4.5** page 100.) it is possible that what is being observed is a transition from Pauli-paramagnetism to an itinerant electron antiferromagnet. The values of susceptibility obtained by Pop agree with previous measurements^{2,3,4,5}, although no anomaly had previously been mentioned, possibly because earlier data did not include the temperature range of interest. The density of states calculated from Pop's susceptibility measurements (given the assumption that titanium is an antiferromagnet) agrees with the value calculated from their specific heat measurements. The observed Néel temperature from Pop's work is (276 ± 4) K.

Since the publication of Pops work several other groups^{6,7,8} have looked for evidence to support these claims. Measurements of susceptibility, resistivity, and speed of sound have

been made along with a polarised neutron powder diffraction measurement. None of these experiments have observed the anomalies shown by Pop.

Aside from Pop's antiferromagnet hypothesis there are two other main candidates which could be responsible for the observations; The anomalies could be related to impurities, titanium hydride is known to display such anomalies in the susceptibility due to the presence of a charge density wave. It is also possible that a structural phase change is responsible. These possibilities are given further consideration later in this chapter.

The observations of Pop et al¹ were the motivation for a series of experiments performed by the Manchester group, bulk susceptibility, neutron powder diffraction, neutron single crystal diffraction, and muon spin relaxation experiments have been performed and are documented in chronological order in this chapter.

4.2 The Experiments.

4.2.1 Vibrating Sample Magnetometer Measurements of the Bulk Susceptibility of α -Titanium.

As a starting point for an investigation of Pop et al's¹ claims we set about reproducing the bulk magnetic susceptibility measurements. This experiment was initially performed by J.R.Lowden¹⁰ although further investigations including the de-gassing of samples to remove any hydrogen present and the characterising of all samples used in further experiments was carried out by the author using the same method, hence, a description of the apparatus and method is included.

4.2.1.1 Instrumentation and Method.

An Oxford Instruments Vibrating Sample Magnetometer (VSM) was used to perform these measurements. The VSM vibrates the sample in a magnetic field and the magnetic moment of the sample induces a signal in a set of pick up coils. It therefore measures the bulk magnetisation, M , directly. A schematic of the VSM (at Manchester) is shown in **figure 4.4**. The sample was fixed to the end of the sample rod with Cotronics 918 ceramic cement and bound with PTFE tape for added security. The rod was tightly screwed into the transducer which during operation vibrates the rod along the vertical axis. The sample is lowered down into the centre of the 12 Tesla superconducting magnet which supplies the large external magnetic fields used. Temperature control is achieved using a gas-flow cryostat controlled by an ITC4 Oxford Instruments three term temperature controller which has a temperature range of 3 to 400K. Helium gas is blown over the sample at a variable rate while a resistance heater controls the gas temperature. For temperatures higher than 400K a furnace can be used, but to maintain continuity in our measurements only the cryostat was used. Experimentally the signal is optimised by scanning the sample vertically with the transducer on and then the rod moved and fixed

in the maximum signal position. Three types of measurement were made for each data set:

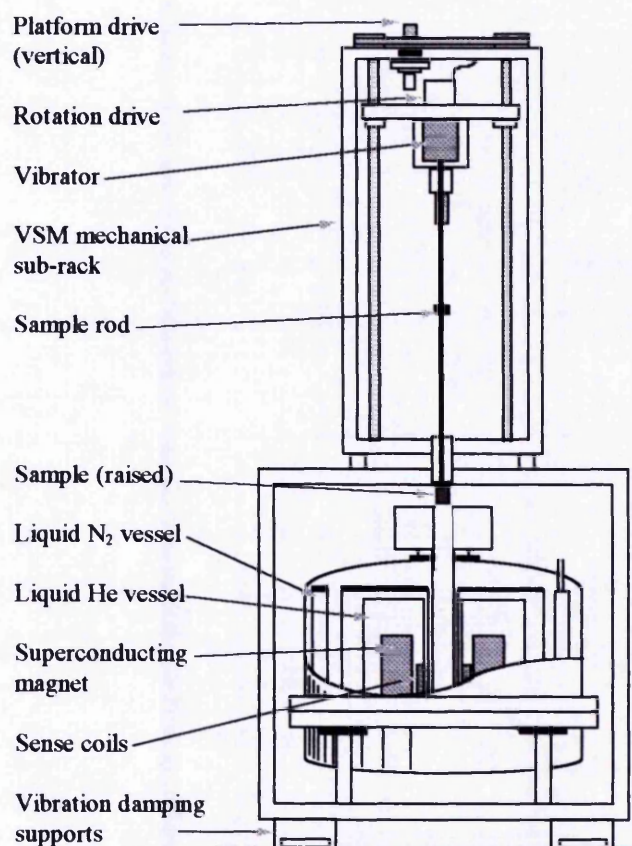


Figure 4.4 A schematic representation of the Manchester vibrating sample magnetometer.

- Firstly a calibration run with the sample rod, adhesive and PTFE tape but not the sample;
- Secondly the magnetisation as a function of field was checked to ensure the linear nature of the M - H relationship for titanium;
- Thirdly the magnetisation as a function of temperature in a fixed field of 10 Tesla.

Several samples of titanium were used throughout the experiments described in this chapter. The principal samples were 99.99% purity titanium rods supplied by Goodfellow Metals. These were 100mm long 9mm diameter polycrystalline cylindrical samples that were used for all the neutron powder diffraction experiments and the initial

VSM investigation. These samples were cut into 45mm long rods for the neutron experiments and into smaller 10mm sections for the VSM work. Spark erosion was the chosen method for cutting the samples. This is a chemically extremely clean method (and moreover, one of the few feasible methods of cutting titanium). An x-ray fluorescence study performed by Dr.J.Esson⁹, of a sample on an un-cut and a cut face showed no additional chemical impurities due to the cutting process. Two other samples were also obtained; a large single crystal of unknown purity used in the single crystal experiments and a 100mm square 2mm thick flat plate of 99.999% pure polycrystalline Ti used in the muon implantation experiment. These other two samples had small sections spark cut from them for the VSM analysis.

4.2.1.2 Results and Discussion.

The VSM produces raw data of the form absolute magnetisation versus temperature. The data were normalised by the 'blank' calibration run, i.e. the calibration data was subtracted from the sample data for comparative purposes. The mass of the sample and applied field can be used to obtain a mass susceptibility. No further data manipulation was required.

The VSM data shown throughout this chapter are fitted to a first order approximation to the standard T^2 dependency used by Pop that was adequate for the temperature ranges within which the data was taken. A simple linear function i.e. for $T \leq T_N$;

$$\chi = A + BT$$

Equation 4-1

and for $T > T_N$;

$$\chi = A + (B - C)T_N + CT$$

Equation 4-2

where A, B, C and T_N are free parameters. All fitting was carried out using a least squares non-linear regression fitting program.

The initial susceptibility measurements made by J.R.Lowden¹⁰ on 99.99% purity α -titanium, 99.9% purity α -titanium and 99.99% purity chromium can be seen in **figure 4.5**. With data for the other three samples in **figure 4.6**, **figure 4.7** and **figure 4.8**. The results of fits to these data can be seen in **table 4.1**

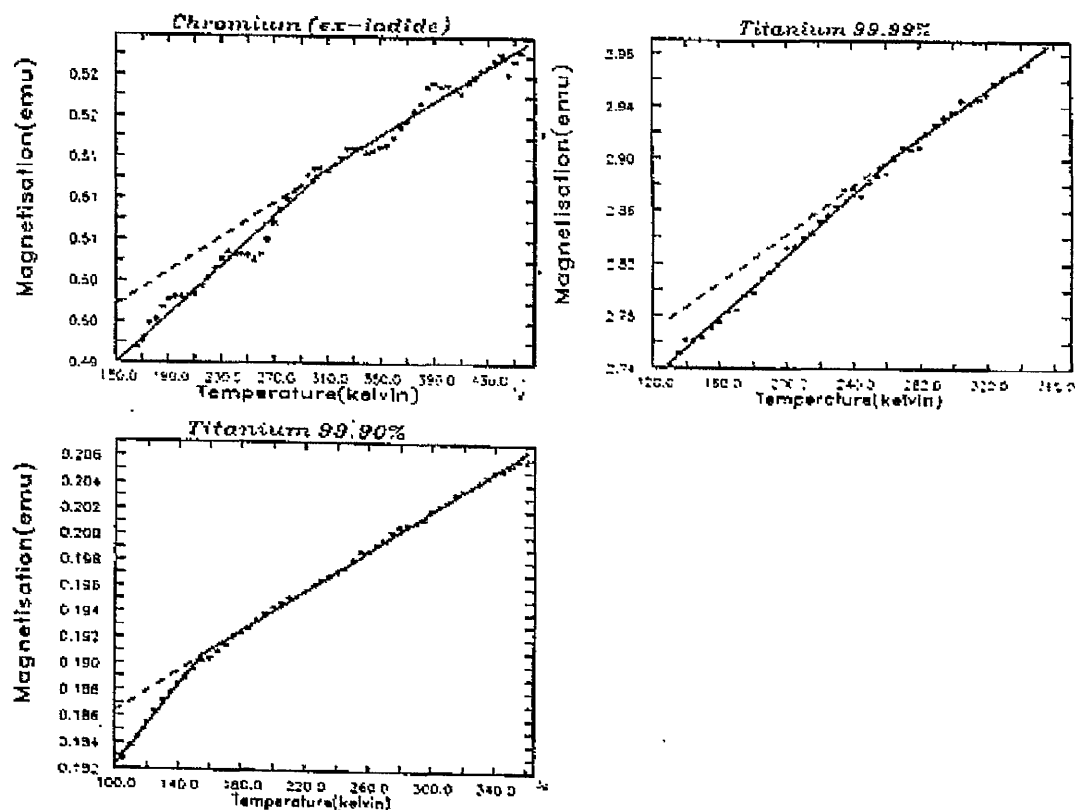


Figure 4.5 Magnetisation as a function of temperature for 99.99% Cr, 99.99% Ti and 99.9% Ti showing respective fitted transition temperatures of, $(306 \pm 3)\text{K}$, $(260 \pm 5)\text{K}$ and $(155 \pm 2)\text{K}$. The oscillations seen in the chromium data are due to poor temperature stability during this run.

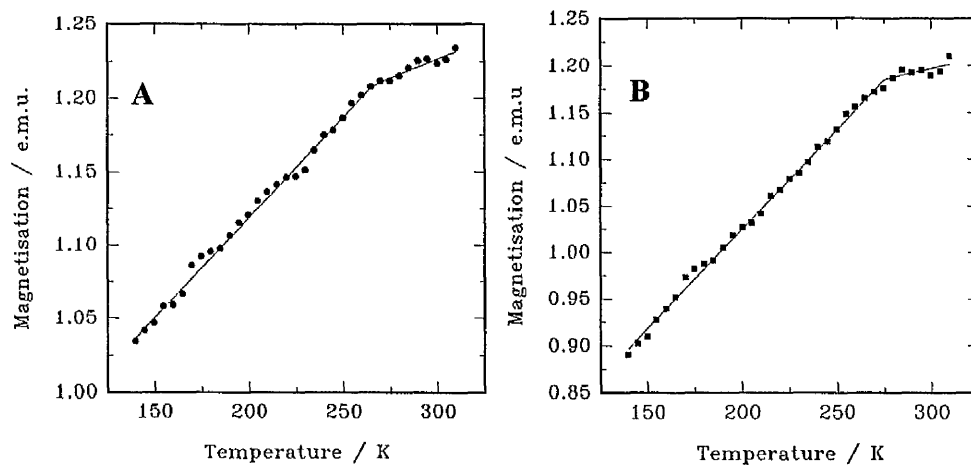


Figure 4.6. Magnetisation as a function of temperature for polycrystalline α -Ti, before (A) and after (B) de-gassing at 800K. Fits to the data are also shown.

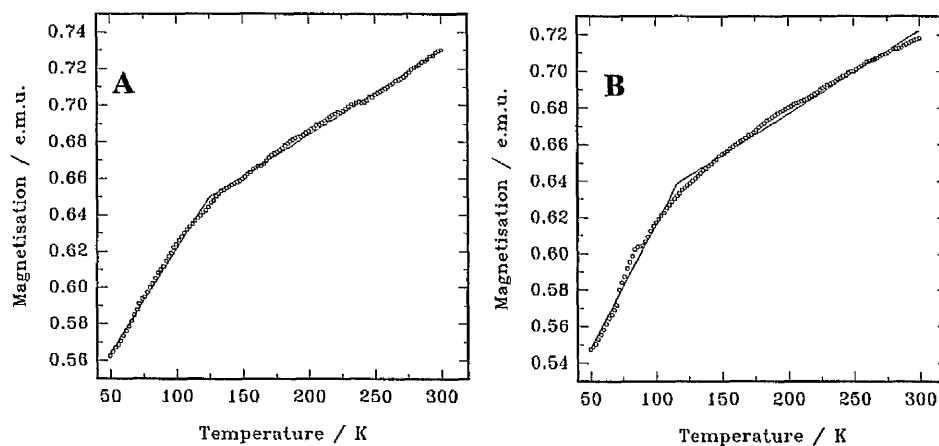


Figure 4.7 Magnetisation as a function of temperature for a single crystal of α -titanium before (A) and after (B) de-gassing at 800K. Fits to the data are also shown.

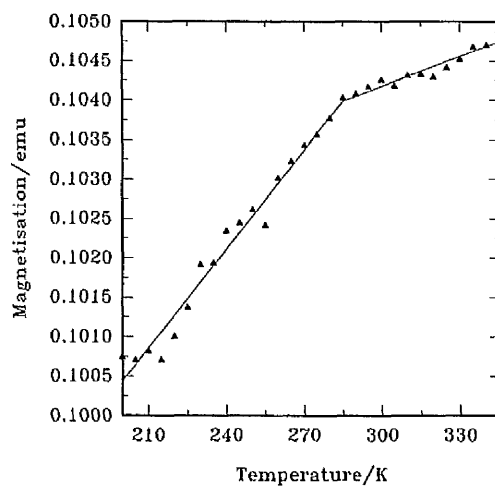


Figure 4.8. Magnetisation as a function of temperature for 99.999% purity α -titanium. A fit to the data is also shown.

The results of the fitted data tell us two things. Firstly, in samples of the same purity to those that Pop worked with the anomaly is present in the same form at the same temperature. Secondly, the anomaly is highly sensitive to sample purity, demonstrated by the results shown in **table 4.1**.

Sample Purity. (* Indicates work by J.R.Lowden.)	Transition temperature before de-gassing	Transition temperature after de-gassing
99.999%	(284 \pm 5)K	No data
99.99%*	(260 \pm 5)K	No data
99.99%	(266 \pm 4)K	(275 \pm 4)K
99.9%*	(155 \pm 2)K	No data
Unknown (Single Crystal)	(125 \pm 8)K	(116 \pm 12)K

Table 4.1. A comparison of the purity and measured transition temperature of α -titanium samples used in the experiments described in this chapter

4.2.2 A Neutron Diffraction Experiment on α -Titanium Performed on POLARIS at ISIS.

The experiment described in this section was performed by J.R.Lowden who also undertook the associated data analysis. A full account of the experiment and details of the data analysis can be found in Lowden's Ph.D. thesis¹⁰.

POLARIS is situated on the ISIS spallation neutron source. Originally intended as a polarised neutron instrument it is now used exclusively as a powder diffractometer. It has high intensity and medium resolution providing diffraction spectra up to very large d-spacings with incident wavelength 0.1Å to 6.0Å. The instrument has four detector banks, A, B, C and D. A detector bank consists of 12 ^3He tubes at 1.1 to 2.4m from the sample ($14^\circ < 2\theta < 30^\circ$), B detector bank has 20 ^3He tubes at 2.0m from the sample ($85^\circ < 2\theta < 95^\circ$), C bank has 10 ^3He tubes at 0.7 to 0.9m from the sample ($135^\circ < 2\theta < 158^\circ$) and D bank has 20 ZnS elements at 1.0m from the sample ($80^\circ < 2\theta < 90^\circ$). Together this array of detectors allow diffraction spectra from d-spacings as large as 20Å.

A square array of four 45mm long polycrystalline rods cut from the Goodfellow's metals' samples described in section 4.2.1.1 was mounted on an aluminium block and placed in a closed cycle helium refrigerator (CCR). The sample was first cooled to 15K and data collected for 12 hours at this temperature. The sample was then heated to 350K and data collected for 12 hours. A peak not corresponding to the hexagonal close packed chemical structure was observed in the low temperature data which was absent in the high temperature data (**Figure 4.9**). Its $|q|$ was found to be $(1.96 \pm 0.1)\text{\AA}^{-1}$ with a relative intensity to its nearest nuclear peak of approximately 40:1. The reflection could be seen in detector banks A,B and D but was out of range of bank C. The data in **figure 4.9** is from the 90° , D detector bank.

The single anomalous peak can be tentatively indexed as $(\frac{1}{3}, \frac{1}{3}, 1)^{10}$ but it is impossible to be specific about the direction in reciprocal space associated with any magnetic order on the basis of the magnitude of the wavevector alone. The temperature dependence of all nuclear Bragg peaks in the data sets were checked and there was found to be an excess of scattering in the low temperature Bragg peaks. This was taken to be further indication of coherent magnetic scattering.

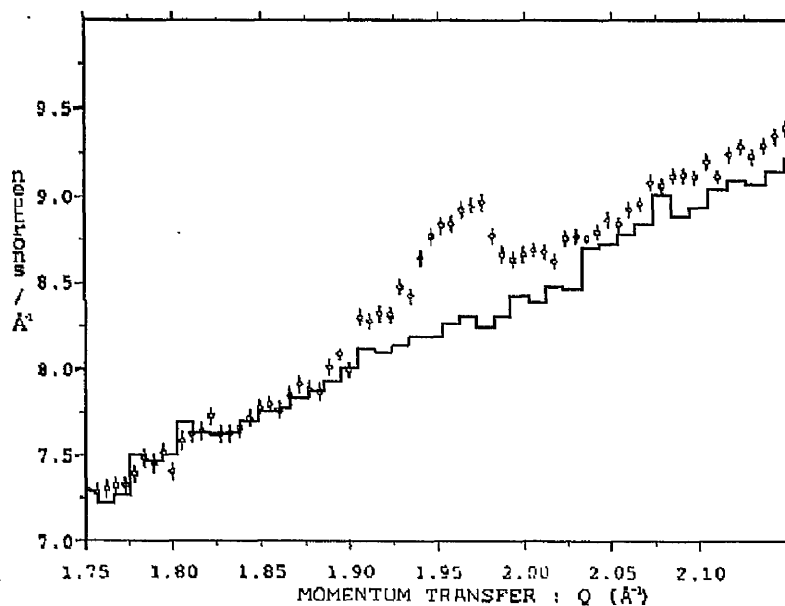


Figure 4.9. POLARIS data showing the anomalous peak at 15K (circles), which is absent at 350K (histogram).

It was the result of this experiment which provided the motivation for further neutron scattering studies of α -titanium. At the time of the experiment it was believed that this was the first observation of microscopic evidence of magnetic order in titanium. The next step was to obtain a single crystal and determine the direction of the wavevector q .

4.2.3 Diffraction Measurements on a Single Crystal of α -Titanium Performed on SXD at ISIS.

From the previous experiment $|q|$ was determined for the non-hcp peak but it is impossible to be sure of the direction of q . It was the aim of the next experiment to determine the direction of the magnetisation vector in reciprocal space through a single crystal study. A large single crystal was obtained from Metals Crystals and Oxides Ltd., approximately cylindrical in shape, 45mm long and 8-9mm diameter. The suppliers of the crystal indicated that the $[10\bar{1}0]$ direction was vertical and maintained 99.99+% purity. It was later found that the actual purity was almost certainly lower, less than 99.9%, see **table 4.1**. This could not be ascertained until the discovery of crystallites in the sample meant that a section was removed which was small enough to perform magnetisation measurements on.

4.2.3.1 Instrumentation and Method.

The single crystal diffractometer at the spallation neutron source is a two axis time of flight spectrometer with a two dimensional position sensitive detector. The central pixel of the detector was fixed at 90° to the incoming beam and in the equatorial plane. A schematic diagram is shown in **figure 4.10**. The sample was mounted, oriented with the $[10\bar{1}0]$ axis vertical (as given by the manufacturer), in a copper block with Araldite adhesive which in turn was screwed into a standard 8mm thread on the cryostat cold finger. A thermocouple was mounted directly onto the copper block and the whole array enclosed in an aluminium foil heat shield. A second aluminium shield was constructed around this and the whole sample mounted in a displex cooler. The displex cooler has a temperature range of 12 to 300K and a 360° , ω , rotation axis (vertical).

The only in situ orientation possible on this instrument is simple rotation about the vertical axis (the ω -drive). An alignment run was commenced but no high symmetry direction

observed so a procedure of rotation and running was continued until a principal line leading to a peak of high symmetry was observed which enabled peak indexing. From then on a visual search for anomalous peaks was commenced at values of ω (vertical axis) changing by 30° , a figure chosen as the angular width of the detector is approximately 75° thus giving comfortable frame overlap for indexing. Data was taken at temperatures dropping from room temperature to 15K in steps of 25K.

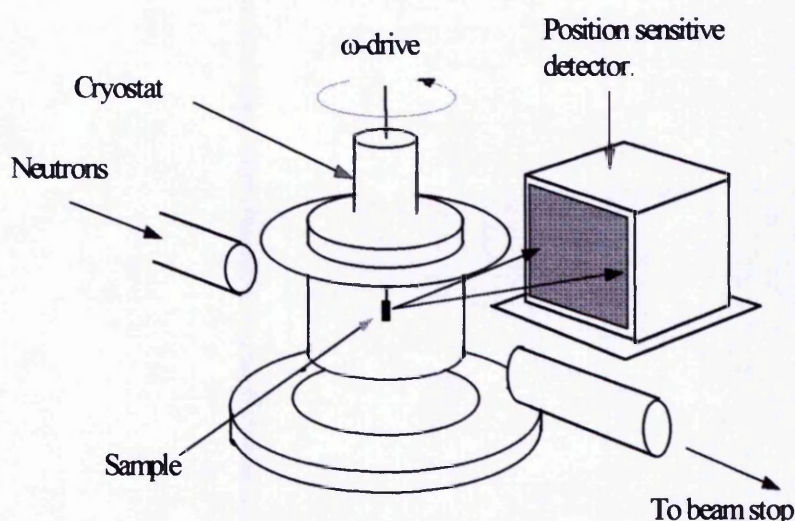


Figure 4.10 A schematic diagram of the single crystal diffractometer, S.X.D., at ISIS.

4.2.3.2 Results and Discussion.

The data collected is four dimensional; time of flight, intensity and two spatial coordinates. Hence it requires specific data handling software. The most useful visualization technique, which is available as part of GENIE¹¹, is to collapse the two spatial dimensions of the detector onto one i.e. sum all Y spectra onto the X axis of the detector and then separate out the individual spectra if an interesting feature is present. Due to the nature of the detector, defining the Bragg angle for a particular reflection in a particular spectrum requires a geometric consideration of the instrument, all indexing of peaks was done manually.

Due to the complex nature of the data, as outlined above, and further unforeseen complications the data was initially very confusing. A large number of spurious peaks were

observed in runs at all temperatures. Possible explanations for such phenomenon are given below.

- Instrument Fluctuations: Several warnings were issued to the team concerning the data acquisition electronics. Intense peaks where detector saturation occurred could result in a ghost peak appearing "below" the true peak and should be ignored. Data acquired near to the edges of the time window should be treated skeptically for the same reasons.
- Secondary scattering: Since the sum of two or more reciprocal lattice vectors is another lattice vector then a multiple scattering peak may appear at any reciprocal lattice vector which would account for spurious peaks at positions commensurate with the hcp structure yet forbidden by the structure factor. The probability of such reflections was high due to the large size of the crystal and thus high intensity of the nuclear Bragg peaks.
- Non-single crystal: The most promising explanation given the mass of spurious peaks. Crystallites with differing orientation to the bulk sample will superimpose a series of nuclear structure peaks onto the main pattern.

To try to extract genuinely interesting information from the resultant confusion code was written which matched peaks present in data collected at base temperature with peaks in the corresponding high temperature data file and listed any unmatched cold file peaks with the relevant details in an output file. In this way the above sources of spurious peaks would be dealt with as they are all temperature independent phenomenon. A program contained within GENIE called peaksearch¹¹ extracts all information about all the peaks present in a particular scan and writes this to a formatted data file making the reading of this data for the purposes of the peak-matching program relatively simple. The matching program allowed for fluctuations in time of flight and position in the detector along with a low intensity cut-off limit, which allowed for a low intensity 'noise' level, any unmatched peak below this limit

would be marked as suspect. These limits could be dictated by the user. The peak sorting program was successful in reducing the data to non nuclear structure peaks, from the single crystal and any crystallites present. From the information left it was not possible to identify any magnetic reflections as the background was too noisy with a mass of peaks identified by the peaksearch program which could not be credited with statistical significance.

Concrete evidence confirming the POLARIS data was not forthcoming from the SXD experiment. Although theoretically SXD is the perfect instrument for such an experiment with the ability to scan large areas of reciprocal space, the instrumental problems along with poor alignment capabilities meant that any magnetic structural information could be hidden by nuclear structure reflections or spurious data. A clearer more precise picture was needed. A single detector, two-axis diffractometer would be the canonical instrument for such a study and so the following experiment at Risø, the Danish National Laboratory, was proposed.

4.2.4 Diffraction Measurements on α -Titanium Performed on TAS3 at Risø.

Two experiments were carried out on this instrument; a single crystal survey of reciprocal space and a further powder experiment. The surfaces of the single crystal were mapped extensively using x-rays prior to this experiment in an attempt to identify the position of any crystallites. It was found that a section of one end, approximately 15% of the bulk, consisted of one if not more small crystallites. This section was removed by spark erosion. The section removed was small enough that a VSM measurement could be performed, the results of which are shown in **figure 4.7** (page 101) and **table 4.1** (page 102) The temperature at which the anomaly in the susceptibility appears suggests that the manufacturers estimate of purity (99.99+%) was over optimistic, comparison with the polycrystalline data suggests that it is less than 99.9% pure.

4.2.4.1 Instrumentation and Method.

TAS3 is a two axis diffractometer mounted on the research reactor DR3 at Risø the Danish National Laboratory. It has a single rotating detector used mainly in the equatorial plane but with facilities to be raised up to 10° out of plane. This gives the possibility to look out of the initial scattering plane in which the crystal was oriented. A schematic diagram of the instrument is shown in **figure 4.11**. For the first part of the experiment the crystal was the same as that used in the SXD experiment but mounted in an aluminum holder. Initially the crystal was aligned in open geometry, (not in the cryostat). Then it was enclosed within an aluminum can filled with helium exchange gas in an ILL Orange cryostat. The cryostat has a temperature range of 15 to 300K and was mounted on a two arc goniometer. For the second part of the experiment the same polycrystalline sample as used in the POLARIS experiment was mounted in the same cryostat as used in the first part of the experiment.

The geometry of the instrument enabled quick alignment and diagnostic work on the single crystal. It was immediately apparent that the manufacturer's orientation details were at best approximate. Simple alignment with the scattering plane being the a^* , b^* plane was not

possible due to physical restraints of the apparatus. The chosen scattering plane is shown in figure 4.12.

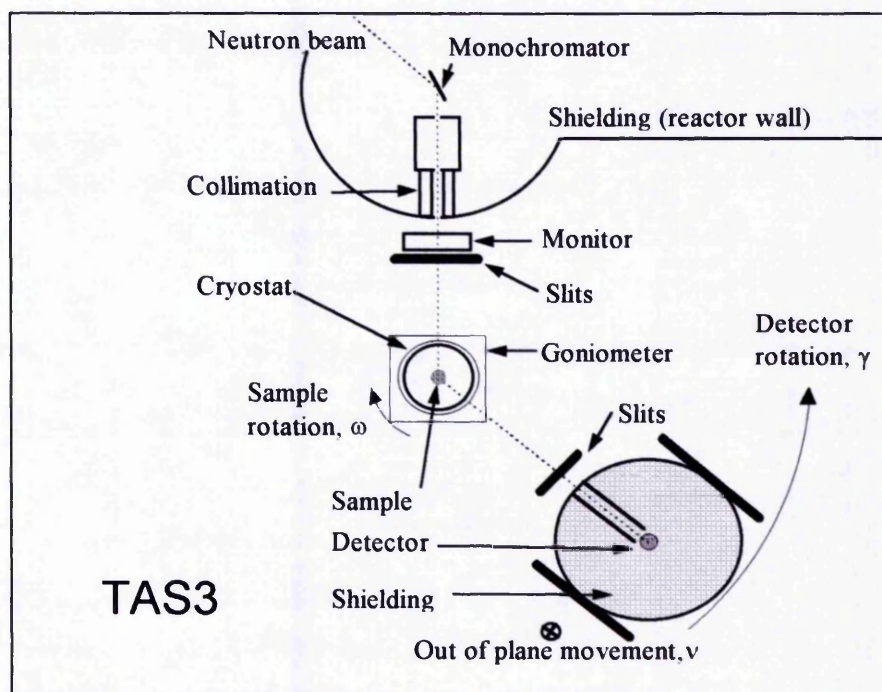


Figure 4.11 A schematic diagram of the TAS3 diffractometer. The out of plane movement is achieved by raising the detector out of the page along an arc centred at the sample.

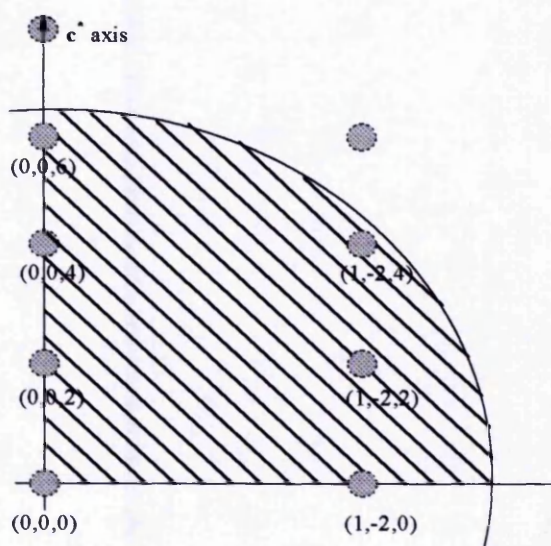


Figure 4.12 showing the chosen scattering plane and the area covered with $\lambda=1.3\text{\AA}$ neutrons.

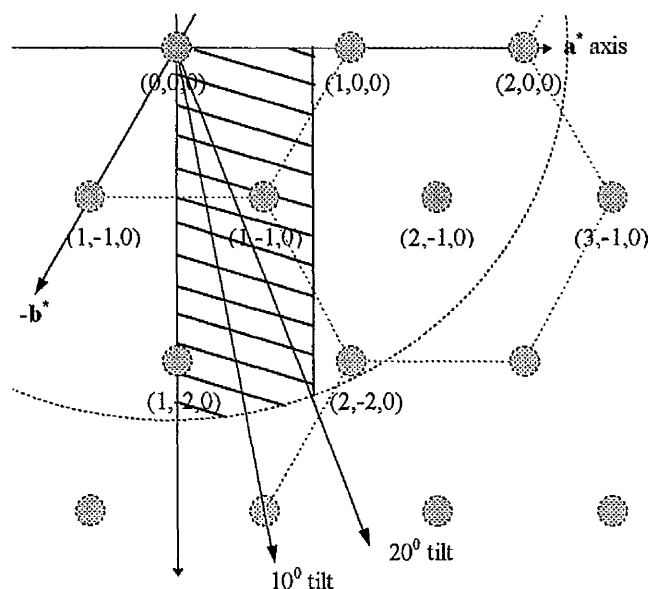


Figure 4.13. The extent out of the scattering plane into the basal plane allowed by the detector tilt and $\lambda=1.3\text{\AA}$ neutrons (hatched).

The orientation work immediately showed irregularities in a way SXD could not because of its complex data visualization problems. At room temperature several peaks were present which did not correspond to the hcp structure of Titanium. The first suspected source of such peaks were more crystallites, not revealed by the x-ray work as a result of being embedded within the crystal. This corroborated the SXD evidence and was shown to be the case by masking portions of the crystal with cadmium producing significant decreases in intensity of the spurious peaks. Topographic Polaroid photographs further confirmed this by showing that sample spurious reflections did not come from the whole crystal but only a small part. The top part of the crystal was consequently masked with cadmium which appeared to cover the crystallites.

The sample was then mounted in the cryostat and realigned on the diffractometer. When alignment had been achieved, horizontal and vertical slits were closed in around the sample at the reactor beam port and at the detector to reduce background scattering to a minimum. A series of scans was then undertaken to cover as large an area of reciprocal space as possible

initially staying in the chosen scattering plane. The wavelengths available to us were dictated by the monochromator but effectively imposed only an upper limit on the value of $|q|$ possible to reach as θ , the Bragg angle, could be varied from -45° to $+45^\circ$. (i.e. γ , which if $\nu=0$ is 2θ , has limits $\pm 90^\circ$) 45° being dictated by the mechanical limit of the apparatus.

Two principal scan types were used: $[\theta, 2\theta]$ and $[\omega]$. $[\theta, 2\theta]$ allow any radial trajectory to be scanned, e.g. radial from the origin of reciprocal space. this is achieved by changing ω by an amount θ then changing γ by an amount 2θ to bring Q back onto the radial path. An ω scan is a simple rotation of the crystal, hence reciprocal space, and so traces a circular trajectory through reciprocal space with the circle's center at the origin. A combination of these two scans allows any trajectory across the scattering plane. It is a standard feature of such instruments that software is already in place to calculate the necessary combination of motor drives required to track a given direction. A third scan was available on this machine provided by the out of plane movement of motor ν . A maximum of $+20^\circ$ and -10° was available, which enabled movement out of the scattering plane into the perpendicular basal plane. The extent of this movement can be seen in **figure 4.13** (page 111). This combined with previously described scans allowed full coverage of the first Brillouin zone. **Figure 4.12** and **figure 4.13** combined show the area of reciprocal space the instrument was able to cover. The method used to survey the area was a series of grid scans combined with more detailed searches in areas thought likely to yield results, such as the arc corresponding to 1.95\AA^{-1} , the $|q|$ of the powder peak observed in the POLARIS experiment. The grid size was dictated by the resolution of the instrument. For our purposes poor resolution was an advantage as the grid size need not be smaller than the resolvable width of a peak, this being the case any peak would be picked up. Scans could be programmed in terms of k and l for the scattering plane and h for out of plane scattering. An example mesh would be the (000),(002),(1-22),(1-20) rectangle with a step size of 0.05 reciprocal lattice units. Resolution was much reduced out of plane with full width half height, as scanned in ν , of 4.5° hence a step size of 2° in ν was sufficient.

The polycrystalline sample was mounted in the cryostat and a low temperature, 1.5K, data set collected by a simple γ -scan at a step size appropriate for the resolution. Data were also collected in the same way at 300K.

4.2.4.2 Results and Discussion.

Peaks were observed in the single crystal data, some of which had a dramatic temperature dependence (60% between 1.5 and 300K) suggestive of magnetic phenomenon and others which although not consistent with hcp titanium were not temperature dependent. Explanations for peaks which were not temperature dependent included those considered in the analysis of the SXD data along with:

- Order contamination: that is, for any wavelength λ allowed by the monochromator, wavelengths λ/n , where n is an integer, are also allowed, effectively giving multiple incident wave vectors $n\mathbf{k}_i$. Such reflections can be partially quenched by careful choice of monochromator although this would have restricted the choice of wavelength. An awareness of the phenomenon made identifying such reflections straightforward.
- Powder lines; polycrystalline aluminum diffraction lines were present due to the sample holder and cryostat. These were readily identified by characteristic values of q and as a consequence they could be 'tracked' directly in an ω scan.

For peaks displaying temperature dependence the following non magnetic explanations were considered:

- The Debye-Waller factor; a temperature dependent correction factor arising from increased nuclear thermal vibration. It is approximated as a Gaussian harmonic potential profile which transforms to a Gaussian in q -space and results in a decrease of the coherent

scattering amplitude. Although the exact form for a particular crystal is complex the increase in intensity at reduced temperature is unlikely to exceed 10% even at the highest $|q|$'s in this experiment and thus cannot fully explain this temperature dependence.

- Non-single crystal; an argument can be made to explain the temperature dependence in terms of a crystallite moving further into the beam as the crystal is cooled due to contraction of the bulk crystal, producing an increase in intensity. This seemingly tenuous argument is, in the light of the ISIS experiment the most likely explanation for the peaks not commensurate with the hcp structure. It can be readily checked by deduction of the orientation matrix required to bring the crystallite peaks into line with the bulk orientation.

A thorough search had been undertaken with the most probable symmetry sites covered i.e. the $(\frac{1}{3}, \frac{1}{3}, 1)$ type reflections. Problems still remained with crystallite contamination. The temperature dependent reflections were shown conclusively to be from a crystallite by considering their relative orientation, which displayed a perfect hexagonal close packed structure related to the bulk pattern by direct mapping via an orientation matrix. Suspicions were aroused as to the quality of the single crystal given the defects already discovered.

Data from the polycrystalline sample was statistically poor as a result of the relatively low flux and hence long counting times needed for good data. A peak of $|q|=1.96\text{\AA}^{-1}$ would, in this data appear at a scattering angle of 43.20° . The width of such a peak can be predicted by considering the resolution function which as a function of angle was modelled to a fourth order polynomial with a forced minimum at $2\theta_m$, θ_m being the monochromator take off angle. This method predicts a width of 0.902° for a peak at 43.20° . A peak can be fitted, at this scattering angle and width, in the data taken at 1.5K which will not fit at 300K, the two data sets are seen in **figure 4.14a** where a peak amplitude above background of (141 ± 54) neutrons was fitted, and **b** where no such peak would fit.

For comparison to the POLARIS data the TAS3 data was corrected for the Lorentz factor which is primarily a geometric correction arising from a fixed detector size and counting time at each measuring point. The proportion of scattering cone intercepted for a given scattering angle is not constant but varies as $\sin 2\theta$ with the radius of the scattering cone within the Ewald sphere. There is also a second factor arising from the probability of finding a crystallite in a given reflecting position, this contributes a $\sin \theta$ term, giving the full Lorentz correction for rotational scans of powder reflections to be,

$$L^{-1} = \sin 2\theta \sin \theta$$

Equation 4-3

Having applied these corrections the resultant relative intensities of the major Bragg peaks are comparable to the intensities from the POLARIS data with the intensity of the spurious peak being somewhat smaller than in the POLARIS data approximately an 90:1 relative intensity to the nearest Bragg peak.

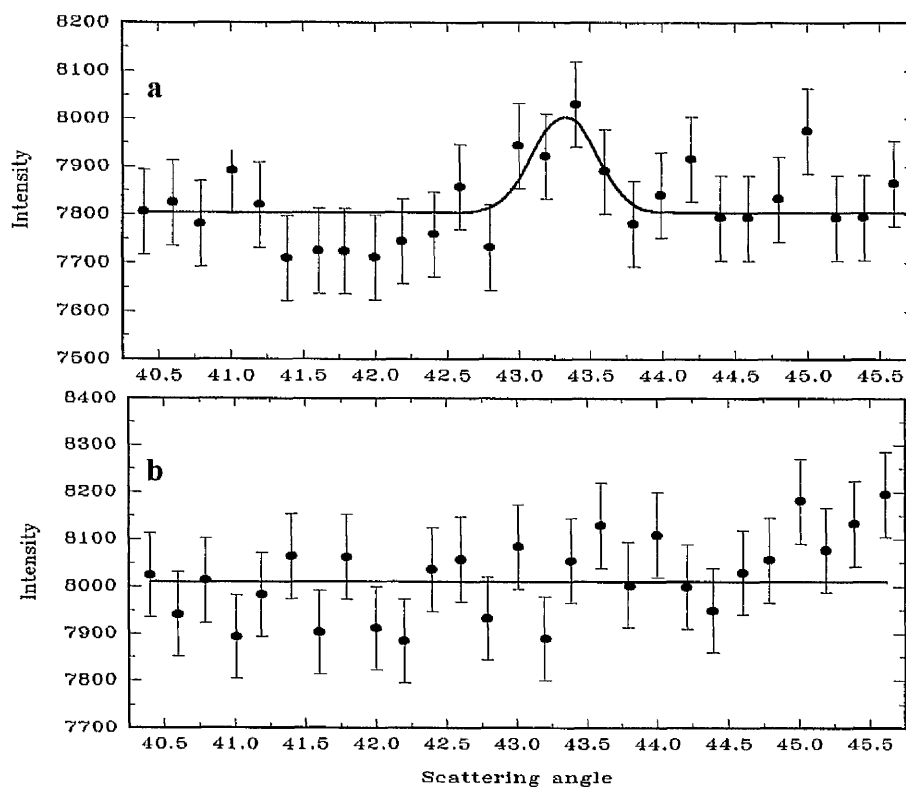


Figure 4.14. Fitted data from the Risø polycrystalline experiment showing the $|q|=1.95\text{\AA}^{-1}$ peak present in the low temperature data (a) and not in the high temperature data (b).

The observation of the non hcp structure peak in the powder data appeared to corroborate the previous observations on POLARIS although the reason for its lower relative intensity was not clear.

4.2.5 A Muon Spin-Relaxation Experiment on α -Titanium at ISIS.

The emerging subtlety of the problem led to the suggestion that muon implantation may be able to reveal any long range magnetic order present below T_n . The method is, in theory, extremely sensitive to microscopic internal magnetic fields although uncertainty involving the muon site within the sample can negate this advantage.

Muons are positively charged spin-half particles often considered as heavy positrons, the muon mass is $209 \times m_e$. The muon has a lifetime of $2.2 \mu\text{s}$ after which, on average, it decays to a positron and two neutrinos. The direction in which the positron is emitted holds information about the magnetic environment that the muon existed in.

Previous muon implantation experiments performed on chromium^{12,13,14,15,16} have been diverse in their claims although all have yielded at least some suggestion of muon-magnetic coupling. Given that the magnetic structure of chromium is reasonably well known oriented single crystals were used in most of the experiments. Two experiments were conducted on polycrystalline samples^{14,15}. Kossler et al¹⁵ observed muon-magnetic coupling in the form of a depolarisation intrinsic to the sample below the transition temperature. We have no knowledge of any magnetic structure of titanium and therefore we felt a polycrystalline sample gave the best chance of being able to detect any such long range order in α -titanium.

The sample used was a 50mm by 50mm flat plate of 99.999% purity supplied by Goodfellow Metals. This is the highest purity sample we were able to obtain. A VSM. Characterization of the sample (see **figure 4.8** (page 101) and **table 4.1**) puts the transition temperature at $(284 \pm 5)\text{K}$. The plate was 1mm thick, far in excess of the stopping distance of muons in such a sample. This ensures that no effects due to the sample mounting contaminate the data.

In the next section the principles involved in extracting information about internal magnetic fields from the data collected during such an experiment are outlined. For a much more detailed account see Chappert and Grynszpan.¹⁷

4.2.5.1 Theory.

Muons are implanted into the sample after being guided from the production site through a series of bending magnets. If we consider initially an experiment where there is no magnetic field then the angular distribution of positrons emitted by muon decay is described in a polar coordinate system by:

$$W_\theta = 1 + a_0 \cos \theta$$

Equation 4-4

Where a_0 is the asymmetry parameter. The positrons are preferentially emitted along the muon spin axis. This is a consequence of the parity violation in weak interactions. If we arrange an experiment such that there is an array of detectors forward and behind the decay site (usually the sample, see **figure 4-15**) then the count-rate in the forward and backward detectors will be given by:

$$N_{(F,B)} = N_0 \exp\left(-\frac{t}{\tau_\mu}\right) [1 \pm a_0]$$

Equation 4-5

With + forward and - backward. The exponential term arises from the radioactive decay of the muon, τ_μ being the half life, 2.2 μ s. In the presence of a static external magnetic field, B, the muon precesses at it's Larmor precession frequency ω_L . This modifies the count-rate expression to:

$$N_{(F,B)} = N_0 \exp\left(-\frac{t}{\tau_\mu}\right) [1 \pm a_0 \cos \omega_L t]$$

Equation 4-6

Assuming all the muons precess with the same frequency this expression holds true. A muon implanted in a sample in zero field will not precess unless there are internal local fields. Any coherent precession of the muons indicates the presence of long range magnetic order, e.g. coherent internal fields. It is this "zero field" configuration which we adopted.

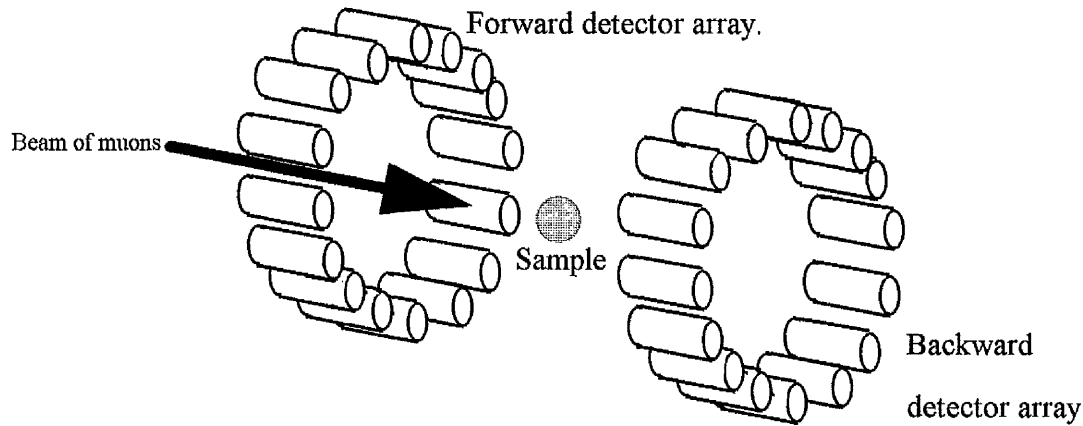


Figure 4.15. Muons are implanted in the sample where upon decay the emitted positrons are detected in either the forward or backward array of detectors. The muons are initially polarised such that the spins are pointing back down the beam line hence the naming of the detectors.

Under these experimental conditions it is $G_z(t)$ which holds the information we let $G_z(t)$ be defined by the equation:

$$N_{(F,B)} = N_0 \exp\left(-\frac{t}{t_m}\right) \cdot [1 \pm G_z(t)]$$

Equation 4-7

In practice $G_z(t)$ is obtained by measuring the ratio of forward and backward emitted positrons thus:

$$G_z(t) = \frac{N_f(t) - \alpha N_b(t)}{N_f(t) + \alpha N_b(t)}$$

Equation 4-8

Where α is an experimental factor governed by detector characteristics. $G_z(t)$ is the longitudinal relaxation function and holds information about muon mobility and moment fluctuations. In the event of depolarisation equation 4-8 must be modified. If the muons are exposed to a random field, in orientation or magnitude inside the sample, as is the case in a polycrystalline magnetic sample, then some spins will precess more rapidly than others. The result of such incoherent precession is a de-phasing of the muon spins (a similar effect occurs due to muon hopping), similar to the well-known NMR line broadening. In order to account for this an additional decay term must be added to the above expression.

To first order the relaxation function can be described by an exponential decay function:

$$G_z(t) = a_0 \text{Exp}(-\lambda t) \cdot \cos(\omega_\mu t)$$

Equation 4-9

Where λ is the depolarisation rate, a_0 is the initial asymmetry and ω_μ is the Larmor precession frequency due to any static local field B_μ .

4.2.5.2 Instrumentation and Method.

A zero field configuration was adopted due to the high sensitivity of this method. It was hoped that any long range magnetic order present in the sample would give rise to depolarisation of the muons and therefore be detectable as a decay constant, λ_{mag} , in the asymmetry.

Data were taken at a range of temperatures including the base temperature of the CCR (12K), 320K and the transition temperature, 280K.

4.2.5.3 Results and Discussion.

During the experiment stray fields of the order of several hundred milliGauss were present at the sample position due to a magnet on a nearby instrument. The sizes of these fields are well calibrated although a time average was used when the field changed during data collection. This effect was included in the model of the data by calculating the Larmor precession frequency of the muons in such a field and fixing the parameter ω appropriately.

We have assumed that there are five contributions to the form of the time dependent asymmetry: radioactive decay (exponential, with decay constant τ); depolarisation due to the sample environment (exponential, with well known decay constant λ_{cry}); an oscillatory term due to any stray external field, B_{ext} ; a term to account for detector dead time at high count rates, $F(n)_{dtime}$, and any depolarisation due intrinsically to the sample.

Fitting the data to a function of the form;

$$G_z(t) = A_0 \cdot F(n)_{dtime} \cdot \exp\left(-\left(\lambda_{cry} + \lambda_{mag} + \frac{1}{\tau_\mu}\right) \cdot t\right) \cdot \cos(\omega \cdot t + \phi)$$

Equation 4-10

allows $(\lambda_{mag} + \lambda_{cry})$ and A_0 , the initial asymmetry, to be extracted. $(\lambda_{mag} + \lambda_{cry})$ is plotted as a function of temperature in **figure 4.16a** and **b**. The normalization of the data to exclude effects due to external fields is not perfect. At small values of ω_L i.e. small external fields, λ and ϕ (the initial phase shift due to muons being in a field prior to deposition in the sample.) become statistically correlated. It is this that produces the large errors seen in **figure 4.16b**. The depolarisation due to the cryostat is measured by the muon beam staff using a silver sample which is magnetically neutral. Silver gives a value of 0.009, which is slightly larger than the mean value exhibited in our data. This is also most likely due to imperfect normalization. The initial asymmetry, A_0 , is also of interest as a reduction would be expected in the magnetic state, this was not the case as can be seen in **figure 4.17a** and **b**.

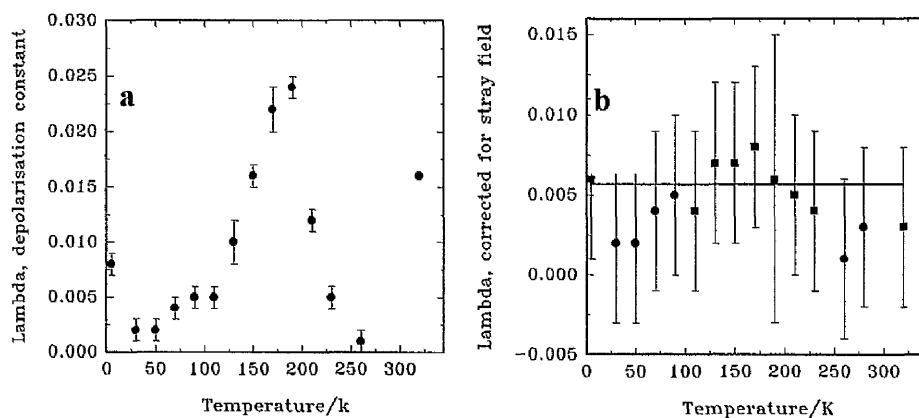


Figure 4.16a and b Depolarisation as a function of temperature before (a) and after (b) normalisation for stray field. The points in b denoted by a circle are not normalised as the stray field was small at this time.

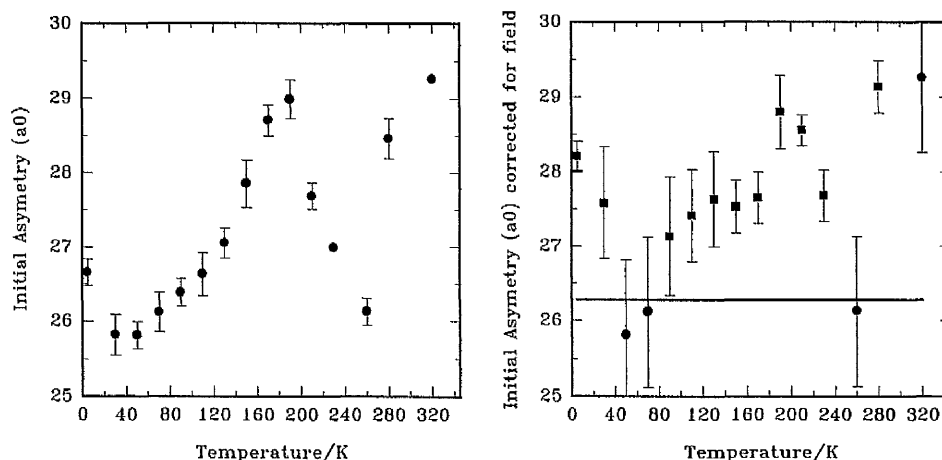


Figure 4.17a and b The initial asymmetry A_0 as a function of temperature before normalisation (a), and after (b)

In conclusion it is reasonable to say that no depolarisation due intrinsically to the sample was observed. This is in conflict with effects seen in chromium where sizable effects were observed at the transition temperature and at the spin-flip temperature^{13,12,16,15}. It is also reasonable to say that no reduction in the initial asymmetry was observed, this is consistent with chromium data. If α -titanium were an incommensurate antiferromagnet then an

experiment of this type should be sensitive to the internal magnetic fields. There is however, the possibility that α -titanium could be a comensurate system and the muons sit at sites within the crystal where the net internal field is zero and hence no signal would be observed. This is thought to be unlikely because a comensurate structure would have revealed its presence in previous experiments.

4.2.6 A Diffraction Measurement on Polycrystalline α -Titanium Performed on D1B at the ILL.

Given an inconclusive result from the muon experiment a definitive experiment was sought. The single crystal had revealed nothing of interest and is known to be of poor structural quality and purity, probably worse than 99.9%. The POLARIS data is convincing and taken with the corroboration from TAS3 it was felt that a full temperature dependence of this peak was needed to see if this correlates with the transition temperature suggested by the VSM susceptibility measurements. It was with this intention that the next experiment was planned.

4.2.6.1 Instrumentation and Method.

D1B is a two axis powder diffractometer positioned at the end of the thermal guide in reactor hall one at the ILL. A diagram of the instrument is shown in **figure 4.18**. There is a choice of monochromator between germanium and pyrolytic graphite, graphite was chosen for this experiment as it supplies a longer wavelength of neutron and thus makes lower $|q|$'s accessible along with a higher overall intensity than the germanium. The detector is a ^3He multidetector containing 400 cells. It has a radius of curvature of 1.525m and an angular range of 80° .

Two samples were used on this experiment with the intention of exposing any sample dependent properties. Both samples consisted of four rods of 99.99% purity titanium supplied by Goodfellow, each rod being 9.5mm in diameter and 40mm long. Magnetic susceptibility measurements were consistent with previous samples of this purity. Neither sample was de-gassed prior to the experiment. The sample was cooled in a unique low background, vanadium tailed ILL Orange cryostat which has a temperature range of 5 to 300K.

A measurement was made at 5K for 9.5 hours with the multidetector positioned between 5° and 85° . An incident wavelength of 2.52\AA was selected.

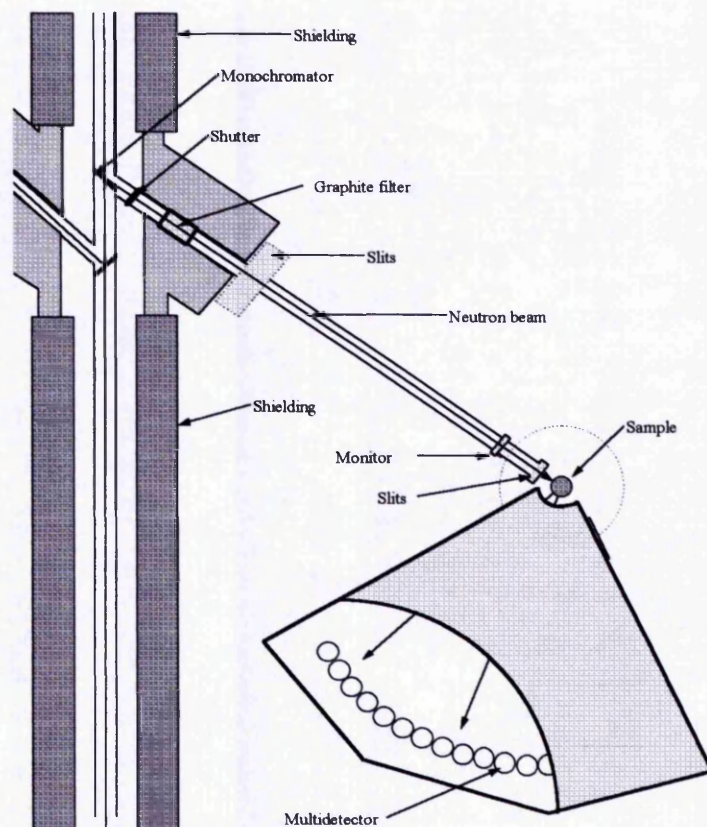


Figure 4.18. A schematic diagram of the D1B instrument at the ILL.

4.2.6.2 Results and Discussion.

The background levels on this instrument are generally very low which was true of this experiment although the data showed fluctuations in the incoherent scattering due to variations in the detector wire efficiency. The data are shown in **figure 4.19**. A region of increasing background was seen at low angles as well as sharp intensity reductions. An extra peak was seen at 54° , which is thought to be an artefact of the detector, since it is asymmetric. Another peak having $|q| = 2.14 \pm 0.02 \text{\AA}^{-1}$, corresponding to a scattering angle of 50.74° , was observed in all data measured at temperatures less than 145K. However the temperature dependence of its intensity does not have the characteristics of a

magnetic peak and is probably not intrinsic to the sample. The 2θ angle corresponding to the previously observed peak at $|q|=1.95\text{\AA}^{-1}$ was 46.04° . It is clear that this peak does not exist in these data. In **figure 4.19** it was expected that a peak of approximately 20,000 counts above background should be present the lack of which implies that the previous observations were not intrinsic to the sample. The minimum ordered moment that could have been observed in this experiment was found to be $0.044\mu_B$. This estimate was based on the statistical error present in the data and a calculation assuming a simple commensurate magnetic structure as used by Lowden¹⁰.

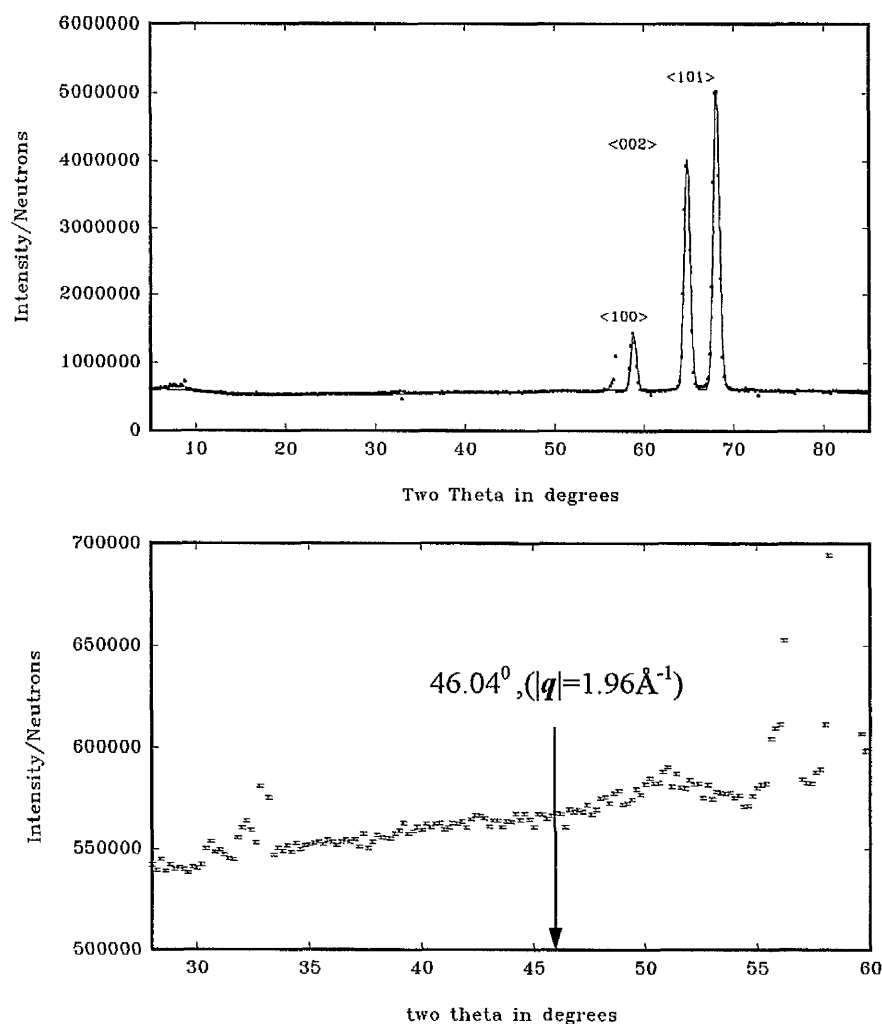


Figure 4.19. Data from the D1B experiment. **A**, shows the full data set collected for 9.5hrs at 5K. The main structural Bragg peaks are fitted. **B**, shows the area of interest the features present are discussed in the text. Note the unequivocal absence of a peak of 20,000 counts above background at a two theta value of 46.04 degrees (marked with arrow).

4.3 Discussion and Conclusions.

The anomaly in the magnetic susceptibility of α -titanium is persistent in a wide range of samples. The temperature at which it occurs appears to be extremely sensitive to sample purity. This would not be unusual for a magnetic phase transition. Impurities often suppress such transitions as in chromium for example, although the sensitivity here is high. Given the range of purities for which we have magnetisation data it is probable that the single crystal we obtained was of not very high purity, from the neutron data we also know it to be low quality. The single crystal work was very unlikely to have revealed any useful data due to these two factors. The experimental work carried out on the polycrystalline samples proves even more contradictory. The initial measurement on POLARIS appeared to produce a replicative low temperature peak (on TAS3) inconsistent with the hcp structure of α -titanium. A lack of experimental time in both cases meant that a temperature dependence of the peak or a full thermal cycling of the sample could not be done. The instrument independent and temperature dependent nature of the observation led us to believe that we were observing an effect intrinsic to the sample possibly even microscopic evidence of magnetic order.

During the course of both experiments great care was taken to exclude the presence of impurities from the sample environment. It is feasible that a gas condensing on the samples could produce spurious peaks. An extensive consideration of all the possible phases of ice, oxygen and nitrogen along with the other known phases of titanium (β and the rare ω -phase) could not produce any reflection with the requisite $|q|$. All these possibilities would have an associated family of peaks which could be readily indexed if they were present. Another possibility is that we were observing a transition associated with the creation of a charge density wave known to exist in the hydride, or a transition to an antiferromagnetic state known to exist in some oxides and hydrides^{18,19,20} These compounds however have distinct chemical structures for which there is no evidence in

any of the experiments. It is also known that the concentration of hydrogen, for example, needs to be high to facilitate the transition to a charge density wave, $1.8 < x < 2.0$ in TiH_x ²⁰. At these levels of concentration the sample would visibly deteriorate, whereas our sample remained bright and metallic throughout the experiments. It is also worth noting that the absorption of hydrogen at room temperature is negligible in titanium^{21,22}.

In parallel with this series of experiments Dr P. Novák²³ undertook some numerical electron band structure calculations, based on the local spin density approximation and the full potential linearised augmented plane wave method. The two Ti atoms contained within the unit cell were assumed to be non-equivalent, so that they may have different magnetic moments. Up to the present the calculations have always converged to a non-magnetic state where the moment is equal on both atoms. Novák points out that the Fermi level falls in the interval where the density of states changes rapidly it is possible that allowing cell parameters to vary a small amount could result in the appearance of magnetism. Novák concludes that if there is magnetism in titanium it is very weak.

The most convincing evidence to date is that of absence. The lack of an observation in the D1B experiment (and to some extent the muon experiment) prove conclusively that the previously observed peaks are not as a result of magnetism within the sample. It has been suggested that we are observing a structural phase change although I consider this unlikely as the hcp structure with its known unit cell dimensions is clearly unchanged throughout all our neutron experiments. It is my conclusion that titanium is not magnetic, or if it is, it is so weak that a new generation of experiments is required to demonstrate it as such. The nature of the magnetisation observations remains unsolved.

4.4 References.

- ¹ Pop I., Petrisor T., Giurgui A. and Néda A., J. Phys. Chem. Solids **46** pp1077 (1985)
- ² Collings E.W., Ho J.C., Phys. Rev. **B2** pp255 (1970).
- ³ Kojima H., Tebble R.S., Williams D.E.G., Proc. R. Soc. London **A260** pp237 (1961)
- ⁴ Collings E.W., Smith R.D., J. Appl Phys. **39** pp4462 (1968)
- ⁵ Squire C., Kaufman A., J. Chem. Phys. **P** pp673 (1941)
- ⁶ Tothill J.N., Jiang X. and Wilson J.A. J. Phys. Chem. Solids **47** pp1017 (1986)
- ⁷ Alberts H.L., J. Magn. Magn. Mat. **68** pp61 (1987)
- ⁸ Kilcoyne S.H., Cywinski R. & Schärpf O., J. Phys. Chem. Solids **53** pp771, (1992)
- ⁹ Dr. J. Esson, Private communication. (1996)
- ¹⁰ Dr. J.R. Lowden, Ph.D. Thesis, University of Manchester. (1995)
- ¹¹ David W.I.F., Johnson M.W., Knowles K.J., Moreton-Smith C.M., Crosbie G.D., Campbell E.P., Graham S.P. and Lyall J.S. PUNCH GENIE Manual "A Language for Spectrum Manipulation and Display", R.A.L. publication. RAL-86-102 (1986).
- ¹² J. Major, J. Mundy, M. Schmolz, A. Seeger, K.P. Döring, K. Fürderer, M. Gladisch, D. Herlach and G. Majer., Hyperfine Interactions **31** pp259-264 (1986)
- ¹³ A. Weidinger, G. Balzer, H. Graf, T. Möslang, E. Recknagel and Tn. Wichert., Hyperfine Interactions **8** pp543 (1981)
- ¹⁴ V.G. Grebinnik, I.I. Gurevich, A.I. Klimov, V.N. Majorov, A.P. Manych, E.V. Melnikov, B.A. Nikolsky, A.V. Pirogoc, A.N. Ponomarev, V.I. Selivanov, V.A. Suetin, V.A. Zhikov., Hyperfine Interactions **6** pp103 (1979)
- ¹⁵ W.J. Kossler, A.T. Fiory, D.E. Murnick, C.E. Stronach and W.F. Lankford., Hyperfine Interactions **3** pp287 (1977)
- ¹⁶ W. Templ, M. Hampele, D. Herlach, J. Major, J. Mundy, A. Seeger and W. Staiger., Hyperfine Interactions **64** pp679 (1990)

-
- ¹⁷ Chappert.J.,Grynszpan.R.I.,”Muons and Pions in Materials Resarch” North-Holland. (1984)
- ¹⁸ Adler S., Selwood.P.W.,J.Amer.Chem.Soc. **76** pp346 (1954)
- ¹⁹ Gibb.T.R.P.,Kruschwitz.H.W.,J.Amer.Chem.Soc. **72** pp5364 (1950)
- ²⁰ Wohlfarth.E.P.,Acta Metallurgica **4** pp226 (1956)
- ²¹ Hirooka Y., Miyake M.,Sao T., Journal of Nuclear Materials **96** pp227 (1981)
- ²² Moriya T., J.Magn.Magn.Mat. **14** pp1 (1979).
- ²³ Novàk P. Report to the Royal Society, private communication. (1996)

